SETTLING VELOCITY OF STRAIGHT AND CURVED RODS AT LOW REYNOLDS NUMBERS IN A QUIESCENT FLUID

DANIEL V. DARAMSING

A THESIS SUBMITTED TO THE FACULTY OF GRADUATE STUDIES
IN PARTIAL FULFILMENT OF THE REQUIREMENTS
FOR THE DEGREE OF
MASTERS OF APPLIED SCIENCE

GRADUATE PROGRAM IN MECHANICAL ENGINEERING
YORK UNIVERSITY
TORONTO, ONTARIO

MARCH 2023

Abstract

The motivation for the present thesis is towards understanding the effects of microplastic fibre geometry on the settling velocity, which is an important parameter used for atmospheric transport predictions. Microplastic fibres have been mathematically modelled as simple straight rods in the past to estimate their settling velocity; however, samples collected worldwide demonstrate more complex geometries. One common geometric parameter of realistic microfibres is curvature, and the effect of this parameter on the settling velocity is the focus of the present thesis. A new drop tank and particle tracking system were custom-designed to measure the settling velocity of curved rods at low Reynolds numbers typical of microfibres found in atmospheric samples. A parametric study of the settling velocity of curved rods demonstrated that the settling velocity of curved rods was always larger than that of straight rods with the same diameter and aspect ratio, and the smaller the radius of curvature, the faster the settling velocity. An experimental model was developed to relate the Reynolds number at terminal velocity and drag coefficient for both straight and curved rods to inform predictions. It is shown that non-ideal effects can significantly affect the estimation of travel of microfibres in comparison to other existing models, which emphasizes the importance of improved models that are tuned to predict the settling velocity of microfibres for atmospheric simulations of microfibre transport.

Acknowledgements

I would like to take this opportunity to express my heartfelt appreciation to Professor Dr. Ronald Hanson for his invaluable contributions to my academic and professional development during my graduate studies at York University. As a member of the Fluid Mechanics and Flow Control (FMFC) team, I am grateful to have had the opportunity to work under his guidance and mentorship, and wouldn't be possible without his constant support and guidance. Additionally, I want to acknowledge Dr. Mark Gordon for his support and co-supervision during my research. Furthermore, I would like to thank Liisa Jantunen from Environment and Climate Change Canada (ECCC) for her support throughout my research. I would like to extend my sincere gratitude to my esteemed Ph.D. mentor, Mr. Amirhossein Hamadi. Mr. Hamadi's mentorship has not only helped me grow as a researcher but also as a person. His unwavering support, encouragement, and faith in my abilities have been a constant source of motivation and inspiration, and I feel immensely fortunate to have had the opportunity to work under his guidance. Additionally, I would like to thank the Lassonde School of Engineering, undergraduate researcher Roozbeh Alishahian for assistance during the early stages of my research. On a personal note, I would like to express my heartfelt appreciation to my parents, Chandra and Khooschand Daramsing, for their love, guidance, and support throughout my academic and personal journey. I dedicate this thesis to them as a testament to their unwavering commitment to my success.

Table of Contents

List of Tables

List of Figures

Chapter 1

Introduction

Microplastics (MPs) are a subset of plastic particles that are generally smaller than five millimetres in their characteristic dimensions. MPs have attracted significant attention in recent years due to their widespread presence in remote locations around the globe and the potential negative impacts they may have on the environment and human health [1]. These particles can come from a variety of sources, including the breakdown of larger plastic items and the release of microbeads from personal care products. They have been found in a wide range of environments, including oceans, rivers, soil, and air/atmosphere, and there is growing concern about the potential negative effects they may have on aquatic life and, the food chain, as well as on human health. MPs are believed to be transported globally by two main mechanisms, by water and by air (see for example Allen *et al.* [2]). MPs can be transported from sources, or redistributed throughout the environment, by water [3], however, MPs can also travel thousands of kilometres in a relatively short time in the atmosphere [1, 4].

Dris *et al.* [5], Allen *et al.* [6], Bergmann *et al.* [7], Abbasi *et al.* [8], Wright *et al.* [9], Brahney *et al.* [10], and Evangeliou *et al.* [11] all provided evidence that microplastics are transported long-range by, and deposited from, the atmosphere. Sampled MPs were found to vary in shape, size and composition. In particular, microfibres (MF), which are usually defined as synthetic (petroleum-based) fibres of small diameter and elongated length, were in

abundance. Microfibres are a common shape of microplastics material that is often found in samples, (see for example Dris *et al.* [5], Liu *et al.* [12], and Wright *et al.* [9]) and they make a significant portion of the mass of microplastic material identified in these samples. Microfibres that are found in remote areas usually have a diameter of 25 μm, and fibres of similar diameters may have a length of 2-3 mm [13]. There is currently limited knowledge about how fibre orientation, length, or curvature affect settling characteristics.

There are no existing models created specifically to calculate the settling velocity of microfibres and past researchers often apply other available models. For example, in the seminal work by Allen *et al.* [6], MPs were considered as spherical sand grains with unknown effects on estimates of long-range transport. In another example, Wright *et al.* [9] included a model of a fibrous microplastic for one case, albeit the fibre model was developed for Reynolds numbers of two orders of magnitude or less than the setting occurring in the simulation, with unknown implications to results. Wright *et al.* [9] calculated the settling velocity for a spherical polystyrene (1.05 g/cm^3) fibre of diameter 100 μm and a cylindrical polyacrylonitrile (1.184 g/cm^3) fibre with a length and width of 400 μm and 20 μm to be 0.32 m/s and 0.06 m/s, respectively. The model applied to calculate the settling velocity was from Henn *et al.* [14] which calculated the aerodynamic equivalent diameter of a short reinforcing fibre. Allen *et al.* [6] and Wright *et al.* [9] use simple models derived for ideal cases which do not provide an accurate representation of fibres falling. Henn *et al.* [14] computes the aerodynamic equivalent diameter which is valid for cylinders aspect ratios greater than 20. In fact, the gap in knowledge of the atmospheric transport dynamics of real MPs is often noted in the related literature [6, 9, 15, 16].

The overarching motivation of the present thesis is to support improved atmospheric transport predictions of microfibres. It is widely known that microfibres shapes found in the environment are not straight but appear to be three-dimensional [5, 7, 6, 9]. One common feature of the three-dimensional shapes is the curvature of fibres, which we hypothesize to have an important role with respect to aerodynamic properties such as settling velocity in

addition to the Reynolds number, fibres falling orientation, diameter, length, curvature and material composition. The specific objectives of the present thesis are to:

(1) Design and validate a testing apparatus to measure the settling velocity and orientation.

(2) Quantify the effect of aspect ratio (length to diameter) on the settling of fibres at Reynolds number typical of atmospheric transport of microfibres.

(3) Quantify the effect of curvature on the difference in settling of idealized straight microfibres and identify appropriate scaling parameters.

The results of the present study are compared to other common models in the literature to potential differences that may be obtained from transport predictions.

The measurement and characterization of the aerodynamic behaviours of MPs fibres pose significant challenges due to the small size of these particles. One challenge is in obtaining or producing well-defined shapes with repeatable dimensions. Additionally, tracking the mean motion and rotation of MPs fibres presents difficulties. These challenges were overcome in the present study through the use of a glycerine-fall chamber, where the medium was various high concentrations of glycerine and water rather than air. The chamber was designed to replicate the same Reynolds number regime for MP fibres falling in still air, and the velocity and orientation of the fibres were measured using a particle tracking velocimetry (PTV) method. The viscosity of this medium enabled the use of brass rods, rather than micrometre-scale plastic fibres, to simulate the shapes of MPs fibres in air and was determined using models from [17, 18, 19]. The brass rods, which were of millimetre scale, allowed for the controlled study of factors such as aspect ratio and rod curvature, which have been observed to be important variables in microfibres found in the environment.

This thesis is organized as follows. Chapter 2 presents a review of the background literature relevant to the current study. The experimental design, including the apparatus and methodology, is described in Chapter 3, along with a validation of the procedures used. Chapter 4 presents and discusses the results of the experiment in detail, including a

thorough analysis of the data collected and a discussion of the implications of the findings. The sources of error in the results are also carefully examined and discussed, to provide a comprehensive understanding of the findings. The results are then placed in the context of previous research. Finally, in Chapter 5, a summary of the main conclusion is given in addition to recommendations for the future direction of this research outlined and the recommendations arising from the findings of the study are presented. These recommendations provide a road map for future work in this field and offer insights that may be of value to others working in related areas.

Chapter 2

Background

Chapter 2 presents a comprehensive literature review on MPs in atmospheric deposition, covering various sources and pathways of MPs and their potential impacts on the environment. The geometry and sizes of MPs are noted to give an understanding of what has been collected. To better understand the transport and behavior of MPs in the atmosphere, the chapter delves into the principles of fluid dynamics, discussing drag coefficient and Reynolds numbers for both spherical and non-spherical particles. Finally, the chapter examines a range of experimental setups that have been developed and used in various research to track the falling of different particles.

2.1 Microplastic Review

Pollution from MPs is a well-known global problem and in 2014, the United Nations Environmental Programme (UNEP) stated MPs pollution is 1 of 10 emerging issues that the world faces today [20]. Hartmann *et al.* [21] classes MPs that are smaller than 5 millimetres in size to 1 μm. This definition is consistent with the guidelines set forth by the Marine Debris National Oceanic and Atmospheric Administration (NOAA) and the European Marine Strategy Directive [22]. The origin of MPs links to either primary or secondary sources.

Primary sources of MPs are part of manufactured products. For example, a primary source of microfibres are textiles [7], or in another example, a primary source of microbeads is cosmetics or toiletries (banned by the Government of Canada in June 2017 owing to noted accumulation in the Great Lakes of Ontario). Secondary sources originate from physical, biological, and chemical processes resulting in the degradation of large plastic debris and are primarily caused by anthropogenic activities such as waste collection and littering. For example, photo-oxidation, cold temperature, and mechanical abrasion (from tires and road markings as examples) [23] result in secondary emission of MPs or further degradation to nanoplastics. Nanoplastics are a subset of plastic pollution with characteristic sizes less than 1 μm [21]. Plastic litter, manufactured by-products, and construction waste can be broken down into microplastics (MPs), which can be transported and suspended in the atmosphere by wind and weather conditions (see Figure 2.1). This atmospheric transportation contributes to the distribution of MPs in the environment. Once airborne, MPs can travel long distances through the atmosphere and eventually settle in various locations across the globe, including mountain tops, forests, lakes, and oceans. Fishery, marine vessels, and marine industries are direct sources of microplastics (MPs) entering bodies of water, and beach litter is another contributor [24]. Additionally, agricultural activities and washing machines also contribute to the presence of MPs in soil, with a single use of a washing machine resulting in the discharge of up to 1900 polyester fibers [25]. MPs have been found to contain toxic by-products which are ingested by microorganisms, potentially endangering these species and leading to their presence in the food chain [26, 27].

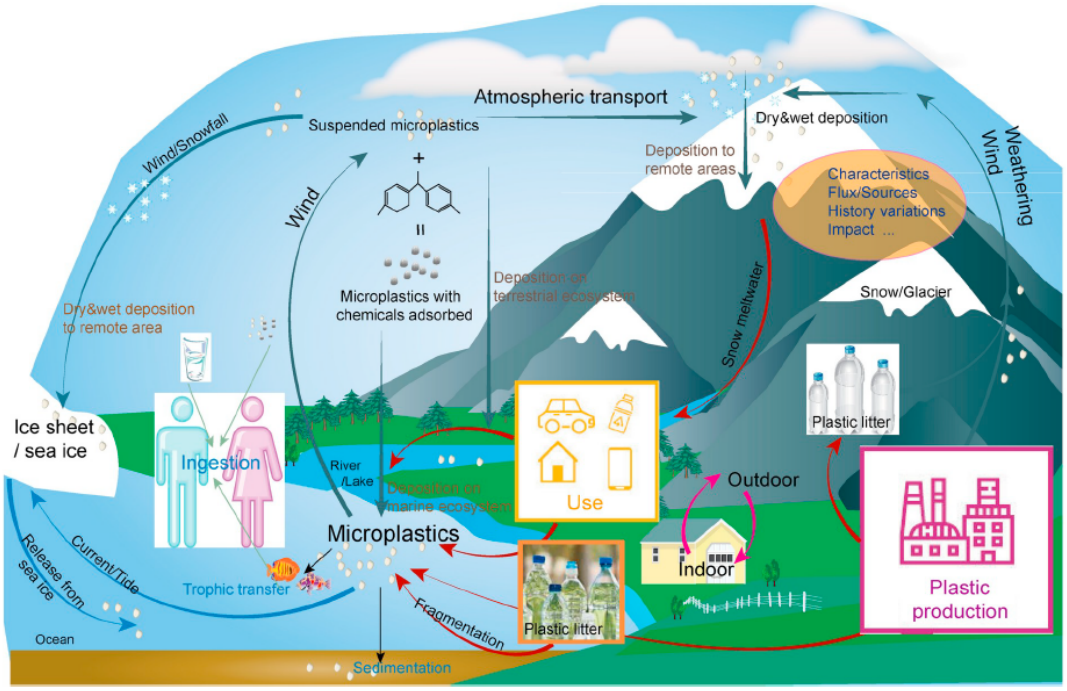

Figure 2.1: Conceptual model of how atmospheric microplastics enter and cycle within the environment. Figure is taken from Zhang *et al.* [15] with permission.

Due to their lightweight nature, MPs have also been shown as a transportation device resulting in invasive species entering an ecosystem consequently disturbing normal activities [28]. Airborne MPs also occur in indoor environments which depends on the ventilation and room partitions [29]. This poses the possibility of being inhaled and potentially leading to respiratory health issues. There is clear evidence of various MPs ranging up to 250 μm of different geometries found in human lungs [30]. Furthermore, research has shown that finished plastics can contain monomers, additives, dyes, and other toxic ingredients [31]. In addition, microplastic materials have the ability to absorb mutagens and carcinogens. Chemical coated microplastics can also act as a shield against atmospheric degradation [11]. It has been noted that colorful particles absorb light, decreasing the surface albedo of snow and ice and accelerating melting, similar to the effects of black carbon.

The study of atmospheric deposition of MPs is a rapidly growing field of research. According to a review by Allen *et al.* [1], there have been 200 publications on this topic in the past decade, compared to 1,000 on marine transportation of MPs (see Figure 2.2). The first quantification of atmospheric deposition was measured in Paris by Dris *et al.* [32] and published in 2015. Recent transportation modeling studies by Brahney *et al.* [10] and Liss *et al.* [33] used Hybrid Single Particle Lagrangian Integrated Trajectory (HYSPLIT) and were compared with plastic deposition rates obtained weekly. However, the accuracy of these results was uncertain due to a lack of complete spatial and temporal data sets. Su *et al.* [34] conducted a critical review of pathways and influences, dating the contribution of MPs to the atmosphere back to 1862 for bio-based plastics and 1907 for synthetic plastics. Beyond MPs, other studies have shown pollutant transport in the atmosphere. For instance, large Sahara dust particles (up to 450 μm in diameter) can be transported over distances of 3,500 km from the Sahara to the North Atlantic through mechanisms such as rapid horizontal transport, turbulence, uplift in convective systems, and electrical levitation of particles [35].

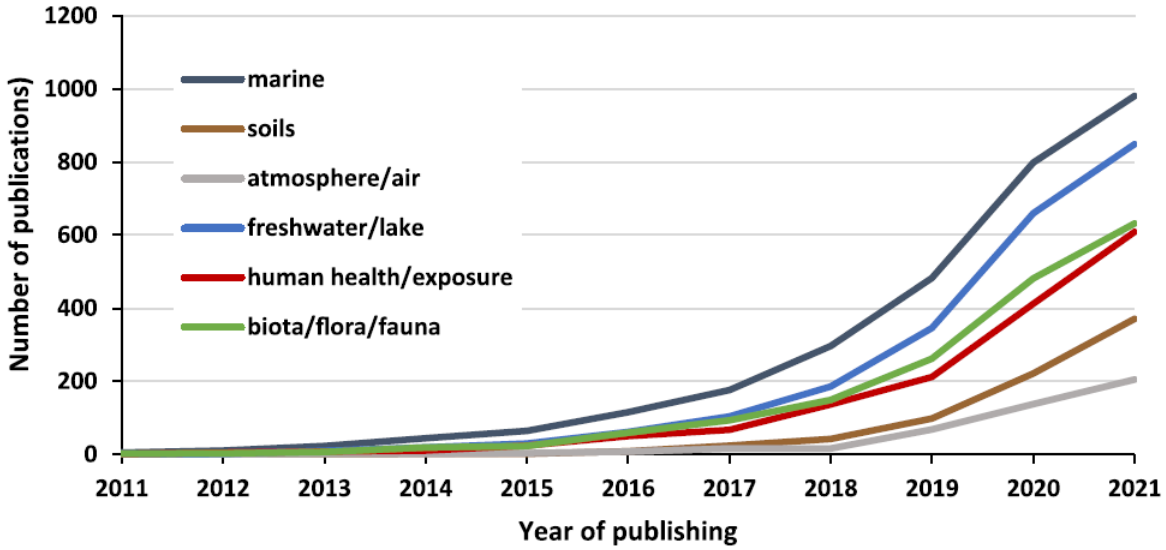

Figure 2.2: Trends in publications over the last decade (2011 - 2021) related to articles on MPs. Reproduced from Allen *et al.* [1] with permission.

Pollen particles from willow and pine (ranging from 10 μm to 200 μm) have been observed being transported at an altitude of 3 kilometres in just five days from western Europe to the Arctic [36]. These are just a few examples, as the literature on this topic is extensive.

Microplastics ranges from a variety of different lengths, aspect ratio, chemical composition, fibrous, non-fibrous, synthetic and natural materials as shown in Figure 2.3. The terms microplastics and fibres are used interchangeably however the important difference is MPs are extremely small pieces of plastic debris while fibres have the characteristic of a filament or thread. Natural fibres, such as rayon, are produced naturally by plants, animals, and geological processes while synthetic fibres such as polyethylene result from anthropogenic activities such as textile manufacturing. Bullard *et al.* [16] summarized, that the most common shapes identified for atmospheric deposition of microplastics are fibres, where more than 80% were found from Dris *et al.* [32] in Paris, Cai *et al.* [37] in Dongguan, Zhou *et al.* [38] in Yantai, Wright *et al.* [9] in London and Klein *et al.* [39]. According to Allen *et al.* [6], varnish was the most frequent polymer type found in their studies and this reflects the widespread use of this coating for vehicles, wind turbines, ships and buildings. Based on the observation of their geometry MPs can be classified into four categories; fragments (flattened and shard like), films (transparent and thinner than fragments), granules (rounded) and foams (sponge-like textures). Fragments and films were the most common for non-fibrous MPs found in Wright *et al.* [9] studies. Microplastics in the atmosphere are not straight fibres as their structure is influenced by the environment. A crimped fibre is defined as the difference of the strand fully straight versus how much it is bent.

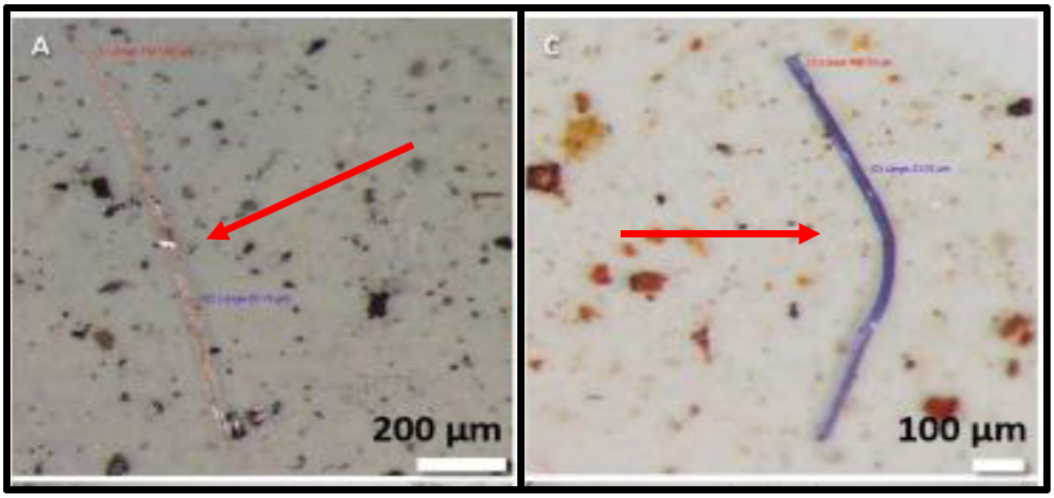

Figure 2.3: Fibre samples (polystyrene, fibre length 1101 μm and diameter 20.75 μm) and (polyvinyl chloride, fibre length 956 μm and diameter 23.03 μm) collected from the Arctic taken from Bergmann *et al.* [7].

The summary presented in Table 2.1 offers a comprehensive overview of the investigations conducted on microplastics (MPs) collected from atmospheric deposition around the world. The compositions of MPs collected from atmospheric deposition are diverse, with common materials including Polystyrene (PS), Polyethylene (PE), Polypropylene (PP), Poly-Vinyl Chloride (PVC), Polyethylene terephthalate (PET), Ethylene-vinyl acetate (EVAC), Polytetrafluoroethylene (PTFE), Polyacrylonitrile (PAN), and Polyurethane (PUR) (with densities ranging from 0.91 to 1.38 g/cm^3). The most frequent microplastic sizes observed range from 100 μm to 600 μm and are typically fibrous in nature. As per the data presented in Table 2.1, microplastics transported through atmospheric deposition exhibit a wide range of lengths, from 250 μm to 2000 μm, and diameters between 10 μm to 50 μm. The most common diameter of microfibres is noted by Wright *et al.* [9] to be 20 μm which corresponds to aspect ratios from 12.5 to 100 with the above lengths mentioned. Additionally, the densities of these MPs were also taken into account, with values ranging from 0.92 g/cm^3 for polypropylene to 1.32 g/cm^3 for poly-vinyl chloride. The reported dimensions and material densities are used

further in Chapter 3 with respect to the design aspects of the experimental setup.

Table 2.1: Summary of microplastics identified from collected samples to be assume deposited from the atmosphere from varies recent studies. Adapted from Zhang *et al.* [15] with further recent additions.

Reference	Location	Length (μm)	Shape
Dris *et al.* [32] 2015	Paris, France	100-1000	Fragments, Fibre
Dris *et al.* [5] 2016	Paris, France	50-1400	Fibres
Dris *et al.* [40] 2016	Paris, France	50-450	Fibres
Klein *et al.* [39] 2019	Hamburg, Germany	63-5000	Fragments, Fibres
Dehghani *et al.* [41] 2017	Tehran, Iran	250-500	Granules, Fibres
Abbasi *et al.* [8] 2019	Asaluyeh County, Iran	100–1000	Fibres, Granules
Cai *et al.* [37] 2017	Dongguan, China	200-700	Fibres, Foams
Qian *et al.* [42] 2017	Yantai, China	100 - 300	Film, Foam
Allen *et al.* [6] 2019	Pyrenees, Europe	100-300	Fragments, Fibres
Bergmann *et al.* [7] 2019	Europe and Arctic	11-250	Fibres
Wright *et al.* [9] 2020	London, England	400-500	Fibres
Yukioka *et al.* [43] 2020	Japan	100 - 5000	Fragment, Films
Robin *et al.* [44] 2020	Ireland	N/A	Fibres
Szewc *et al.* [45] 2021	Gdynia, Poland	5-720	Fibres, Fragments
Truong *et al.* [46] 2021	Ho Chi Minh, Vietnam	300 - 5000	Fibres
Huang *et al.* [47] 2021	Guangzhou, China	25 - 5000	Fibres, Fragments
Knobloch *et al.* [48] 2021	New Zealand	30 - 5000	Fibres, Films
Soltani *et al.* [49] 2021	Sydney, Australia	200 - 400	Fibres
Parolini *et al.* [50] 2021	Alps, Italy	83 - 1910	Fragments, Fibres

2.2 Fluid Dynamic Principles

The dynamics of a free-falling particle is first discussed in this section with respect to the governing equations. Afterward, the effect of particle geometry (spherical and non-spherical) on the settling velocity behavior is addressed. The relation between the non-dimensional parameters affecting the dynamic of the particle fall such as Reynolds number and drag coefficient are discussed.

2.2.1 Dynamics of a Free-Falling Particle

A particle falling in a fluid will experience three forces, gravity, drag and buoyancy. Gravity is a body force that acts on the mass, whereas drag is a surface force. Buoyancy is also a body force, but acts opposite to gravity. If the density of the object is much greater than the fluid the buoyancy force may be neglected. The free body diagram for a sphere falling in a fluid with the buoyancy neglected is shown in Figure 2.4. To solve the drag force for a spherical particle, the equations of a fluid motion must be solved to determine the velocity and pressure fields around the body. For an incompressible Newtonian fluid, the velocity and pressure are governed by the continuity Equation 2.1 (mass balance) and the Navier-Stokes Equation 2.2 (momentum balance).

$$\frac{\partial \rho}{\partial t} + \frac{\partial u_x}{\partial x} + \frac{\partial u_y}{\partial y} + \frac{\partial u_z}{\partial z} = 0 \tag{2.1}$$

$$\rho\left(\frac{\partial u_x}{\partial t} + \frac{\partial u_x}{\partial x} + \frac{\partial u_y}{\partial y} + \frac{\partial u_z}{\partial z}\right) = -\frac{\partial p}{\partial x} + \mu\left(\frac{\partial^2 u_x}{\partial x^2} + \frac{\partial^2 u_x}{\partial y^2} + \frac{\partial^2 u_x}{\partial z^2}\right) + \rho g_x \tag{2.2}$$

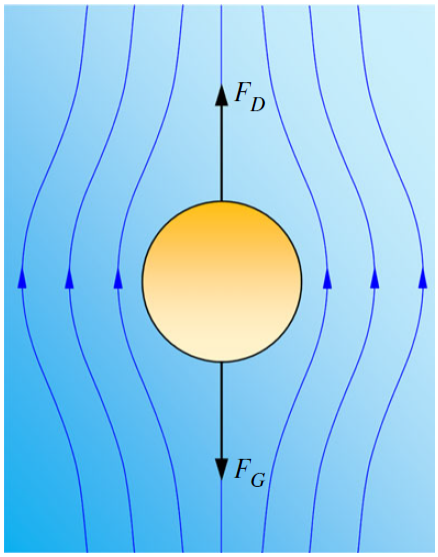

Figure 2.4: Schematic diagram of the settling velocity for a spherical particle where F_D is the drag force and F_G is gravity acting on the particle. The streamlines around the particle are shown. Sourced from Dey *et al.* [51] with permission.

The mass continuity equation states that mass is conserved where u represents the velocity having components in the x, y and z direction. Additionally, the rate of change of density with respect to time is shown at the beginning of the equation which represents how the density of the fluid changes over time. Assuming an incompressible flow means the density of the fluid is constant and does not change with time, so the rate of change of density is zero. Therefore the continuity equation is reduced to Equation 2.3.

$$\nabla \cdot u = \frac{\partial u_x}{\partial x} + \frac{\partial u_y}{\partial y} + \frac{\partial u_z}{\partial z} = 0 \tag{2.3}$$

The Navier-Stokes equation is Newton's second law applied to any fluid where the left side represents mass times acceleration while the right-hand side represents forces. The first two terms on the right side of Equation 2.2 are the internal forces which are the pressure gradient and the viscosity, respectively while the last term is the external force (gravity) acting on the body. The continuity Equation (2.1) and Navier-Stoke Equation (2.2) can be nondimensionalized by using a characteristic length (L), a characteristic velocity (u_0), a

dimensionless time (τ) and pressure (ϕ) as shown in Equations 2.4 and 2.5.

$$U_x = \frac{u_x}{u_0}, \quad U_y = \frac{u_y}{u_0}, \quad U_z = \frac{u_z}{u_0}, \quad \zeta_x = \frac{x}{L}, \quad \zeta_y = \frac{y}{L}, \quad \zeta_z = \frac{z}{L} \tag{2.4}$$

$$\tau = \frac{tu_0}{L} \quad \& \quad \phi = \frac{pL}{\rho U^2} \tag{2.5}$$

Substituting the nondimensionalized variables (Equation 2.4 and 2.5) into the continuity Equation (2.1) and Navier-Stokes Equation (2.2) introduces the Reynolds number as shown in Equation 2.7 (Seinfield *et al.* [52]).

$$\frac{\partial U_x}{\partial \zeta_x} + \frac{\partial U_y}{\partial \zeta_y} + \frac{\partial U_z}{\partial \zeta_z} = 0 \tag{2.6}$$

$$\frac{\partial U_x}{\partial \tau} + U_x \frac{\partial U_x}{\partial \zeta_x} + U_y \frac{\partial U_x}{\partial \zeta_y} + U_z \frac{\partial U_x}{\partial \zeta_z} = -\frac{\partial \phi}{\partial \zeta_x} + \frac{1}{Re}\left(\frac{\partial^2 U_x}{\partial \zeta_x^2} + \frac{\partial^2 U_x}{\partial \zeta_y^2} + \frac{\partial^2 U_x}{\partial \zeta_z^2}\right) \tag{2.7}$$

$$Re = \frac{\rho u_\infty d}{\mu} \tag{2.8}$$

The Reynolds number described in Equation 2.8 is a dimensionless number, which relates the inertial forces to viscous forces that helps predict the flow patterns in the fluid. The term ρ is the density of the fluid, u_∞ is the velocity of the fluid, d is the characteristic linear dimension and μ is the dynamic viscosity of the fluid. When the Re is much smaller than 1, the non-dimensional Navier-Stoke Equation (2.7) can be simplified into Equation (2.9).

$$\frac{\partial \phi}{\partial \zeta_x} = \frac{1}{Re}\left(\frac{\partial^2 U_x}{\partial \zeta_x^2} + \frac{\partial^2 U_x}{\partial \zeta_y^2} + \frac{\partial^2 U_x}{\partial \zeta_z^2}\right) \tag{2.9}$$

The velocity and pressure distribution for a sphere was obtained by Stokes using Equations (2.6 and 2.9) assuming an infinite medium, rigid sphere and no slip condition. At every point there is a normal force (pressure) and tangential force (friction from shear stress caused by the velocity gradient) acting on the surface of the body. The summation of the normal and frictional force is the drag force for any particle shape as long as it is in the direction of gravity [53, 54]. When the Reynolds number is less than 10 the drag force is comprised of two-thirds viscous stress and one-third pressure as shown in Equation 2.10 where R_p is the radius of the sphere.

$$F_D = F_t + F_n = 4\pi\mu R_p u_\infty + 2\pi\mu R_p u_\infty = 6\pi\mu R_p u_\infty \tag{2.10}$$

2.2.2 Drag Coefficient

The drag force on a sphere as it travels through a fluid when Reynolds number is less than one is called the Stokes' regime (or creeping flow). In this region the inertial terms are negligible and viscous forces are the main contributor. However, if Re ≥ 1, Stokes laws will be underestimated since the inertial forces must be accounted for. Therefore a new method is needed to account for this and it is represented by the drag coefficient, C_D shown in Equation 2.11. Just like the Reynolds number the drag coefficient is a dimensionless number and quantifies the resistance of an object in a fluid environment.

$$C_d = \frac{F_d}{\frac{1}{2}\rho u^2 A_p} \tag{2.11}$$

In the Equation above, F_d is the drag force experienced by the object, ρ is the fluid density, u is the velocity of the object and A_p is the projected area of the object. Note that the term $1/2$ in the denominator is included to account for the fact that the drag force is acting in the opposite direction of the velocity. For an incompressible flow over a sphere the drag coefficient depends only on the Reynolds number and the drag coefficient can be categorized into three realms, the Stokesian, transitional and Newtonian realm as shown in Figure 2.5. The Stokesian ranges is for Re ≤ 1, the transitional realm is between 1 to 1000 and the Newtonian realm is Reynolds number past 1000. For the Stokes' regime, the relation appears linear until Re $= 1$ and is modeled by Equation 2.12 for a smooth sphere. For Reynolds number ≤ 20 the flow is considered to be laminar and the streamlines appear identical on both the upstream and downstream. For Re > 20, flow separation occurs at the rear stagnation points of the sphere and forms closed recirculating wakes.

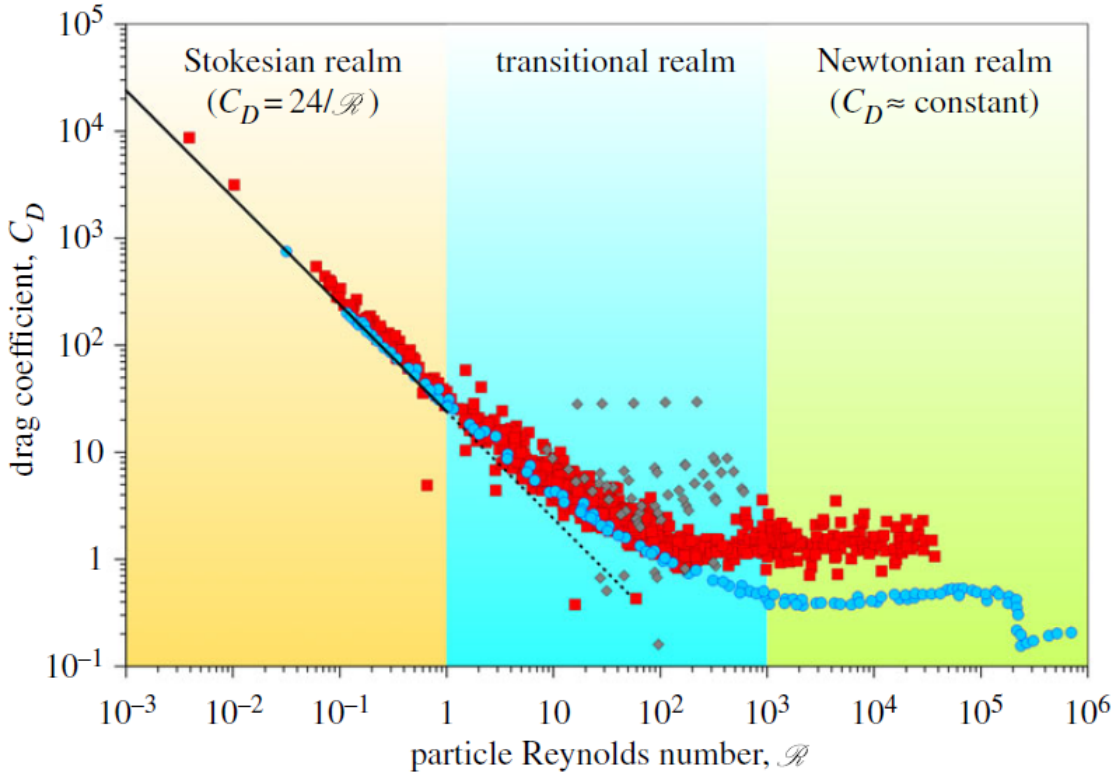

Figure 2.5: Experimental data for drag coefficient C_D versus particle Reynolds number, Re taken from several studies, includes spheres (circles), natural grains (squares) and shell fragments (diamonds). The solid line is Stokes' law, while the dotted line is that extended to the transitional realm. Sourced from Dey *et al.* [51] with permission.

$$C_D = \frac{24}{Re} \tag{2.12}$$

As Reynolds number increases, the length of the wakes and separation angles increases which means vortex shedding is a function of Reynolds number. For spheres the drag coefficient drops abruptly Re $\approx 2{\cdot}10^5$ which indicates the transition from laminar to turbulent in the boundary layer [53]. Given that the focus on the present research is low Reynolds number, the Newtonian regime is not discussed further for brevity. Further discussion of modelling efforts of C_D with Re for the Newtonian range of Re is summarized by Barati *et al.* [18].

The equation of motion for a sphere falling when Re < 1 can also be derived using a force balance. From Equation 2.4 only two forces will be present, gravitational and drag force acting in opposite directions. In the analysis of a falling object, two key parameters to consider are the terminal velocity and relaxation time. Terminal velocity is defined as the maximum speed reached by the object due to the resistance of the medium through which it is falling, while relaxation time represents the duration required for the object to attain its terminal velocity. On the other hand, the settling velocity is the velocity at which a particle or small object is suspended in a fluid and will fall under the influence of gravity, without any additional external forced acting on it. Understanding these characteristics can provide insight into the dynamics of the falling object. By performing mathematical manipulations, it is possible to determine the characteristic relaxation time (as given by Equation 2.13) and the terminal velocity (as given by Equation 2.14) for a spherical particle.

$$\tau = \frac{m_p}{3\pi\mu_f D_p} = \frac{d_p^2(\rho_p - \rho_f)}{18\mu_f} \tag{2.13}$$

$$v_t = \frac{m_p g}{3\pi\mu_f D_p} = \frac{d_p^2(\rho_p - \rho_f)g}{18\mu_f} \tag{2.14}$$

The terminal velocity for particles beyond the Stokesian regime can be calculated using Equation 2.15. This equation is applicable to both spherical and non-spherical particles, with the caveat that the drag coefficient, C_D, is a function of the particles Reynolds number.

$$v_t = \sqrt{\frac{2m_p g}{\rho_f A_p C_D}} \tag{2.15}$$

2.2.3 Non-Spherical Particles

Non-spherical particles can be classified as regular-shaped particles (disk, cones, ellipsoids) or irregular-shaped particles (non-symmetric, rough surface) [55]. The drag coefficient for non-spherical particles tends to depend on the Reynolds number, particle shape, surface roughness, falling orientation, particle to fluid density ratios, secondary motion, fluid turbulence intensity and particle/fluid acceleration [55, 56, 17, 57]. While the drag on a sphere at low-Reynolds

number is well established, a single universal method to characterize the drag of a non-spherical particle does not exist. Yet many applications involve particles that are not idealized spheres. Natural processes such as cylindrical asbestos fibres and pollutant transport in the atmosphere involve non-spherical particles. For the case of modelling the settling velocity of microfibres, a type of non-spherical particle, Wright *et al.* [9] utilized an existing model for non-spherical particles to estimate the settling velocity of fibres simulated in their study of atmospheric transport. For the case of atmospheric transport of MPs, Wright *et al.* [9] use approximations for predicting the settling velocity of non-spherical particles.

Wright *et al.* [9] calculated the settling velocity for a 100 μm spherical non-fibrous particle (polystyrene) and cylindrical fibrous particle (polyacrylonitrile) of aspect ratio (length/diameter) of (400 μm/20 μm) to be 0.32 m/s and 0.06 m/s, respectively. Wright *et al.* [9] used the method of Henn *et al.* [14] to calculate the corresponding settling velocity of the fibre. Henn *et al.* [14] introduced the concept of the aerodynamic equivalent diameter, which represents the effective spherical diameter of particles with the same falling velocity in air. Using this method, it is possible to calculate the aerodynamic equivalent diameter of cylindrical fibres (as given by Equation 2.16).

$$D_a \approx (d_c \ln 2\beta)^{1/2} D_c \tag{2.16}$$

In Equation 2.16, d_c is the density of the particle, β is the aspect ratio of the fibre and D_c is the cylindrical diameter. Allen *et al.* [6] used the same approach for calculating the settling velocity for a spherical 25 μm dust particle, however, crucial information such as the density of the particle was omitted. In the present study, the settling velocity was determined to be 0.1 m/s. Based on this value, it can be inferred that the density of the particles in question is approximately 5000 kg/m^3. This estimation is supported by the fact that, for a particle with a diameter of 25 μm, a settling velocity of 0.1 m/s would correspond to a density of around 5000 kg/m^3. It is worth noting that the density of these particles was not explicitly reported by Allen et al. [6] in their publication. Since non-spherical particles do not have

a well-defined diameter, a volume equivalent sphere diameter (Equation 2.17) or nominal diameter is often used for normalization. In one notable case, Song *et al.* [17] evaluates the Reynolds number using the volume equivalent sphere diameter, where V_p is the volume of the non-spherical particle.

$$d_{eq} = \left(\frac{6V_p}{\pi}\right)^{1/3} \tag{2.17}$$

Tran *et al.* [57] conducted a series of settling experiments for irregular particles to determine the orientation of the particle during settling. It was observed for Re between 0.1 to 100, all irregular particles showed a tendency to align their maximum cross-section normal to the direction of settling motion. For Reynolds number greater than 100 the particles settled in a steady-state orientation only after they were released with their maximum cross-section parallel to the horizontal axis. Elongated particles wobble around a horizontal axis, whereas fuller bluff bodies rotate and thus follow a spiral motion rather than a straight vertical path. At a given Reynolds number, the values of the drag coefficient for all the irregular particles were higher than the ones for spheres, regardless of their shape. Near-spherical particles showed the lowest drag coefficient while higher values of drag coefficient occurred from non-circular planer constructions, such as a cylindrical bar.

A study from Marchildon *et al.* [58] found that for Re < 80, a cylinder falls with a fixed orientation, keeping its maximum projected area perpendicular to the main motion direction in a straight path. For Reynolds number above 80 the cylinder may exhibit oscillation and oscillation will be present once Re > 300 and travels in a sinusoidal path. Similar observations from Bagheri *et al.* [56] found isometric particles showed oscillations and instability in the range $70 <$ Re < 300.

2.2.4 Shape Factors

The challenge of analyzing non-spherical particles lies in their unique geometry compared to spherical particles. To address this issue, researchers and scientists have developed

dimensionless numbers that are used to classify the shape factor of non-spherical particles [56, 59, 17, 57, 60]. These non-dimensional values allow for the collapsing of non-spherical particles onto the same C_D and Re curve used for spheres. One of the most commonly used shape factors is the aspect ratio (AR), defined as the length of the particle along the symmetrical axis divided by the largest diameter of the cross sections. For cylinders, it would be the length divided by diameter. Spheroids are classified as an oblate (AR < 1) or prolate (AR > 1). For oblate spheroids, the shape becomes a circular disk. For prolate spheroids the shape is needle-like and when AR $= 1$, the object is a sphere [55]. The sphericity of a particle, ϕ is the ratio of the surface area of the equivalent-volume-sphere to the actual surface area of the particle, A_p, where d_{eq} is the equivalent diameter.

$$\phi = \frac{\pi d_{eq}^2}{A_p} \tag{2.18}$$

The sphericity value of unity means the particle is a sphere and as ϕ decreases the particle deviates further from a perfect sphere. Less spherical particles of the same volume and mass tend to have a lower in settling velocity which implies a higher drag coefficient [57, 60]. For a fixed volume, the drag coefficient has an inverse correlation with sphericity [56]. A similar parameter called circularity (surface sphericity), c, is the ratio between the perimeter of a sphere with equivalent projected area, d_A, and the projected perimeter of the particle, P_p, is the projected perimeter of the particle in the direction of motion shown in Equation 2.19.

$$c = \frac{\pi d_A}{P_p} \tag{2.19}$$

The Corey shape factor, Co developed by Corey *et al.* [61], is another approach for characterizing the shape of three-dimensional irregular particles and is defined as the ratio of the shortest particle axis to the square root of the product of the other two axes. For a cylinder on its side, Co is equal to the $\mathrm{AR}^{-1/2}$ [57].

Bagheri *et al.* [56] showed in the Stokes' regime (Re < 1), the drag coefficient is slightly more sensitive to change in elongation than in the flatness, while in the Newtonian regime, the impact of the flatness of the drag coefficient is much more significant than the elongation.

Furthermore, the drag coefficient in the Stoke's regime is relatively insensitive to surface roughness and shows no alter in the drag coefficient while in the Newtonian regime it plays a significant role in the drag coefficient.

2.2.5 Drag Coefficient for Cylinders

Oseen *et al.* [62] found that as we get further from the surface of the sphere the inertia in the Navier-Stokes equations becomes more important compared to the viscous term. Oseen's study resulted in an improvement in Stokes' drag by taking into account the inertial factors in the Navier-Stokes Equation. Oseen's presented an Equation 2.20 for calculations of the sphere drag coefficient.

$$C_D = \left(\frac{24}{\mathrm{Re}} + \frac{3\mathrm{Re}}{16}\right) \tag{2.20}$$

Tritton *et al.* [63] conducted a set of experiments involving the settling of quartz fibres in an air flow with the Reynolds number ranging between 0.5 to 100.
The aspect ratio of the fibres ranged above 600. Tritton *et al.* [63] presented a curve for the variation of drag coefficient with Reynolds number which was fitted on the average of all their experimental results, where this curve is shown in Figure 2.6.

Huner *et al.* [64] conducted experiments investigating the drag on a circular cylinder at a low Reynolds number of 0.23 to 2.6. The size of the particles ranged between 0.5 mm to 1 mm in diameter with lengths of 25 mm to 42 mm. The experiments were conducted inside a wind tunnel with an open-circuit system and utilized particle image velocimetry to measure the velocity of the cylinders. The experimental results were compared to existing theoretical models and found that the models were accurate for high aspect ratio cylinders. However, the drag on small aspect ratio cylinders was significantly higher than predicted by the existing models.

Khalili *et al.* [65] utilized the Lattice–Boltzmann method to numerically study the effect of container size or boundaries of a domain on the settling velocity of a cylinder at very low

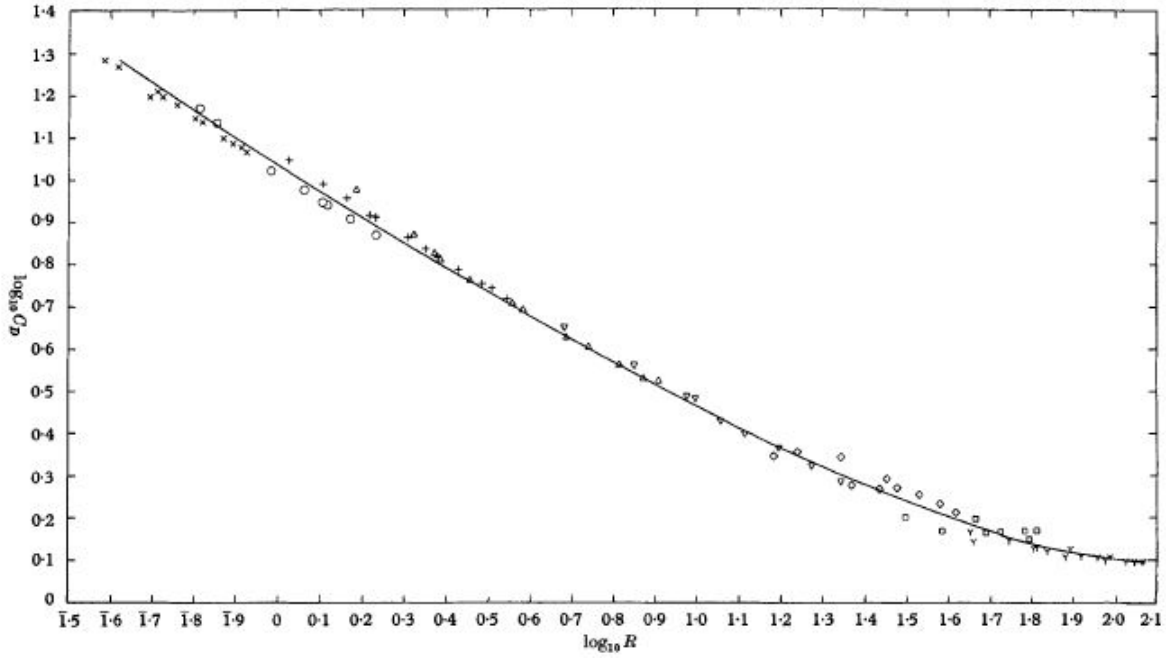

Figure 2.6: The variation of drag coefficient with Reynolds number for the fibres studied in Tritton *et al.* [63].

Reynolds numbers. The new correlation to calculate the drag coefficient for a 2D cylinder in an infinite domain is shown in Equation 2.21 where γ is the Euler's constant ($\gamma = 0.577216...$).

$$C_D = \frac{4\pi\delta}{\mathrm{Re}}\left(\frac{2}{1+\sqrt{1+4.3\delta^2}}\right) \quad \text{where} \quad \delta = \left[\frac{1}{2} - \gamma - \log\left(\frac{\mathrm{Re}}{4}\right)\right]^{-1} \tag{2.21}$$

2.3 Particle Tracking Experiments

Various research experimental setups used to track particles will be discussed in this section. It is important to note that the methods mentioned below represent only a few examples, given the numerous available particle track methods. The literature review examines the use of single and dual-camera setups, Particle Image Velocimetry (PIV) systems, and experiments related to falling fibers for particle tracking.

In the literature there are numerous experiments have been conducted to measure the drag on non-spherical particles. One of the first experiments to determine the drag on a

cylinder at a low Reynolds number was conducted by Finn *et al.* [66]. This approach looked at the deflection of a thin wire suspended in an air stream where the Reynolds number ranged between 0.06 to 6.0. The experimental results matched with Lamb's theoretical Equation (2.22) and the drag force was calculated from the measured deflection of the pendulum.

$$C_D = \frac{8\pi}{\frac{1}{2} - \gamma - \ln(\frac{Re}{8})} \quad \text{where } \gamma \text{ is Euler's Number} \tag{2.22}$$

Jayaweera *et al.* [67] studied the behavior of freely falling cylinders and cones in a viscous fluid. It was observed at a very low Reynolds number, Re < 0.1, cylinders did not show preferential orientation, however for a Reynolds number ranging between 0.01 to 0.1, cylinders oriented themselves based on their aspect ratios. For cylinders with aspect ratios (diameter/length) > 1, they would fall with their long axis horizontal, while particles with aspect ratios < 1 fall like disks.

Gomez *et al.* [68], conducted an experiment to model the settling velocity of the dispersion of fern spores (diameters 23 to 73 μm) using a single camera. Other researchers have also conducted experiments on particles settling in glycerin-water mixtures. A Particle Tracking Velocimetry (PTV) experiment done by Carranza *et al.* [69] using a single high-speed camera with stereo adapter lens looked at PTFE (polytetrafluoroethylene) cylinder and sphere falling in glycerine weight ratios of 50%, 60% and 80 % at room temperature. The authors computed the Reynolds number, settling velocity, and drag coefficient for each test case using a single camera system. To verify their calculated velocities using the frame rate of the camera and measured pixel displacement and compared experimental measurements of a falling spherical glass bead with a well-known theory. A simple procedure was done by Carranza *et al.* [69]. One difficulty which Gomez *et al.* [68] faced was their light source reflected off the glass surface resulting in sources of errors.

While a single camera may be sufficient to capture the settling of a single particle falling vertically, more than one camera is used to track more complex motions. For instance, research conducted by Esteban *et al.* [70] used a dual camera setup where each camera was placed

perpendicular to one another directed on a tank observing various planar particles such as disks and polygons. Garrett *et al.* [71] conducted an aerodynamic study of falling snowflakes observing distributions of the aspect ratios and falling orientations with a multi-camera setup. The multi-camera setup was advantageous as it views the snowflakes' orientation as it fell. A few more examples of systems using multiply camera systems to track particles falling are conducted by Cole *et al.* [72] and Kramel *et al.* [73].

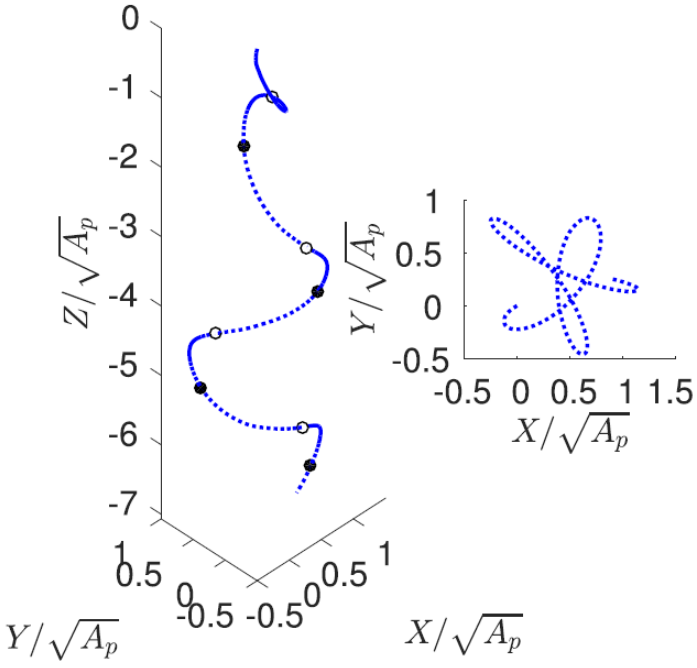

Figure 2.7: 3D construction of the falling trajectory and (X,Y) planar projection for a disk descending in "spiral" to "planar zig-zag" motion. Aerial view of the particle is shown to the right. Sourced from Esteban *et al.* [70] with permission.

The advantages of using a multi-camera setup is the recreation of viewing the motion in a 3D space. This technique can show motion patterns such a reoccurring oscillations and an aerial view of the motion, as shown in Figure 2.7. The disadvantages of the setup is the systems must be calibrated where they focus directly at the same spot otherwise it would result in experimental errors.

Other relevant experiment conducted by Qi *et al.* [74, 75, 76] employed a particle image velocimetry (PIV) technique using a single camera for experimentally measuring the settling velocities and orientations for long aspect ratio nylon fibres with Reynolds number of 0.5 - 2 based on fibre diameters. A laser emits a 532-nanometre wavelength to create a green light sheet that illuminates the fibres. The laser sheet thickness is 5 millimetres formed by a telescopic and diverging lens shown in Figure 2.8. The intensity of the laser is nearly Gaussian which helps determine whether a fibre is fully inside the light sheet. Fibres also come in a variety of aspect ratios and as they increase, they become more difficult to disperse; as they decrease, there is a loss of strength resulting from poor binding.

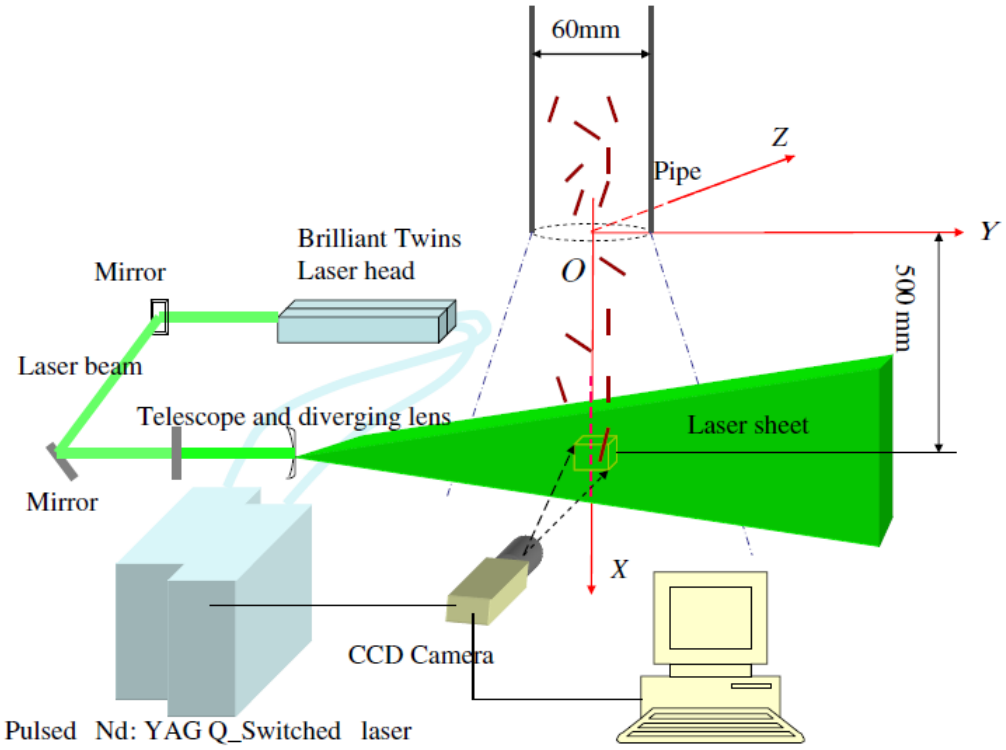

Figure 2.8: A PIV experimental setup to track microfibres falling used by Qi *et al.* [74] to track the motion of fibres falling in still air.

Qi *et al.* [74, 75, 76] used a single camera setup, which had limitations in accurately measuring the curvature of the fibres. From their finding, it was concluded that the straightness

of the fibre does not have a significant impact on the settling velocity. A similar experiment was performed by Yang *et al.* [77] focused on the free settling properties of single fibre particles (cotton, glass and jute) of lengths 5 mm, 10 mm and 20 mm in air. Their experiment utilized two LED lights to illuminate the fibre and one high-speed camera. One of their findings was that the different fibre materials have moisture absorption rates which slightly increases their settling velocity. The frictional drag was affected by parameters such a fibres roughness while drag depended on the orientation it fell.

Nguyen *et al.* [78] conducted a PTV experiment for polyester MPs fibres of 1 to 4 mm in length settling in a water column. They considered the variables of length, curliness, settling orientation and settling velocity for these particles. The authors found that a fibres curliness reduces the settling velocity, whereas a curly fibre 1.3 times longer than a straight fibre can settle 1.75 times slower. Their measured settling velocity ranged between 0.1 to 0.55 mm/s and showed a slight increase with the length (and therefore aspect ratio) of the fibre. Lastly, the sphere equivalent diameter was found to be a good representation of microplastic fibre size to predict the drag coefficient.

In the study conducted by Song *et al.* [17], an experiment was carried out to measure the settling velocity of non-spherical particles. The authors introduce a new model, which is based on a combination of a previous drag coefficient model and a new settling velocity model, for predicting the drag coefficient and settling velocity of both spherical and non-spherical particles in a Newtonian fluid. Song *et al.* validated their model by comparing it to experimental data and other existing models and found that it is accurate and applicable for a range of particle shapes and Reynolds numbers. The drag coefficient and settling velocity equation is valid with particle Reynolds number ranging from 0.001 to 100 and sphericity ranging from 0.471 to 1.

Yang *et al.* [79] performed experimental research on the settling of slender fibrous particles under the influences of multiple factors. The experiment was conducted inside a 1.8-meter-tall chamber with a square cross-section of 60 centimetres. A high-speed camera was set at the

side of the chamber to capture the fibres falling inside the chamber. Two LED light sources were used to illuminate the particle. The size of the fibres was divided into three groups with an average diameter of 125 μm, 175 μm and 237 μm and of lengths 5 mm, 10 mm and 20 mm, thus aspect ratios ranging between 21 to 160. Throughout the settling process, it was noted that the fibre particle did not experience any deformation, but there was a horizontal displacement and a change in the orientation angle as it settled. Additionally, as the diameter increases, the settling velocity also increases. An increase in diameter increases the gravitational force although the pressure drag increases simultaneously, however, the effect caused by the gravity forces is more obvious. For a geometrical property, the settling velocity of a fibre particle increases with the curvature degree. It is explained that the settling fibre can push the fluid in the front area, leading to a higher pressure in the front of the fibre and a lower pressure in the back area. The pressure difference can move the fluid from high to low-pressure areas. The fluid can flow to the back area around the two ends of the fibre particle. Additionally, the pressure difference between the front and back areas of the fibres is reduced, especially in the tip region and a drag force reduction is induced as well. When the curvature degree increases, the particle can fit more conformably with the streamlines. For a curved fibre particle, the projected area normal to the settling direction decreases and the drag force becomes smaller than the straight fibre particle.

Chapter 3

Experimental Details

Experiments were performed using a stereoscopic particle tracking velocimetry (PTV) technique to record the motion of straight and curved cylindrical rods falling through glycerine and water mixtures, which replicate the settling of microfibres in air. This setup was designed as a part of this research. All the components and equipment specifications used are listed in this chapter. The apparatus used to manufacture straight and curved brass rods are discussed, as well as the various glycerine and distilled water mixtures. The camera calibration process to map 2D pixel coordinates to 3D spatial coordinates is derived and explained in detail. At the end of the chapter, an experimental validation for a spherical particle is performed, including a comparison between the experimental and theoretical settling velocities.

3.1 Experimental Setup

3.1.1 Experimental Planning

The first step towards designing an appropriate experimental setup to emulate the settling of microfibers in water-glycerin mixtures using metal rods is determining the values of the relevant non-dimensional parameters. For particles settling in still air, the key parameter is the Reynolds number. As mentioned in Section 2.1, it was noted the common range of

microfibres captured in the atmospheric deposition were of lengths between 250 μm to 2000 μm with a typical diameter of 25 μm. These dimensions correspond to aspect ratios of 10 to 80, respectively. The densities of the microfibres were taken into consideration, from the lowest to the highest, polypropylene ($\rho = 0.92\text{g/cm}^3$) to poly-vinyl chloride ($\rho = 1.32\text{g/cm}^3$). Computation of the settling velocity, drag coefficient, and Reynolds number were calculated using a custom-designed program in MATLAB. The code was designed to have an iterative method that was based on related articles [17, 18, 19]. For the aforementioned range of the dimension of the microfibres, the Reynolds number lies within a range of 0.3 to 3.5, with the estimated settling velocity to be 0.09 m/s to 0.47 m/s in still air (based on Song *et al.* [17] for non-spherical particles). The intended range of Reynolds number was expanded between 0.1 to 10 to cover three orders of magnitude and to account for a wider range of fibres dimension as noted previously in Section 2.1.

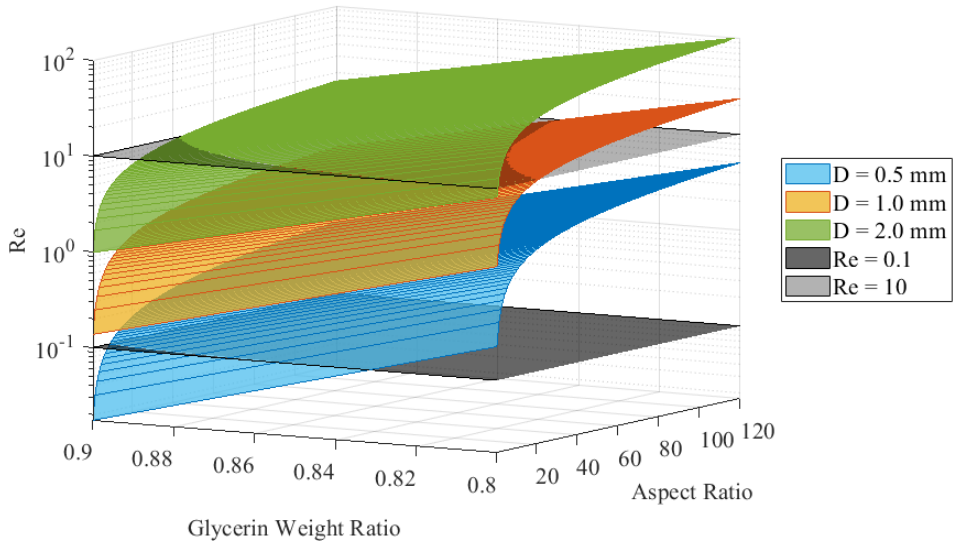

Figure 3.1: Roughly estimated Reynolds number of brass rods with different diameters and aspect ratios in water-glycerin mixtures with varying weight ratios at room temperature calculated using the general non-spherical particle model of Song *et al.* [17]. The grey planes are drawn at Re = 0.1 and 10 for reference.

Figure 3.1 depicts how the Reynolds number may vary in different glycerin/water mixtures at various aspect ratios using the model of Song *et al.* [17]. Only a limited range of glycerin/water mixtures for the brass rods is shown. Lower values than $GW_{80\%}$ (glycerin weight) led to Reynolds numbers greater than the interest for the present study. For mixture ratios greater than $GW_{90\%}$, the viscosity sensitivity significantly increases to temperature change becomes drastic [87], and therefore this was chosen as the maximum value. The range of aspect ratios shown are between 3-120. The bound of the Reynolds number are noted by two planes between 0.1 to 10 in grey.

Tables 3.1 and 3.2 present the variation of Reynolds number for rods of different diameters and aspect ratios as the glycerin-weight ratios vary from $GW_{80\%}$ to $GW_{90\%}$. These results are tabulated using the general non-spherical model developed by Song *et al.* [17]. These results provide insight into the selection of the optimal glycerin-weight ratio and demonstrate how the size of the rod affects the Reynolds number. It can be seen that an increase in particle size results in an increase in Reynolds number, while an increase in the glycerin-weight ratio leads to a decrease in Reynolds number.

Table 3.1: Computation of Reynolds number using the general non-spherical particle model of Song *et al.* [17] for rods of diameter 0.5 mm and aspect ratio 5 to 20 falling in glycerin weight ratios between $GW_{80\%}$ and $GW_{90\%}$.

Rod Diameter (mm)	Glycerin Weight Ratio	Aspect Ratio	Reynolds Number
0.5	$GW_{80\%}$	5	0.770
		10	1.208
		20	1.848
	$GW_{85\%}$	5	0.250
		10	0.405
		20	0.641
	$GW_{90\%}$	5	0.064
		10	0.105
		20	0.169

Table 3.2: Computation of Reynolds number using the general non-spherical particle model of Song *et al.* [17] for rods of diameter 1.0 mm and aspect ratio 5 to 20 falling in glycerin weight ratios between $GW_{80\%}$ and $GW_{90\%}$.

Rod Diameter (mm)	Glycerin Weight Ratio	Aspect Ratio	Reynolds Number
1.0	$GW_{80\%}$	5	4.497
		10	6.650
		20	9.639
	$GW_{85\%}$	5	1.690
		10	2.586
		20	3.850
	$GW_{90\%}$	5	0.480
		10	0.767
		20	1.190

3.1.2 Components of the Particle Tracking System

The particle tracking system utilizes a dual camera stereoscopic setup to measure the three-dimensional planer trajectory of the objects falling inside the glycerine fall chamber. The cameras are monochromatic Kaya Iron 250 CXP models that have a Sony Pregius IMX250 CMOS sensor. This model offers up to 5.01 megapixels at 155 frames per second using an 8-bit resolution. The resolution is 2448 by 2048 with a pixel size of 3.45 μm by 3.45 μm and a diagonal sensor size of 11.00 mm. Given the rectangular sensor size of the camera, it is positioned to maximize the imaging of the particles falling. The cameras were connected to the Komodo II four Channel CoaxPress 12 G Frame Grabber using coax cables. The frame grabber was installed on the motherboard of a computer via PCIe x16 slot. This

connection enables data transfer from the camera to the PC at rate up to 12.5 Gb/s. Vision Point image acquisition software was used to operate the camera and frame grabber. The setup is depicted in Figure 3.2.

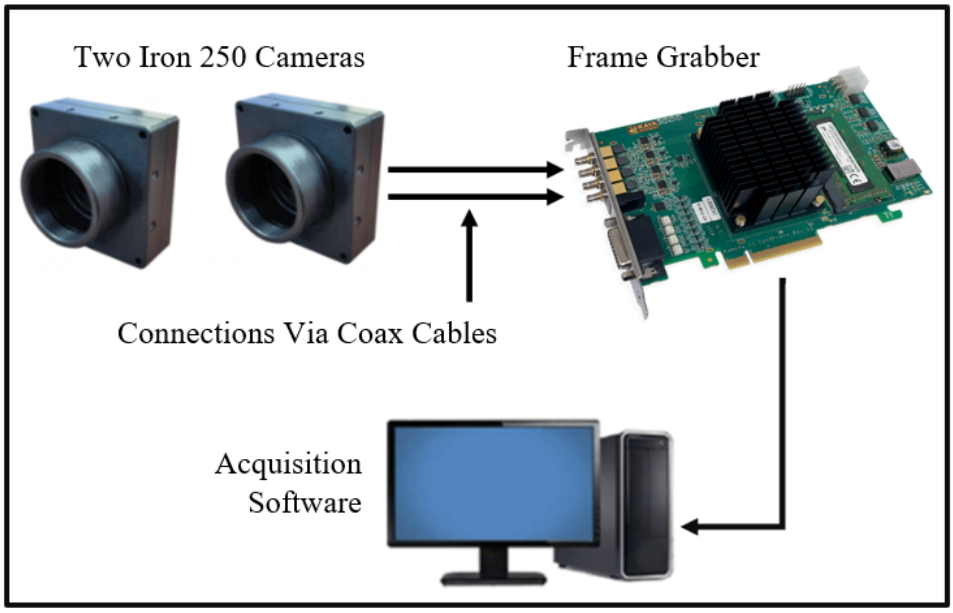

Figure 3.2: Diagram of the main components used for image acquisition where two Iron 250 Cameras are connected to a frame grabber which is installed on the motherboard of a PC.

The camera lenses selected were 2/3" C-Mount Basler models with a fixed focal length of 50 mm. The cameras were positioned approximately 0.9 m from the tank wall, as shown in Figure 3.3. The field of view was near the bottom of the tank where the rods had already achieved settling velocity. The vertical field of view was 15 cm. Based on the lens specification the distortion is approximately 0.12%. A naming convention of Camera 0 and Camera 1 are used to differentiate between the two cameras, which view the ZY and XY planes, respectively, as shown in Figure 3.3.

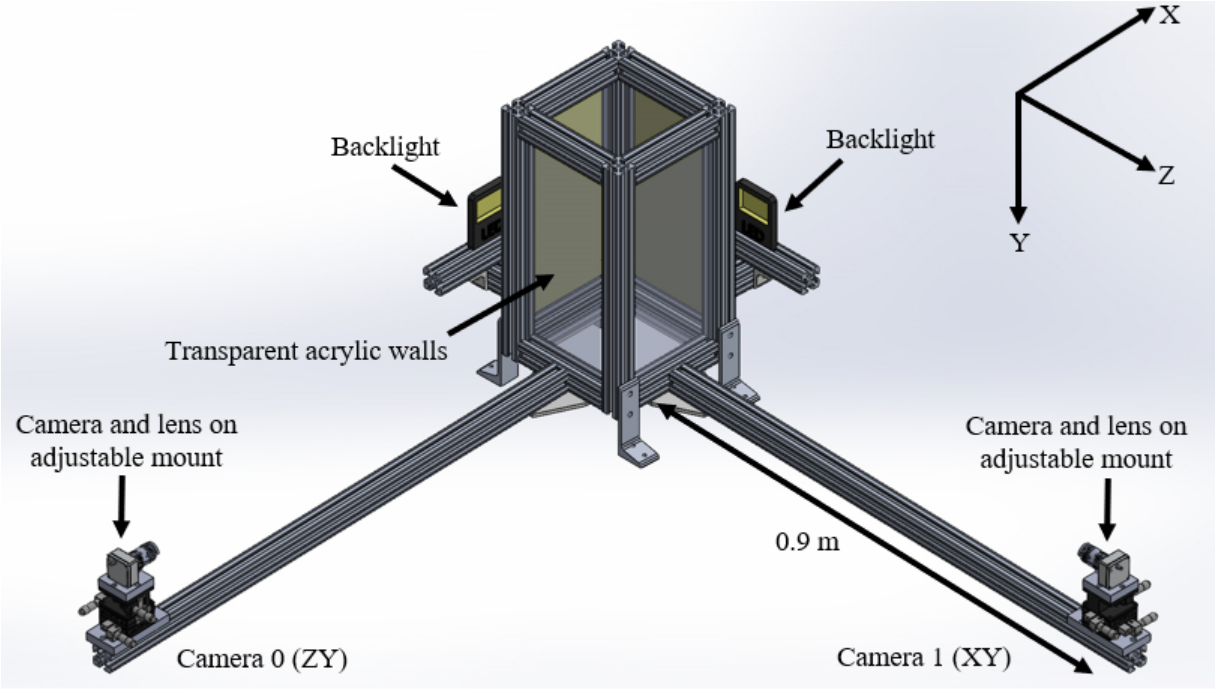

Figure 3.3: Schematic of the experimental setup showing the cameras relative to the tank, location for back-lighting, and scale. The yellow surfaces indicates where the backlighting technique is relative to the tank.

Each camera is mounted on top of a linear (XYZ) and rotation traverse with a 5/8" thick aluminum plate. The base of the linear traverse is secured and fastened to a 1.5" extruded aluminium rod with two 5/8" T-nuts using custom built 1" aluminum plate. The cameras are perpendicular and focus on approximately the same region within the tank. A T-type thermocouple of length 18" with a diameter of 1/8" interfaces with an Omega DPI 1/32" programmable temperature reader which was used to measure the glycerine mixtures. The temperature was required to determine the actual viscosity of the mixture during experiments. The fluid viscosity was corrected to the current temperature using correlations obtained from Cheng *et al.* [87]. Generally, the temperature was within 1.5 °C of what was initially calibrated (later discussed in Section 3.1.3).

The frame of the tank was constructed using 1.5" aluminum extrusions with dimensions where the interior of the tank is a rectangular space with a volume of 882 cubic inches. Clear acrylic sheets having a thickness of 6 mm were placed securely into the aluminum extruded slots and the base of the chamber. The interior edges were sealed using clear silicone. On the base of the chamber, a valve was installed to drain the tank.

The cameras were used to capture images of the rods that were back-lit using 10 Watt LED fog lights. To make the back-lighting intensity more uniform, the light was projected onto 1/16" thick white acrylic diffuser plates as shown in Figure 3.3. A mesh is placed at the bottom of the tank to collect the dropped rods. The mesh can be pulled up by strings in the corner of the tank, which were outside the area viewed by the cameras. To prevent any contaminants from the lab entering the chamber and evaporation of the water from the mixture, a double layer of Saran wrap is used to seal the opening of the tank, in addition to a hard lid when the tank was not in use.

3.1.3 Manufacturing Rods

The brass rods used in the experiments were purchased from K&S Metals. The rod diameters used are 0.5, 1.0, 1.5 and 2.0 mm. A Micromark ultra-smooth saw blade (effectively a jeweler's saw blade) was used to cut the rods to length. A summary of the rod diameters, length and corresponding aspect ratios are given in Table 3.3. A set of three rods were manufactured for each case to test for possible uncertainty caused by the manufacturing process, which is later discussed in detail in Section 4.1.1. A caliper was used to verify the desired length and each rod has a length tolerance of no more than 0.1 mm. The ends of each rod were sanded with a 400-grit sanding block down to the desired length tolerance. Figure 3.4 shows one test case of manufactured straight rods.

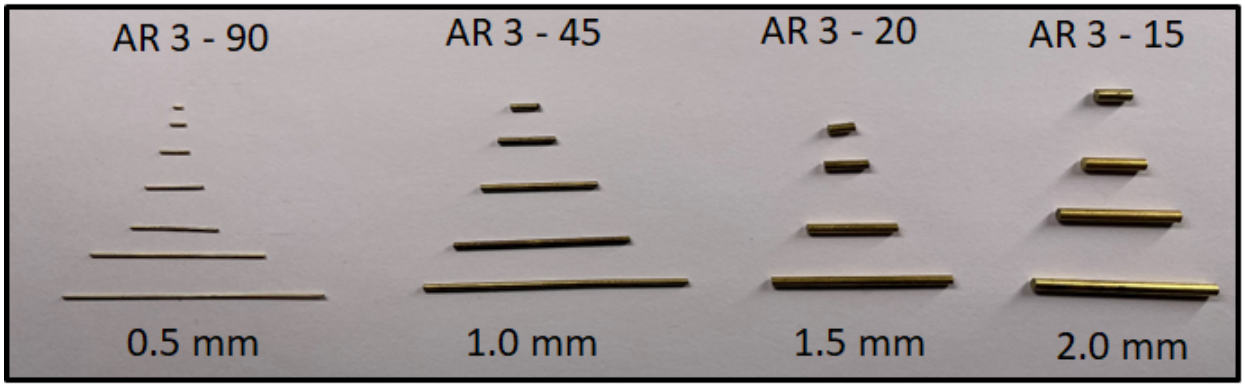

Figure 3.4: Set of straight rods used in the experiment with diameter of 0.5, 1.0, 1.5 and 2.0 mm for aspect ratios ranging between 3 to 90.

Due to the difficulty of curving thick and low aspect ratio rods, curved rods were only manufactured for 0.5 mm rods with AR 60 and 90 and 1.0 mm rods with AR 30 and 45 using the universal bender tool from Micromark. Rods were curved around a metal cylinder having different radius of curvature (RoC) (37.5 mm, 31.7 mm, 27.3 mm and 19.9 mm). Figure 3.5 shows the increasing trend of curvature of each test case and listed in Table 3.4. The effects of uncertainties of the rod dimensions are later discussed in Section 4.1.

For the curved rods, the projected area is calculated by measuring the projected length and multiplying it by the diameter of the rod. This process was done by taking an image of the rod profile over a calibration grid of known dimensions and mapping the pixels to spatial coordinates. For the rods with the same diameter and aspect ratio the projected area decreases with the radius of curvature. Table 3.5 summarizes the measured radius of curvature and projected area for the curved rods used in the present experiment.

Table 3.3: Test cases for straight rods. The values in the tables are the lengths of the rods for the various diameters and aspect ratios. The "-" represents a rod not manufactured for that condition.

Aspect	**Rod Diameter (mm)**			
Ratio	**0.5 mm**	**1.0 mm**	**1.5 mm**	**2.0 mm**
3	1.5 mm	3.0 mm	4.5 mm	6.0 mm
5	2.5 mm	5.0 mm	7.5 mm	10.0 mm
10	5.0 mm	10.0 mm	15.0 mm	20.0 mm
15	-	-	-	30.0 mm
20	10.0 mm	20.0 mm	30.0 mm	-
30	15.0 mm	30.0 mm	-	-
45	-	45.0 mm	-	-
60	30.0 mm	60.0 mm	-	-
90	45.0 mm	-	-	-
120	60.0 mm	-	-	-

Table 3.4: Test cases for curved rods. The values in the tables are the lengths of the rods for the various diameters and radius of curvature in millimeters.

Radius of Curvature (mm)	**Rod Diameter (mm)**	
	0.5 mm	**1.0 mm**
37.5	30 & 45 mm	30 & 45 mm
31.7	30 & 45 mm	30 & 45 mm
27.3	30 & 45 mm	30 & 45 mm
19.9	30 & 45 mm	30 & 45 mm

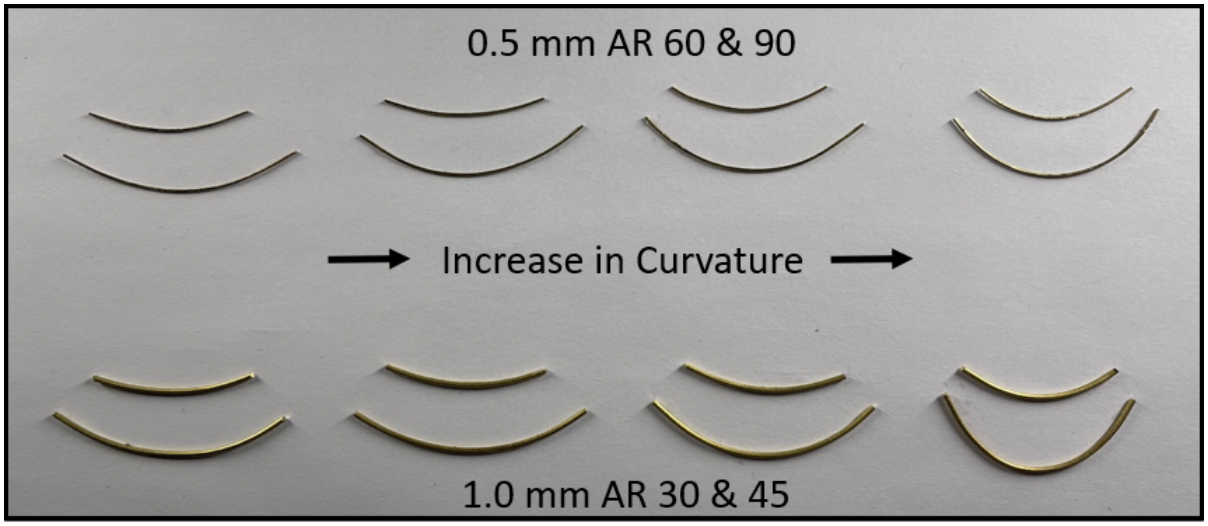

Figure 3.5: Manufactured curved rods for 0.5 mm diameters with AR of 60 and 90 and 1.0 mm diameter with AR of 30 and 45. The radius of curvatures increase from left to right starting at 37.5 mm, 31.7 mm, 27.3 mm and 19.9 mm, respectively.

Table 3.5: Measured projected areas for curved rods having different Radius of Curvature (RoC).

RoC	D=0.5mm AR60	D=0.5mm AR90	D=1.0mm AR30	D=1.0mm AR45
37.5 mm	14.71 mm^2	21.01 mm^2	28.86 mm^2	42.02 mm^2
31.7 mm	14.40 mm^2	20.01 mm^2	29.06 mm^2	41.98 mm^2
27.3 mm	14.17 mm^2	19.68 mm^2	22.87 mm^2	39.73 mm^2
19.9 mm	13.59 mm^2	18.43 mm^2	27.57 mm^2	33.64 mm^2

3.1.4 Glycerine Mixtures

The total volume of the glycerine fall chamber is 14.45 litres. To accommodate for its volume and any possible leakage or spills overtime, a total of 20 litres of each of the glycerine mixtures ($GW_{80\%}$, $GW_{85\%}$ and $GW_{90\%}$) were made and stored inside sealed buckets. Mixtures were made at a temperature of 20 °C with distilled water and 99.7% USP (United States Pharmacopeia) grade glycerine purchased from Ingredient Depot. A 100 mL sample was extracted from each mixture to measure the glycerine weight ratio mixture at 20 °C using the Discovery HR-3 Hybrid Rheometer as shown in Figure 3.6.

The recommended geometry for testing low to medium viscosity fluids, as are the mixtures of water and gylcerin considered, is the concentric cylinder accessory for the Discovery HR-3 Hybrid Rheometer. For this geometry, the three main components are the concentric cylinder, which magnetically locks to the base of the rheometer, the concentric cup where a fluid sample of approximately 22 mL is placed inside and the rotor conical that is screwed onto the top of the rheometer and rotors at various RPM at different shear rates. A clean syringe is used to transfer glycerine mixtures from the sample container to the concentric cup. The two tubes connected to the concentric cylinder circulates a fluid which controls the temperature of the concentric cup.

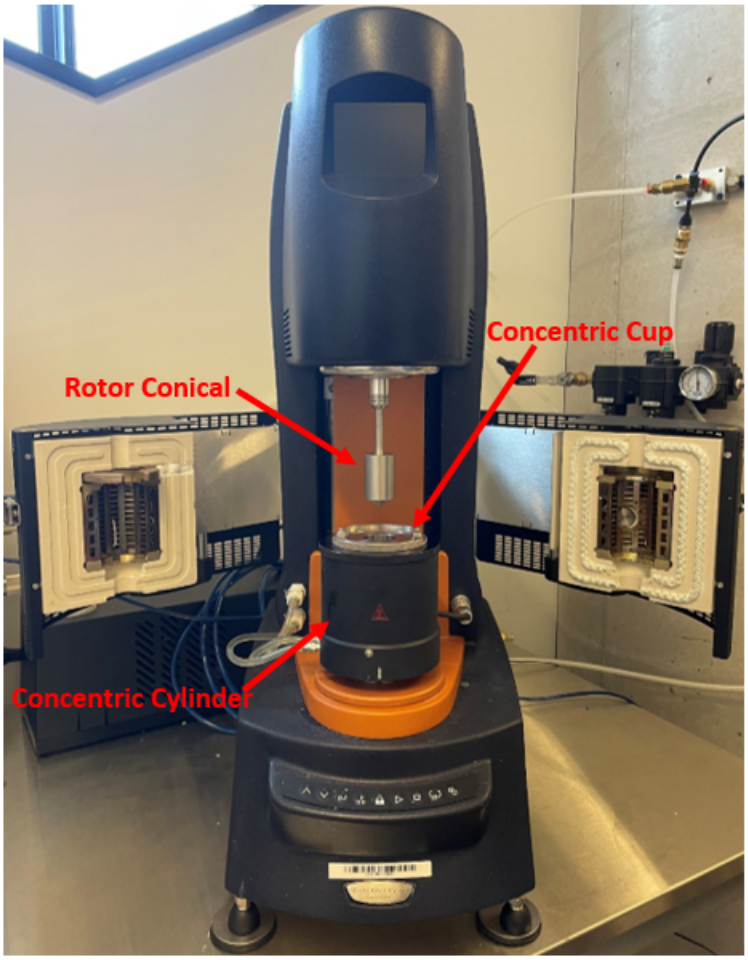

Figure 3.6: The Discovery HR-3 Hybrid Rheometer with the concentric cylinder geometry for very low to medium viscosity fluids.

To validate the accuracy of the measured viscosity for the Discovery HR-3 Hybrid Rheometer, an experiment was conducted using a calibration fluid from Cannon Instruments. The calibration fluid was N75 where the dynamic viscosity at 20 °C is 166.9 mPa·s (cP). This calibration fluid was chosen as it has similar viscosity as the glycerine mixtures used in the present experiment. The calibration fluid was tested at a shear rate of 1 - 200 1/s as shown in Figure 3.7.

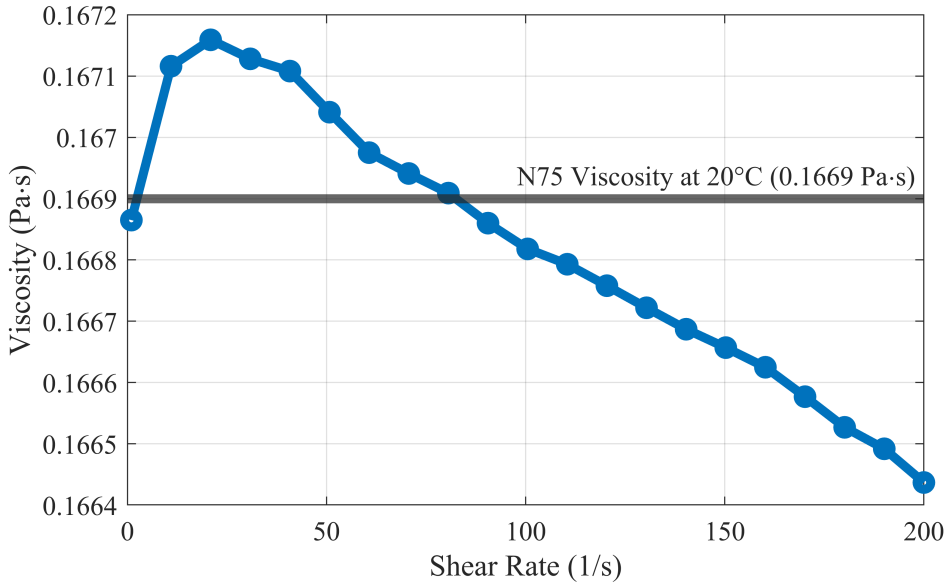

Figure 3.7: Variation of the measured viscosity of the standard N75 silicon oil conducted at a temperature of 20 °C over a range in shear rate from 1 to 200 s^{-1}. The data markers show the viscosity where the blue line shows the viscosity computed from the rheometer at the specific shear rate and the horizontal line indicates the manufacturer's specification of the N75 oil.

Figure 3.7 shows the measured viscosity of the N75 fluid over a shear rate of 1 - 200 s^{-1}. The solid line shows the value provided by the manufacturer. The graph above demonstrates slight inaccuracies measured by the rheometer where the dynamic viscosity is found to lie above and below the viscosity of the calibration fluid. The maximum value occurred at a shear rate of 30 s^{-1} where the dynamic viscosity is 0.16715 Pa·s while the minimum happened at the shear rate 200 s^{-1} where a dynamic viscosity of 0.16643 Pa·s was found and uncertainty of $\pm$ 0.0005 Pa·s. It can be concluded that there is 0.3% error for the viscosity measurement using this Rheometer. This error will be applied to the following viscosity measurements for the glycerin mixtures and will be accounted for in the total uncertainty of the experimental result in Chapter 4.

For glycerine and water mixtures ($GW_{80\%}$, $GW_{85\%}$, $GW_{90\%}$) the experiments were conducted at temperature at 20 °C at a linear shear rate from 1 - 200 s^{-1}, similarly to the N75 calibration fluid. Shear rates were kept within this range as at higher shear rates in the concentric cylinder viscous heating may occur. The results for the shear rate versus viscosity were plotted for the $GW_{80\%}$, $GW_{85\%}$ and $GW_{90\%}$ in Figure 3.8. The viscosity of the glycerine and water mixtures was determined to be the average of the data points within the range of shear rate between 0 and 200 s^{-1} as shown in Figure 3.8.

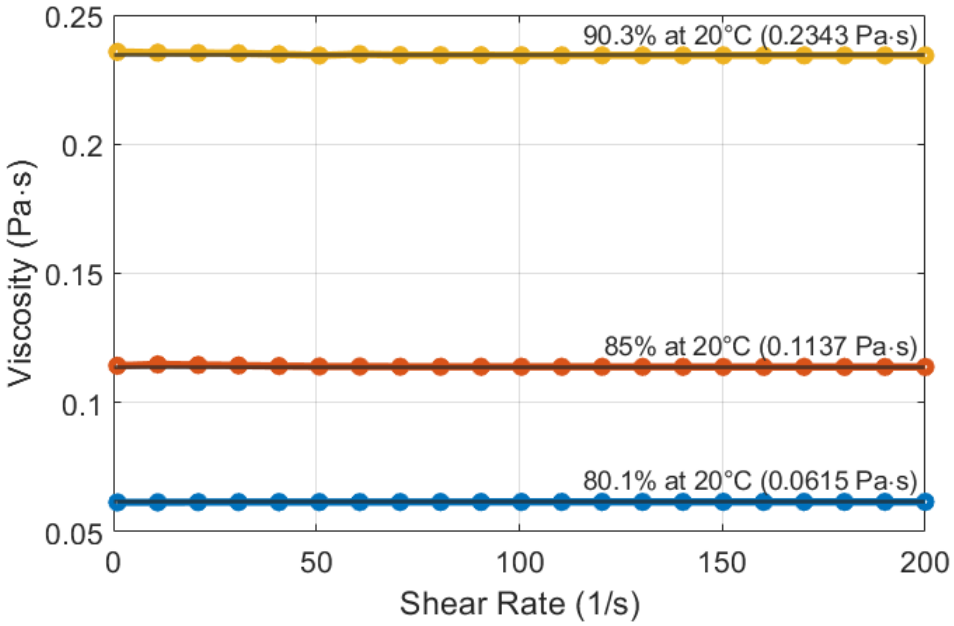

Figure 3.8: Variation of the measured viscosity of the $GW_{80\%}$, $GW_{85\%}$ and $GW_{90\%}$ mixture conducted at a temperature of 20 °C over a range in shear rate from 1 to 200 s^{-1}. The data markers show the viscosity where the blue line shows the viscosity computed from the rheometer at the specific shear rate and the horizontal line indicates the theoretical viscosity.

The results shown in Figures 3.8 demonstrate that the mixtures of water and glycerin have a slight deviation from the actual representation of a $GW_{80\%}$, $GW_{85\%}$ and $GW_{90\%}$ mixture as the theoretical results are lower than the values computed by the rheometer. The exact

weight ratio of the glycerin mixtures was determined by measuring the viscosity and was considered in the present analysis. Using linear interpolation of the viscosity of glycerine weight ratios, it was determined that the actual concentration of the $GW_{80\%}$, $GW_{85\%}$ and $GW_{90\%}$ are $GW_{80.1\%}$, $GW_{85.2\%}$ and $GW_{90.3\%}$, respectively. Considering the calibration error from the viscosity standard (N75) the $GW_{80.1\%}$, $GW_{85.2\%}$ and $GW_{90.3\%}$ mixtures have a dynamic viscosity of 0.06154 ± 0.0002 Pa·s, 0.11374 ± 0.0003 Pa·s and 0.23428 ± 0.0007 Pa·s, respectively. For simplicity, notation will be $GW_{80\%}$, $GW_{85\%}$ and $GW_{90\%}$.

3.2 Stereoscopic Calibration

The method for the stereoscopic calibration process was adopted and modified from that found in the literature [82, 83, 84, 85]. In summary, a leveled calibration grid is placed at a 45° angle inside the tank where all the points must be seen from both cameras and takes up the entire FOV. A reference point from the calibration grid is set (top left corner) and the code identifies each calibration point in pixel coordinates and index's them based on the row and column it is located. Through mathematical equation derived and modified from Soloff *et al.* [82] a surface plot function relating the height and the depth of each calibration point can map the 2D pixel coordinates seen from both cameras into world spatial coordinates. The methods and uncertainties are explained in further details below.

3.2.1 Calibration Grid

As a part of this research a custom code was designed and executed using MATLAB^{TM} to convert the coordinates in pixels, as seen from both cameras, and map them to spatial Cartesian coordinates. This is done by using a calibration grid. For this experiment a symmetrical circles calibration pattern was generated. The symmetrical circle pattern was specified to have 59 rows and 60 columns where the circles are spaced 2 mm apart from their centroids each having a diameter of 1 mm. The grid was printed and laminated onto a white

sheet of paper. The location of the points was verified from measurements done using a caliper. The calibration grid adhered to acrylic plate which was positioned on a 3D printed stand. The grid was placed in the center of the tank at an angle of 45° degrees relative to the chambers sides as shown in Figure 3.9 with the glycerine mixture. All the circles from the calibration grid are visible for the FOV of each camera. A single picture is captured from both cameras for the calibration.

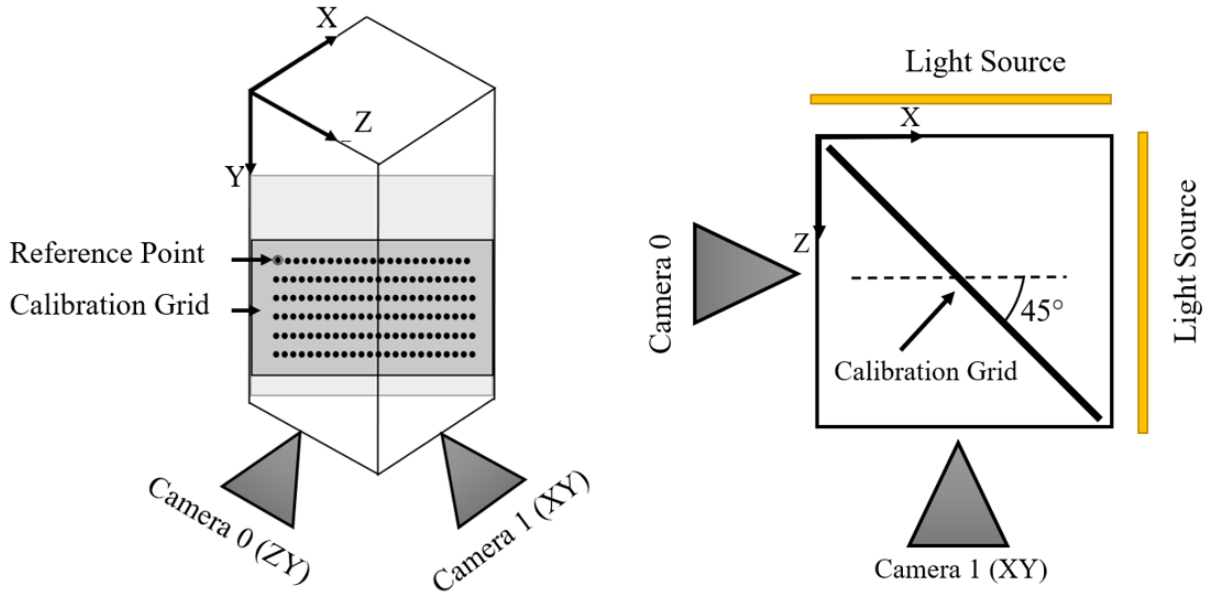

Figure 3.9: Schematic of the grid placement in the middle of the chamber and corresponding view from each camera. The reference point of the calibration grid is indicated on the top left corner.

3.2.2 Calibration Theory and Application

For the images taken of the calibration grid from Camera 0 and Camera 1 the top left circle on the grid was used as a reference point. This reference point is used as the starting location of the index for the locations of the circles on the grid. All other circles detected using the built in MATLAB function *detectCircleGridPoints()* are referenced to this location in terms of their pixel displacement as shown in Figure 3.10.

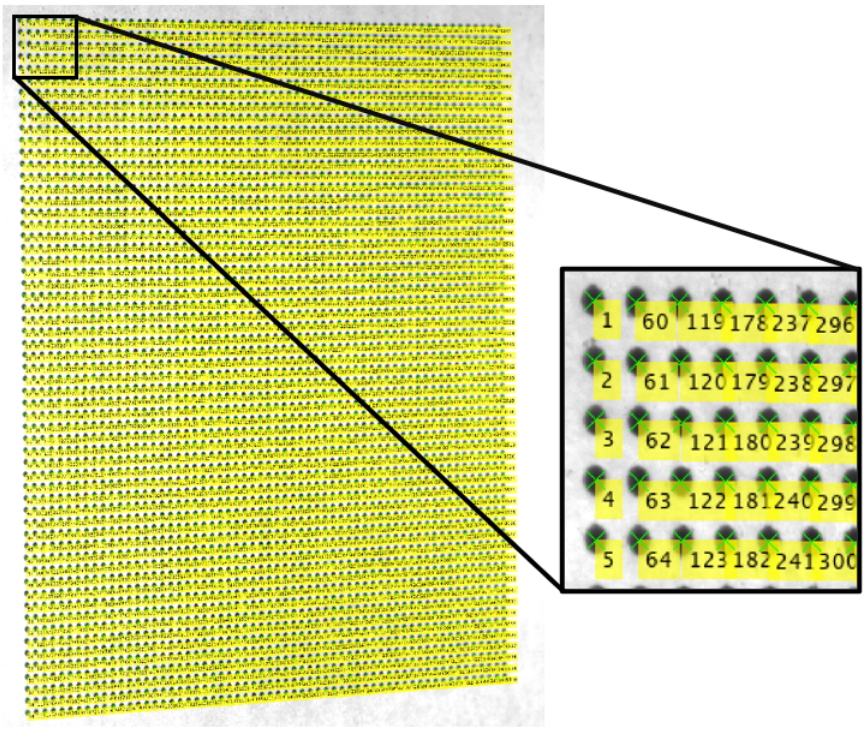

Figure 3.10: Calibration indexing for a symmetrical grid pattern having 59 rows and 60 columns for Camera 0. This procedure is also done for Camera 1 having a similar image.

The displacement between the circles in pixels, are converted into world spatial XYZ coordinates using four mapping functions. These mapping functions are 3D surface plots that are generated specifically for the images captured. These mapping function denoted F, can be expressed as a relation between pixel coordinates (X_i) and world spatial coordinates (x_i) where i = 1, 2, 3 ... as shown in Equation 3.1.

$$x_i = F(X_i) \tag{3.1}$$

The displacement between two circles on the calibration grid from pixel locations to world spatial coordinates (ΔX_i and Δx_i) can be expressed as Equation 3.2.

$$\Delta x_i = x_{1+i} - x_i = F(X_{i+1}) - F(X_i) \tag{3.2}$$

Using a condenses form of the Taylor's series expansion and by disregarding higher order terms (higher than 1), Equation 3.2 can be rewritten to Equation 3.3.

$$\Delta x_i = x_{1+i} - x_i = F(X_i) + \frac{\partial F(X_i)}{\partial X_i}\Delta X_i - F(X_i) = \frac{\partial F(X_i)}{\partial X_i}\Delta X_i \tag{3.3}$$

As a result, the world displacement (Δx_i) can be calculated by multiplying the gradient of the mapping function with the displacement in pixels (ΔX_i). For each camera, two components for the displacement are identified (ΔX_1 and ΔX_2 which are the horizontal and vertical displacements, respectively). Shown in Figure 3.9, the horizontal and vertical displacements captured by Camera 0 correspond to the world Δz and Δy, respectively. Similarly, the horizontal and vertical displacements captured by Camera 1 correspond to the world Δx and Δy, respectively. As two Δy values are observed from Camera 0 and Camera 1 where the difference was negligible. The average of the two Δy values is taken to reduce the uncertainty and to give an accurate result for the world vertical displacement.

This relation between the world XYZ displacement and pixel displacement for each camera is as follows, where F and F' are the mapping functions for Camera 0 and Camera 1, respectively:

$$\begin{bmatrix} \Delta z \\ \Delta y \end{bmatrix}_{Camera0} = \begin{bmatrix} F_{11} & F_{12} \\ F_{21} & F_{22} \end{bmatrix} \begin{bmatrix} \Delta X_1 \\ \Delta X_2 \end{bmatrix}_{Camera0} \tag{3.4}$$

$$\begin{bmatrix} \Delta x \\ \Delta y \end{bmatrix}_{Camera1} = \begin{bmatrix} F'_{11} & F'_{12} \\ F'_{21} & F'_{22} \end{bmatrix} \begin{bmatrix} \Delta X_1 \\ \Delta X_2 \end{bmatrix}_{Camera1} \tag{3.5}$$

Supposing a purely horizontal displacement as much as Δx_0 from one circle centroid in the calibration grid to the nearest circle's centroid, from Equation (3.5) we would obtain:

$$\begin{bmatrix} \Delta x \\ 0 \end{bmatrix}_{Camera1} = \begin{bmatrix} F'_{11} & F'_{12} \\ F'_{21} & F'_{22} \end{bmatrix} \begin{bmatrix} \Delta X_{1-0} \\ 0 \end{bmatrix}_{Camera1} \tag{3.6}$$

The Equation set (3.6) would result in:

$$F'_{11} = \frac{\Delta x_0}{\Delta X_{1-0}} \qquad\qquad F'_{21} = 0 \tag{3.7}$$

Similarly, applying a purely horizontal displacement of Δz_0 to Equation set (3.4) would lead to:

$$\begin{bmatrix} \Delta z \\ 0 \end{bmatrix}_{Camera0} = \begin{bmatrix} F_{11} & F_{12} \\ F_{21} & F_{22} \end{bmatrix} \begin{bmatrix} \Delta X_{1-1} \\ 0 \end{bmatrix}_{Camera0} \tag{3.8}$$

The Equation set (3.8) would result in:

$$F_{11} = \frac{\Delta z_0}{\Delta X_{1-1}} \qquad F_{21} = 0 \tag{3.9}$$

Considering a purely vertical displacement of Δy_0 to both Equation (3.4) and (3.5), respectively would lead to:

$$\begin{bmatrix} 0 \\ \Delta y_0 \end{bmatrix}_{Camera0} = \begin{bmatrix} F_{11} & F_{12} \\ F_{21} & F_{22} \end{bmatrix} \begin{bmatrix} 0 \\ \Delta X_{2-0} \end{bmatrix}_{Camera0} \tag{3.10}$$

$$F_{22} = \frac{\Delta y_0}{\Delta X_{2-0}} \qquad F_{12} = 0 \tag{3.11}$$

$$\begin{bmatrix} 0 \\ \Delta y_0 \end{bmatrix}_{Camera1} = \begin{bmatrix} F'_{11} & F'_{12} \\ F'_{21} & F'_{22} \end{bmatrix} \begin{bmatrix} 0 \\ \Delta X_{2-1} \end{bmatrix}_{Camera1} \tag{3.12}$$

$$F'_{22} = \frac{\Delta y_0}{\Delta X_{2-1}} \qquad F'_{12} = 0 \tag{3.13}$$

As a result, the relation between pixels and world spatial XYZ coordinates are defined below for Camera 0 and Camera 1 are Equations 3.14 and 3.15, respectively:

$$\begin{bmatrix} \Delta z \\ \Delta y \end{bmatrix}_{Camera0} = \begin{bmatrix} \frac{\Delta z_0}{\Delta X_{1-1}} & 0 \\ 0 & \frac{\Delta y_0}{\Delta X_{2-0}} \end{bmatrix} \begin{bmatrix} \Delta X_1 \\ \Delta X_2 \end{bmatrix}_{Camera0} \tag{3.14}$$

$$\begin{bmatrix} \Delta x \\ \Delta y \end{bmatrix}_{Camera1} = \begin{bmatrix} \frac{\Delta x_0}{\Delta X_{1-1}} & 0 \\ 0 & \frac{\Delta y_0}{\Delta X_{2-1}} \end{bmatrix} \begin{bmatrix} \Delta X_1 \\ \Delta X_2 \end{bmatrix}_{Camera1} \tag{3.15}$$

In Equations 3.14 and 3.15, Δz and Δx are the world displacements in Z and X direction

seen from Camera 0 and Camera 1 respectively. The world displacement, Δy is the vertical displacement, Y which is perceived by each camera separately where the average value is taken. ΔX_1 and ΔX_2 are the displacements in pixel from each camera. ΔX_{1-1} and ΔX_{1-0} are the horizontal distances between two adjacent centroids in pixels perceived by Camera 1 and Camera 0, respectively. Similarly, ΔX_{2-1} and ΔX_{1-1} are the vertical distances between two adjacent centroids in pixels perceived by Camera 1 and Camera 0, respectively. Lastly, Δz_0, Δy_0, Δx_0 are the world displacements between two nearby circle centroids on the calibration grid in the Z, Y and X directions, respectively shown in Figure 3.11.

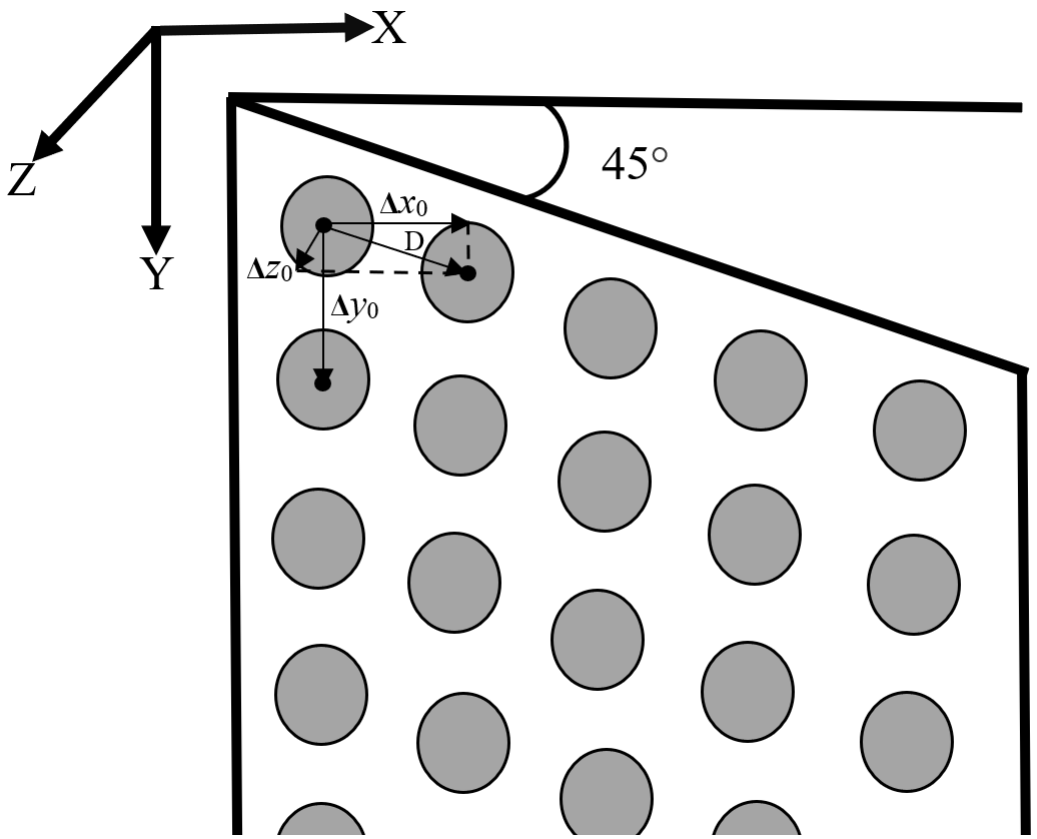

Figure 3.11: A schematic diagram of the calibration grid placed at an angle of 45 degrees showing the world spatial displacements, Δx_0, Δy_0 and Δz_0 between two circles centroids along the first row.

Given the spacing between each circles' centroid to be 2 mm and the angle of the grid placed at 45°, the Δx_0, Δy_0 and Δz_0 would be:

$$\Delta x_0 = D\cos(45) = 1.41 \text{ mm} \qquad \Delta y_0 = 0 \text{ mm} \qquad \Delta z_0 = D\cos(45) = 1.41 \text{ mm} \tag{3.16}$$

To determine the mapping functions for Camera 0 and Camera 1, two non-zero indices for each mapping matrix (F_{11}, F_{22}, F'_{11}, F'_{22}) in Equations 3.11 and 3.13 are determined considering all the circles' centroids lying on the calibration grid with respect to Equations (3.7) and (3.9). Due to perspective effects and the lens distortion in the vertical direction (y direction), the values F_{11}, F_{22}, F'_{11}, and F'_{22} are functions of the calibration grid image depth and vertical position (X_2) in pixels. The depth value is taken from the opposing camera. For instance, the depth of points in the image taken from Camera 0 is taken from the (X_1) values from Camera 1 and vice versa for the image taken by Camera 1. As a result, 3540 data points are considered using the calibration grid having different depths and (X_2) positions. Lastly, four different 5^{th} order polynomial functions are fitted using the calibration grids data and the surface fitting function in MATLAB^{TM}. An example of the data points and the corresponding fitted surface is shown in Figure 3.12.

3.2.3 Accuracy of Calibration

To assess the accuracy of the calibration procedure, the Sum of Squares due to Error (SSE), R-squared and Root Mean Square Error (RMSE) were evaluated and summarized for the generated mapping functions in Table 3.6. From the RMSE values it shows that the data points from the calibration grid are concentrated precisely on the surface function. The R-squared values show that the scatter of data point lies very close to the regression function making it a suitable correlation to map the camera's pixel coordinates to spatial XYZ coordinates.

The fit of the mapping functions was assessed over the calibration grid selected to compute the world displacement using the four generated mapping functions. Three different reference points were selected (the very top, the middle, and towards the end) where the displacement

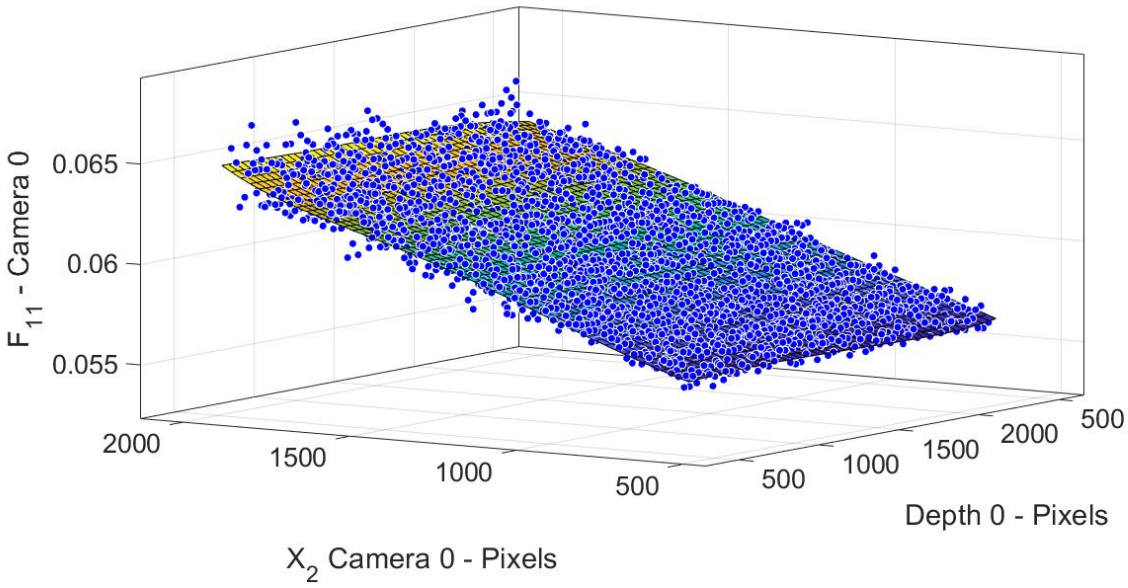

Figure 3.12: Mapping function F_{11}, generated for Camera 0 as a function of height and depth. Mapping functions F_{22}, F'_{11} and F'_{22} are of similar nature.

Table 3.6: Evaluating of SSE, R-Square and RMSE 5^{th} order polynomial mapping functions produced from the calibration procedure.

Mapping Function	SSE	R-Square	RMSE
Camera 0 - F_{11}	0.001108	0.9623	0.0005709
Camera 0 - F_{22}	0.0006273	0.9342	0.0004295
Camera 1 - F'_{11}	0.001329	0.9512	0.0006251
Camera 1 - F'_{22}	0.0008945	0.9079	0.0005128

was computed diagonally between 1, 5, 10 and 15 circles apart as shown in Figure 3.13. Compared to the theoretical values, the percentage error from the code-derived values utilizing the four produced mapping functions is extremely comparable. The trend shows the further the circles are apart the lower the percentage error. This can be justified since the algorithm tries to identify the centroid of each circle which leads to higher errors when circles are close by. The mapping functions plots also appear as smooth linear planes. A single value for the uncertainty of the fit was computed to be 1.35% which was done by comparing the actual

and computed distance for each dot along the grid where the maximum error was 1.96%.

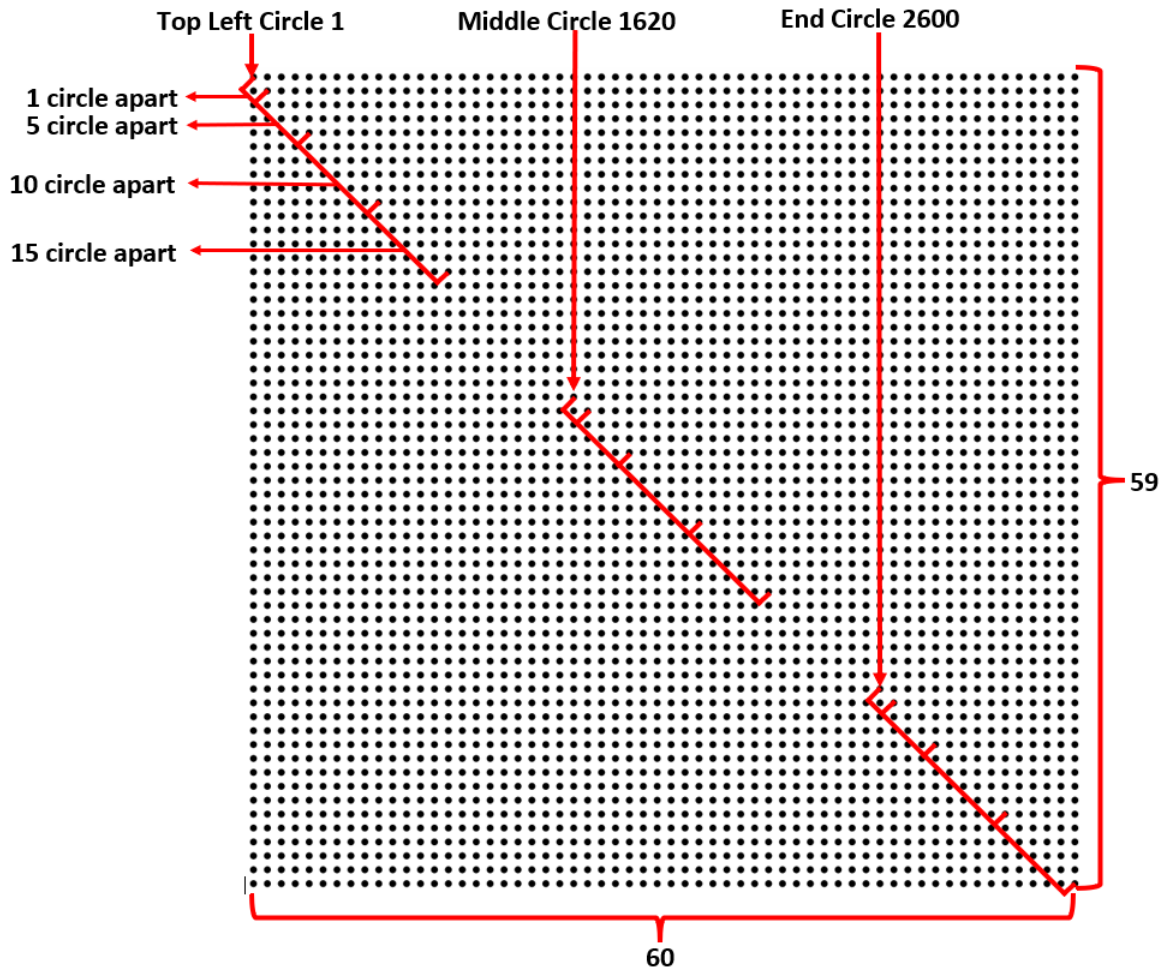

Figure 3.13: Schematic of three displacements for evaluating the accuracy of calibration matrix.

3.3 Image Processing

3.3.1 Image Analysis

Image analysis is performed using the MATLAB^{TM} Image Processing Toolbox. Images are preprocessed before analysis. The first image without the particle in view (see Figure

3.14 (a)) is subtracted from each image (for example, Figure 3.14 (b)) to improve image contrast. The background-subtracted image is converted to a binary image, where the particle is isolated with white pixels, and the rest of the image is black, as shown in Figure 3.14 (c). Further preprocessing is performed. For example, possible minor bubbles or contaminants that were illuminated and shown as isolated regions of white pixels were eliminated using a function that detects small white pixel groups (values of 1) and sets them as black (values of 0). Figure 3.15 shows an example of this. It is crucial that only the rod is shown in white pixels and the rest of the image is black, as other white pixels interfere with angle and centroid detection. The last step applied is the application of the function *regionprops()* to determine the centroid, orientation, and major and minor axis length of the white pixel region representing the rod in the image.

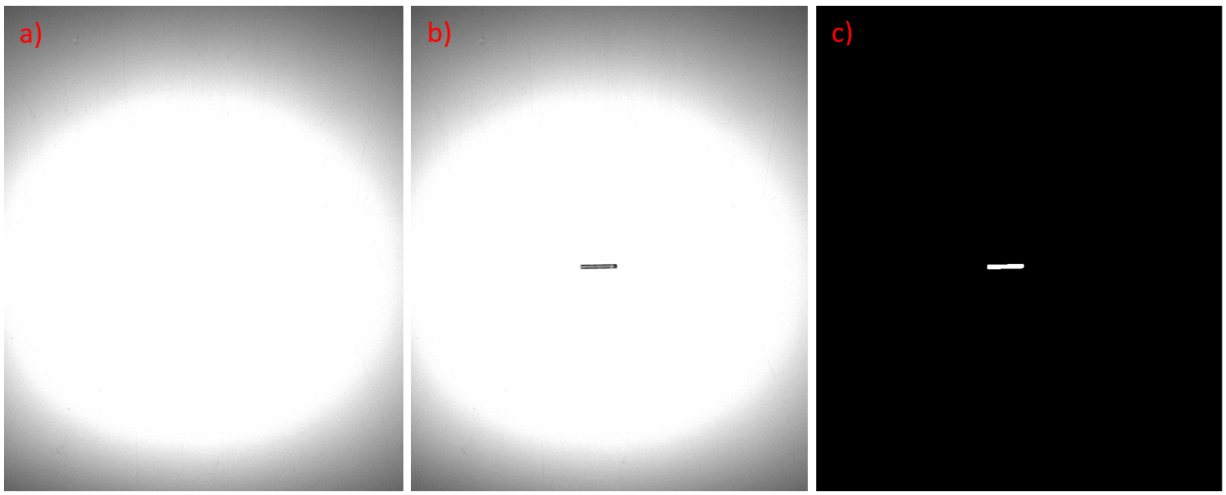

Figure 3.14: Background subtraction process for a 1.5 mm rod dropped horizontally with an AR of 10. a) shows the image referenced for background subtraction with no particle inside in frame. b) image with the particle falling in frame. c) background subtraction between image a) and b) to isolate and show the rod in white pixels.

The end points in pixels of the rod, represented by the white region in the image, are determined using the function *feretProperties()*. An example outcome is shown in Figures 3.16 and 3.17, where a yellow line is drawn from the end points and through the centroid of the rods from the images acquired with the rod in view. The centroid locations and the

orientation values from each camera are saved in a matrix to be used later to create an augmented reality of the rod (or sphere, or curved rod) falling in 3D space.

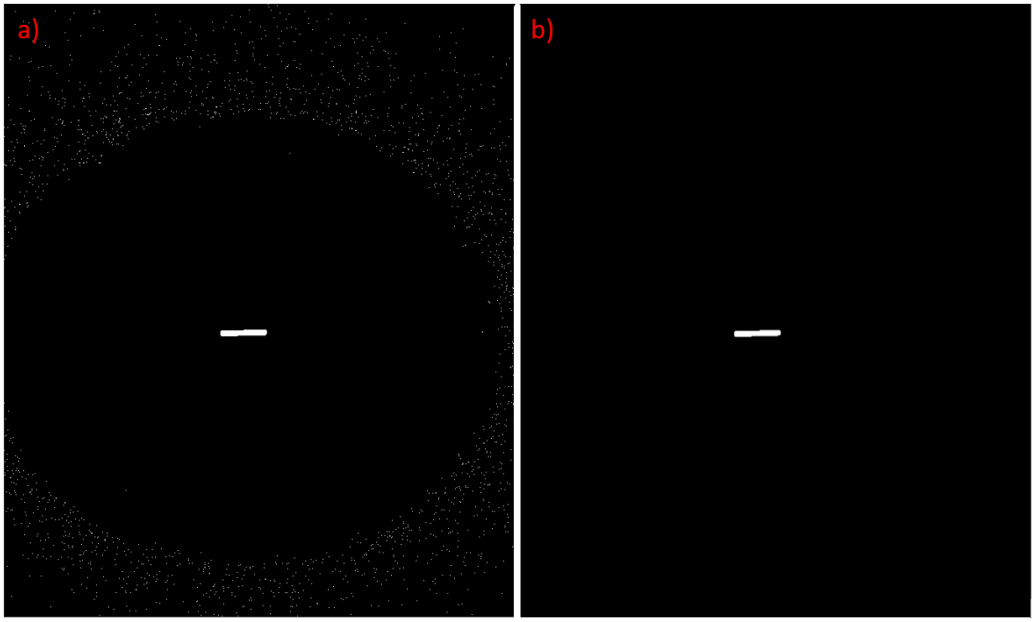

Figure 3.15: Eliminate of noise for a 1.5 mm rod dropped horizontally with an AR of 10 using the "*strel()*" function. a) Showcase the white noise situated at the edge of the image. b) The white noise is eliminated where the white pixels are only the rods position.

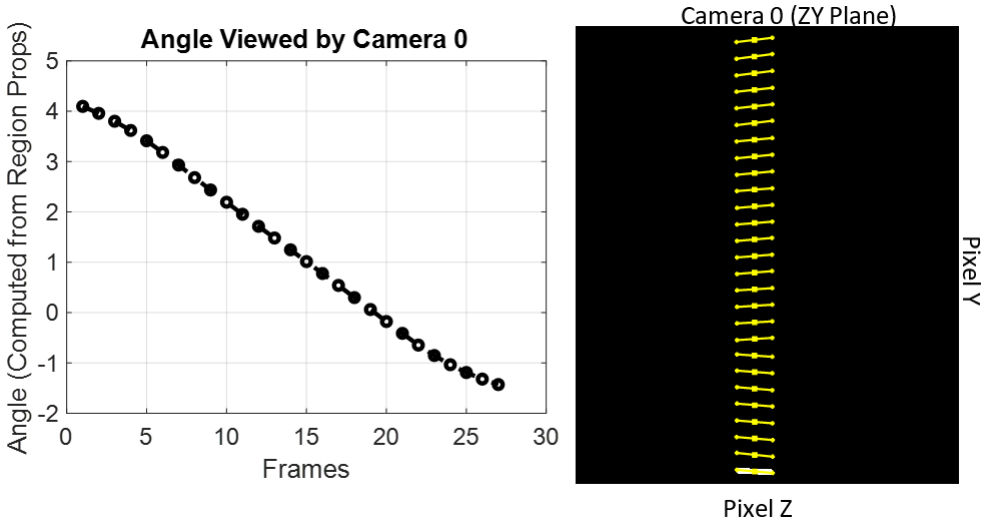

Figure 3.16: Image analysis for a 1.5 mm rod with AR 10 falling in the view of Camera 0.

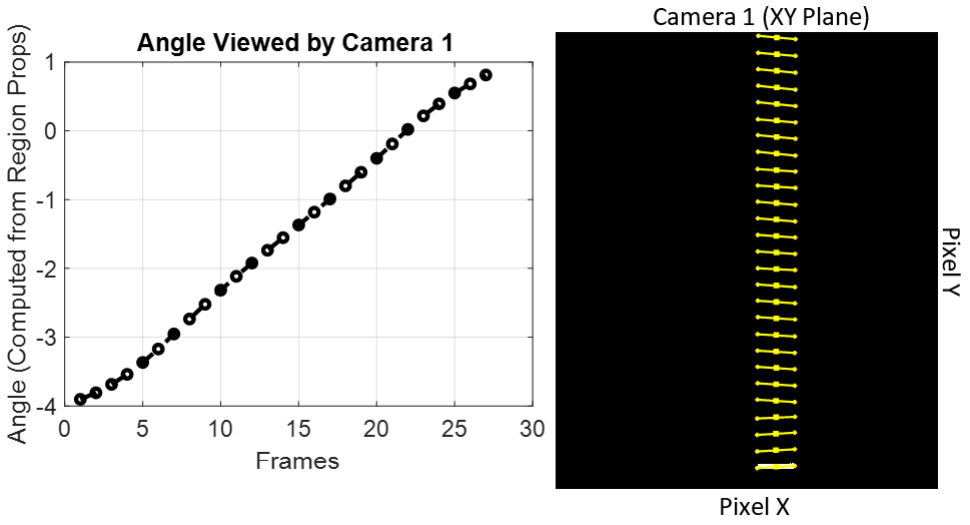

Figure 3.17: Image analysis for a 1.5 mm rod with AR 10 falling in the view of Camera 1.

3.3.2 Projected Area

The orientation angle computed from each camera does not reflect the inclination angle of the rod falling to compute the projected area, however, it is the angle perceived from each camera for that plane; hence why the values are different as shown in Figure 3.16 and 3.17. The inclination angle at which the rod is tilted is determined for each frame by determining the endpoint and angle of orientation from both Camera 0 and Camera 1. The equations provided later explain how the endpoints of the rod are located.

The centroid of the rod in XYZ coordinates (C_X, C_Y, C_Z) as shown in Figure 3.18 is computed using the mapping function determined from the calibration procedure for the ZY and XY pixel coordinates obtained from the Camera 0 and Camera 1, respectively. Using the orientation angle of the rod computed from Camera 0 and Camera 1 (θ_1), the XYZ coordinates for the endpoints (A_X, A_Y, A_Z) and (B_X, B_Y, B_Z) of the rod are calculated where L is the length of the rod shown in Equations 3.17 and 3.18.

$$
\begin{aligned}
A_X &= C_X + (\frac{L}{2}\sin\theta_0)\cos\theta_1 \\
A_Y &= C_Y - (\frac{L}{2}\sin\theta_0)\sin\theta_1 \\
A_Z &= C_Z + \frac{L}{2}\cos\theta_0
\end{aligned}
\tag{3.17}
$$

$$
\begin{aligned}
B_X &= C_X - (\frac{L}{2}\sin\theta_0)\cos\theta_1 \\
B_Y &= C_Y + (\frac{L}{2}\sin\theta_0)\sin\theta_1 \\
B_Z &= C_Z - \frac{L}{2}\cos\theta_0
\end{aligned}
\tag{3.18}
$$

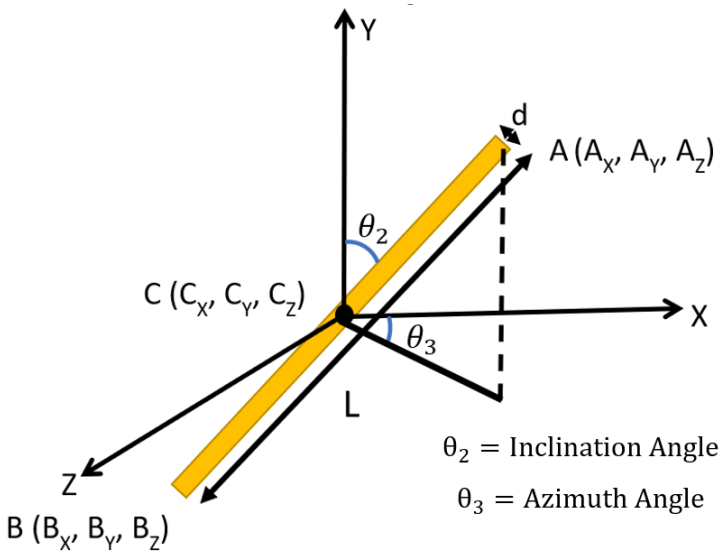

Figure 3.18: A visual representation of a cylindrical rod falling indicating the Inclination Angle (θ_2) and Azimuth Angle (θ_3)

Using the endpoints, the vector between B and A is computed and the by rearrangement of the $\hat{j}$ component is used to compute the inclination (θ_2) and azimuth angle (θ_3) using Equations 3.19.

$$\begin{aligned} \overrightarrow{BA} &= (A_X - B_X)\hat{i} + (A_Y - B_Y)\hat{j} + (A_Z - B_Z)\hat{k} \\ \overrightarrow{BA} \cdot \hat{j} &= |BA| \cos\theta_2 \;\rightarrow\; \theta_2 = \cos^{-1}(\frac{A_Y - B_Y}{L}) \\ \theta_3 &= \tan^{-1}(\frac{A_Z}{A_X}) \end{aligned} \tag{3.19}$$

Using this inclination angle, the instantaneous projected area (area normal to direction of fall in Equations 3.20) of the cylinder is used to compute the instantaneous drag coefficient C_D.

$$A_{projected} = dL \sin\theta_2 + \pi(\frac{d}{2})^2 \cos\theta_2 \tag{3.20}$$

Equation 3.20 is the projected area of a fibre in the direction of fall, as was also done by Qi *et al.* [74]. The first part of Equation 3.20 represents the rectangular area under the cylinder while the second component is the circular area for the ends of the cylinder. The projected area computed while the rod fell horizontally equals the diameter multiplied by the length of the rod.

3.3.3 Three Dimensional Trajectory

Recalling back to the PTV experimental setup, the utilization of two cameras enables the recreation of the three-dimensional trajectory for particles falling. The 3D trajectory of the particles falling is visualized in Figure 3.19. In this figure, the origin of (0, 0, 0) mm is at the first position of the particle taken in the first set of images with the entire rod in view. Practically, this location is approximately in the center of the tank in the X-Z plane and after the rod had already fallen through a depth of approximately 310 mm. Over the duration shown, the rod falls a distance of approximately 140 mm. The FOV of each camera is approximately 150 mm, however, the data nearest the top or bottom of the frame must be omitted when the rod is not in full view in each frame. The three-dimensional trajectory is then used to find the velocity as a function of time. This is done by knowing the time interval between two consecutive images (1/FPS). The final reported settling velocity is considered

to be the average of the last ten computed velocity points over the particle trajectory and approaches a constant value. This constant value is reached before the rod appears in the field of view of the camera.

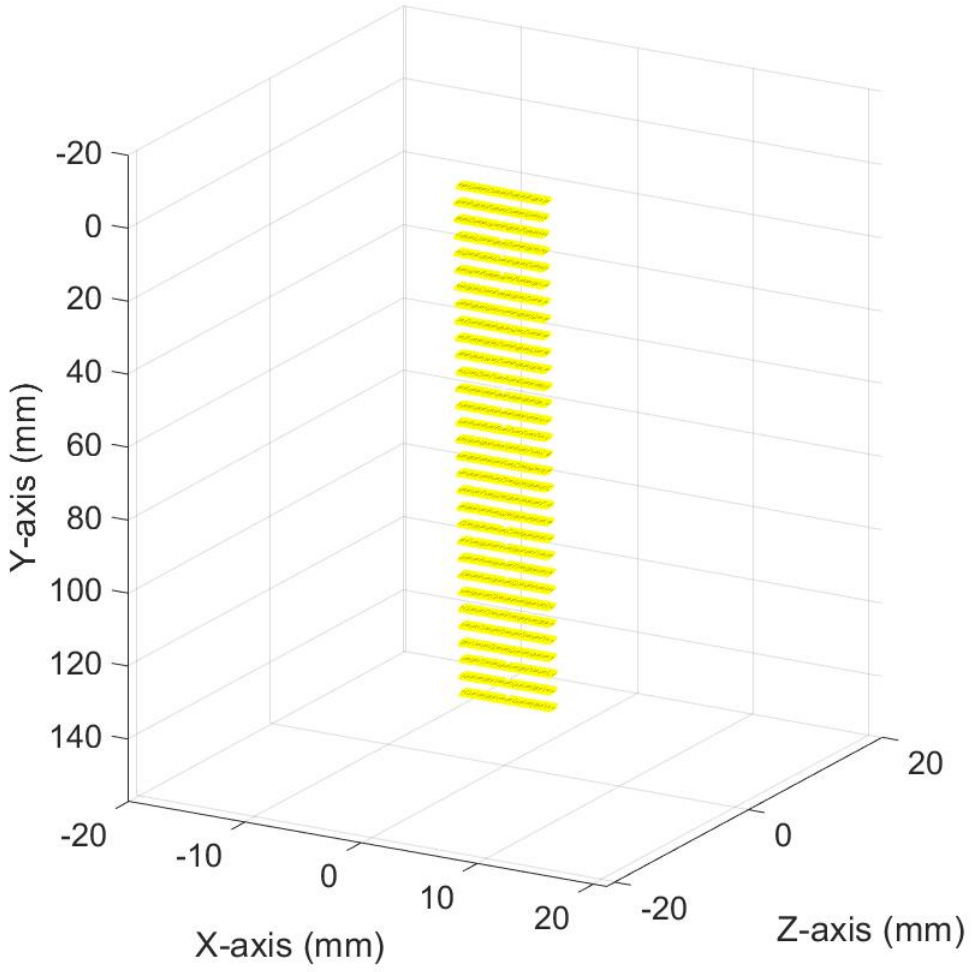

Figure 3.19: Three-dimensional trajectory of a 1.5 mm diameter brass rod cylinder with AR 10 dropped horizontally.

3.3.4 Modelling Curvature

In order to model the 3D trajectory for the curved rods, a MATLAB function called "*tubeplot()*" was used. The approach taken is to capture a picture of the curved rods from a bird's eyes view perspective on a white background. Imagine analysis is done on the picture changing it binary where the white pixels show the outline of the rod. As shown in Figure 3.19 a 4th-order polynomial is used to model the curvature of the white pixels outline in red. The bottom of Figure 3.20 shows modeling of the geometry of the curved rod. This figure is used to help the demonstration of the curved rods' trajectory.

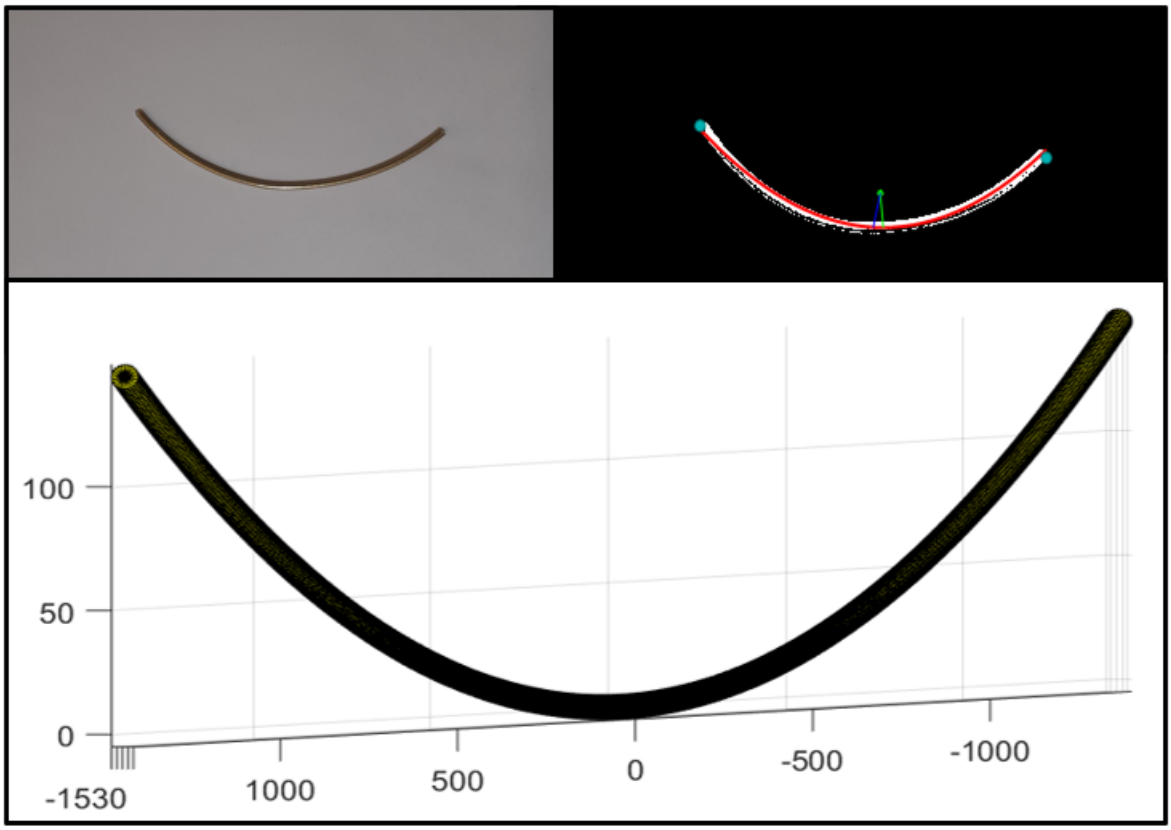

Figure 3.20: Procedure to model curved cylindrical rods showing that the original image (top left), the binary image where the red polynomial models the curvature (top right) and the 3D model of the curved rod (bottom).

3.3.5 Experimental Validation

As mentioned in Chapter 2, PTV experiments can be experimentally validated by tracking a spherical particle and comparing the Reynolds number and settling velocity with theoretical Equations 2.8 and 2.14. As shown in Figure 3.21, a brass ball bearing was used as the calibration particle. The density of this particle is 8730 kg/m^3 and it had a diameter of 1/16" (1.57 mm). This particle was dropped in both $GW_{85\%}$ and $GW_{90.3\%}$ glycerine weight ratio mixtures with water three times and averaged at a temperature of 19.5 °C and 20.3 °C, respectively. The corresponding fluid density and fluid viscosity at these temperatures for the $GW_{85.2\%}$ and $GW_{90.3\%}$ are 1222.5 kg/m^3 and 0.1209 kg/m-s, and 1235.5 kg/m^3 and 0.2290 kg/m-s, respectively. By applying Equations 2.8 and 2.14 the settling velocity for the brass sphere in $GW_{85\%}$ glycerine weight ratio is 83.40 mm/s and the Reynolds number is 1.324. Likewise, the settling velocity for the brass sphere in $GW_{90\%}$ glycerin weight ratio is 43.96 mm/s with a corresponding Reynolds number is 0.372. Tables 3.7 and Table 3.8 compare the theoretical results to the experimental results.

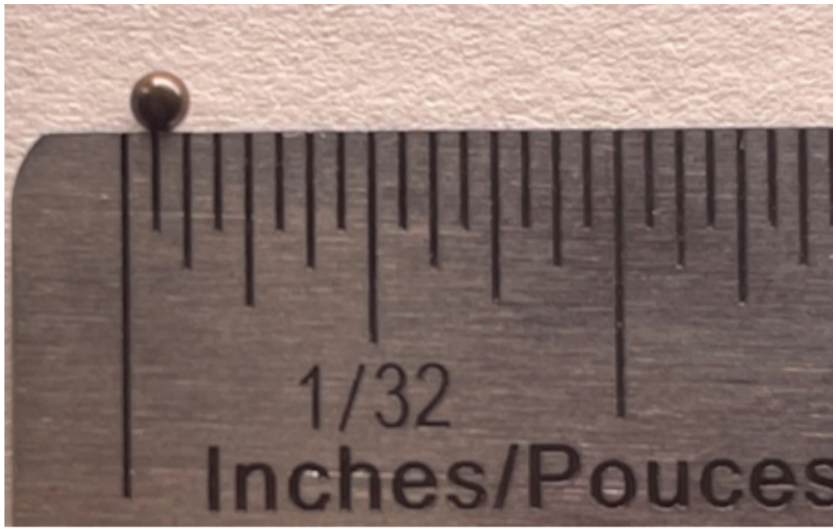

Figure 3.21: A brass spherical particle of diameter 1/16" used a calibration particle to validate the experiment.

Table 3.7: Comparison of the settling velocity for a spherical particle using theoretical values with recorded experimental values.

GWR %	Theoretical Vel. (mm/s)	Experimental Vel. (mm/s)	% Difference
85	83.40	82.32	1.29
90	43.96	44.33	0.84

Table 3.8: Comparison of the Reynolds number for a spherical particle using theoretical values with recorded experimental values.

GWR %	Theoretical Re Number	Experimental Re Number	% Difference
85	1.324	1.3091	1.12
90	0.3720	0.3779	1.58

Table 3.7 and 3.8 above shows that the experimental values reflect theoretical equations due to a low percentage error and concludes that the experimental setup is validated and measurements for cylindrical and curved rods will demonstrate accurate results. This error does not consider uncertainties. Carranza *et al.* [69] mentioned that spherical particles deviate from the path of a straight line as the Reynolds number increases from 15 to 648. As the values for the $GW_{85\%}$ glycerin is pasted the Stokes Regime, this effect can be shown in Figure 3.22.

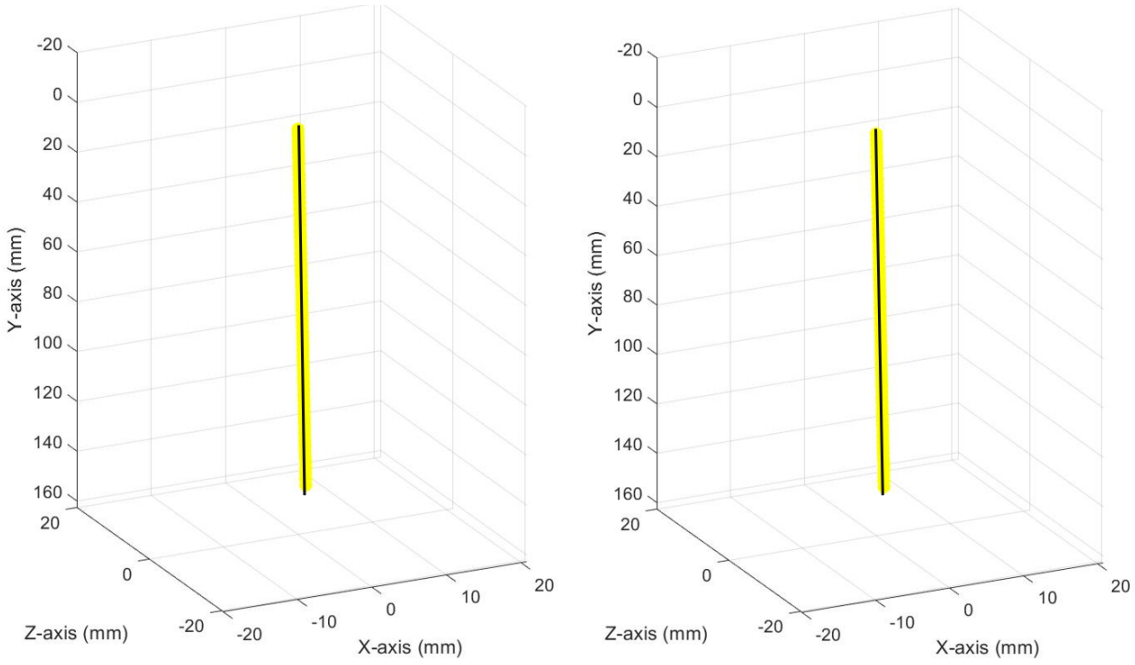

Figure 3.22: 3D Trajectory for a spherical particle in $GW_{90\%}$ (left) and $GW_{85\%}$ (right), showing the horizontal drift at the larger Re value for $GW_{85\%}$.

Chapter 4

Results and Discussion

In this chapter the experimental measurements of the settling of straight and curved rods are presented. In the following section, an analysis of the contribution of the various sources of experimental uncertainties is made. Next, results pertaining to straight rods are presented followed by the results pertaining to curved rods. Focus is given to the relationship between the drag coefficient and Reynolds number, given the significance of the relation for modeling.

4.1 Experimental Uncertainties

The main sources of uncertainties associated with the measurements made and quantities discussed are (a) the length of the manufactured rods ($\pm$ 0.1 mm), (b) the viscosity of the glycerin (0.3%), (c) temperature difference of the glycerin ($\pm$ 0.1 °C), (d) the density of the brass cylindrical rods ($\pm$ 49 kg/m^3), (e) and the particle tracking system for velocity measurements. The experimental uncertainties are summarized in Table 4.1.

Table 4.1: Main sources of the experimental uncertainties and their relative values.

Experimental Uncertainty	Quantified uncertainty
Length of the rod	± 0.1 mm
Viscosity of glycerin weight ratio	0.3 %
T-type thermocouple probe	± 0.1 °C
Density of brass rod	± 49 kg/m^3
Average Velocity error	0.72 %

Each rod was measured with a caliper having a resolution of 0.01 mm to ensure that the length of the rod was within the specified tolerance. The uncertainty of the viscosity of the glycerin was based on the test performed for the calibration fluid as previously explained in Chapter 3. The change in temperature influences the viscosity and to a lesser extent the density of the fluid. To determine the density uncertainty of the rod, five 1.0 mm rods at a length of 30 cm were weighed using a Mettler Toldeo MS54S scale, and a standard deviation of ± 49 kg/m^3 was calculated resulting in a 0.561% error assuming the density of the brass rods to be 8730 kg/m^3. The velocity uncertainty in each test was calculated by evaluating the standard deviation of at least ten values of computed velocity after the particle reached the settling velocity. The second contribution towards the velocity error is from the calibration. The root mean square of these two velocity error sources have been considered to calculate the total velocity error.

The Reynolds number and drag coefficient depend on several parameters. The uncertainty of Reynolds number and drag coefficient is calculated by using the square root of the sum of squares as described in Equation 4.1 [80].

$$\sigma_q = \sqrt{\left(\frac{\partial q}{\partial x_1}\sigma_{x_1}\right)^2 + \left(\frac{\partial q}{\partial x_2}\sigma_{x_2}\right)^2 + \cdots + \left(\frac{\partial q}{\partial x_n}\sigma_{x_n}\right)^2} \tag{4.1}$$

In the Equation 4.1, x represents the independent variable and q represents dependant variables. σ_x and σ_y are the uncertainty (standard deviation) of the independent variables and σ_q is the standard deviation of the dependent variables. In this study, q is the Reynolds number or drag coefficient and x is the independent variable involved in those equations. Therefore, the standard deviation of σ_{Re} and σ_{C_D} are presented in Equation 4.2 and 4.3, respectfully.

$$\sigma_{Re} = \sqrt{(\frac{\partial Re}{\partial L}\sigma_L)^2 + (\frac{\partial Re}{\partial \mu}\sigma_\mu)^2 + (\frac{\partial Re}{\partial \rho}\sigma_\rho)^2 + (\frac{\partial Re}{\partial V}\sigma_V)^2 + (\frac{\partial Re}{\partial T}\sigma_T)^2} \tag{4.2}$$

$$\sigma_{C_D} = \sqrt{(\frac{\partial C_D}{\partial L}\sigma_L)^2 + (\frac{\partial C_D}{\partial \mu}\sigma_\mu)^2 + (\frac{\partial C_D}{\partial \rho}\sigma_\rho)^2 + (\frac{\partial C_D}{\partial V}\sigma_V)^2 + (\frac{\partial C_D}{\partial T}\sigma_T)^2} \tag{4.3}$$

In the equations above L, μ, ρ, V and T are the uncertainties from the length of the rods, viscosity of the glycerine, density of the rod, velocity and temperature from the thermocouple, respectively. It is noted that the velocity uncertainty is explained at the end of Section 4.1. As an example by expanding the first partial differential term from Equation 4.2 it is shown that the maximum and minimum uncertainty are both considered (Equation 4.4).

$$\frac{\partial Re}{\partial L} = \frac{Re(L + \Delta L) - Re(L - \Delta L)}{2\Delta L} \tag{4.4}$$

For both the Reynolds number and drag coefficient, the errors associated with each term varied, thus having different influences on them, as shown in Figure 4.1. For the Reynolds number and drag coefficient, the velocity uncertainty contributed the most to the total error. The lowest error source was due to the length uncertainty for the Reynolds number and temperature uncertainty for the drag coefficient as shown in 4.1.

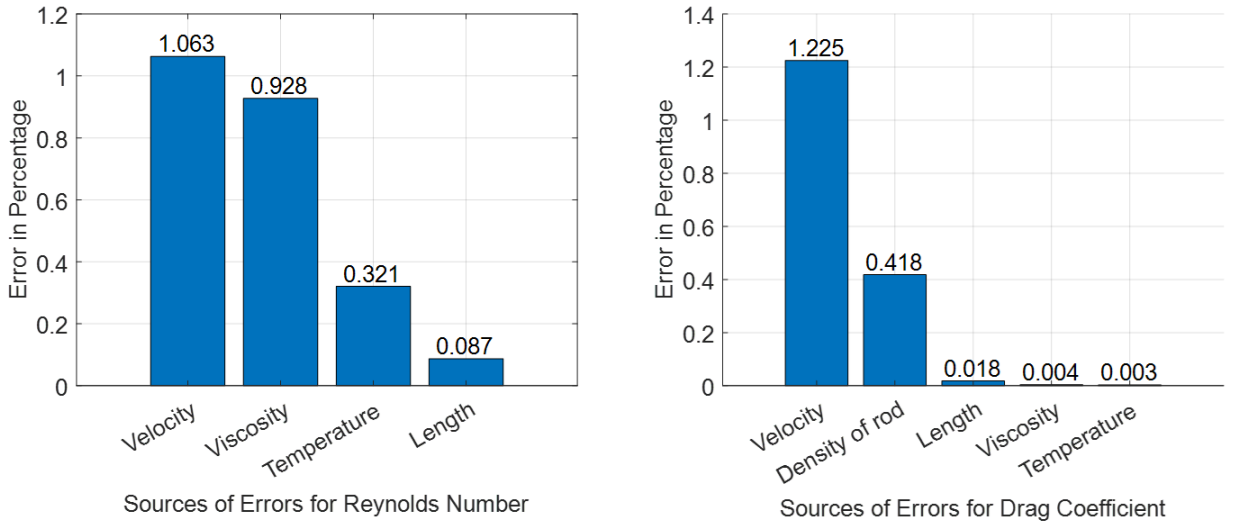

Figure 4.1: Sources of error from the uncertainties for viscosity, temperature, velocity, density of rod and manufactured length of rod (left Reynolds number and right the drag coefficient).

4.2 Straight Rod Analysis

4.2.1 Preferential Fall Orientation

It was observed in the experiments that straight rods have a preferential fall orientation within the studied range of Reynolds numbers. In the experiments, the three-dimensional trajectory of the cylindrical rods falling was measured. It is shown in Figure 4.2 that even a rod dropped from a vertical orientation will gradually transition from vertical to horizontal as time progresses. Regardless of their original orientation, the straight rods always obtain a horizontal orientation when they reach their settling velocity. This is consistent with Tran *et al.* [57] and Marchildon *et al.* [58] who showed that the particle always re-orients itself such that its maximum projected area is perpendicular to the direction of fall, thus maximizing stability. A rod falling at a low Reynolds number tends to orient itself in a position where small disturbances will cause minimal rotation. This happens because the orientation with the most drag will resist rotation the most. This behavior is observed in various organisms,

such as flying squirrels, that glide or fall and use this strategy to maintain stability during their descent discussed in Paskins *et al.* [81]. The Reynolds number range in both Tran *et al.* [57] and Marchildon *et al.* [58] encompasses the Reynolds number range in this thesis. As a result, when the cylindrical rod is dropped horizontally, it remains horizontal as shown previously in Figure 3.19. For the rods dropped in an initially vertical orientation, it takes a further distance to achieve a horizontal orientation for rods of greater diameter and length.

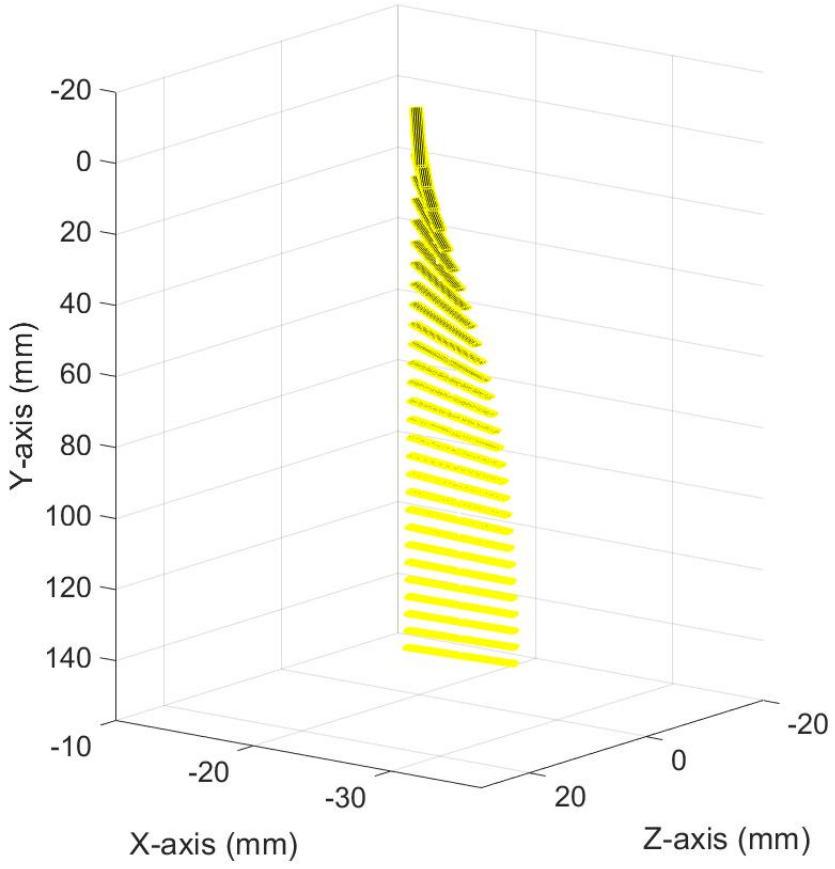

Figure 4.2: Three-dimensional trajectory of a 1.5 mm cylinder with aspect ratio 20 dropped vertically and reorientation to the horizontal.

For a straight cylindrical rod dropped vertically the projected area increases from the minimum value, given by the area of the end of the cylinder, to a maximum value before

asymptoting to a constant value, given by the product of the diameter and the length. An example of this behavior is shown in Figure 4.3, albeit in this case the rod was approaching the horizontal position as it entered the field of view of the cameras. Therefore, at 0 s the rod is not yet horizontal, but rather at an angle of 86.5 degrees. A projected area exceeding the product of the diameter and length is possible because the rod is finite and the ends contribute to the projected area when the rod is not horizontal. A small angle relative to the horizontal, the forces on either end of the rod would not be equal until the rod is horizontal and flow over the rod is symmetric, thus a torque would be generated until the horizontal position is reached. Therefore, a straight rod may take a projected area that is larger than the product of the diameter and length during its fall before reaching its settling velocity due to the effect of the two end cross sections.

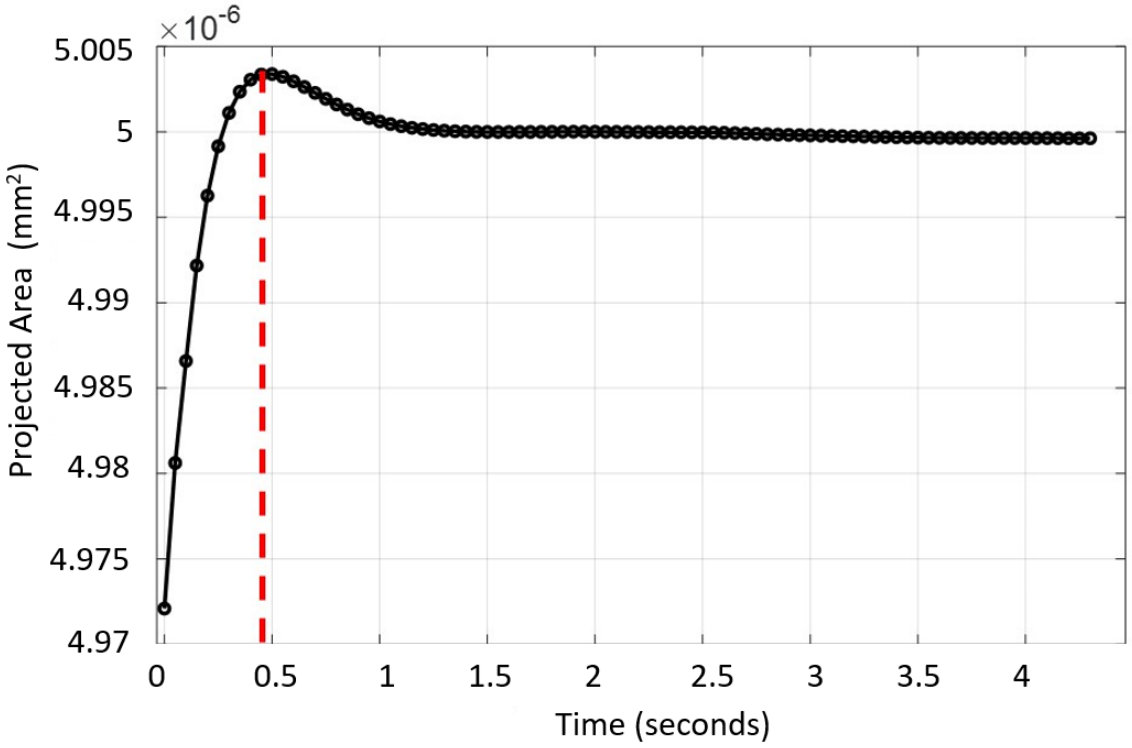

Figure 4.3: Variation of the projected area with time for a 0.5 mm rod and aspect ratio 20 dropped vertically where the red dashed line is drawn at the time when a maximum projected area was reached.

4.2.2 Effect of AR of Settling Velocity

A plot for the variation of velocity of the straight rods with diameter and aspect ratio is shown in Figure 4.4. The error bars are included in Figure 4.4 however are negligible compared to the value of the velocities. One conclusion from this figure is that the settling velocity increases as the diameter of the rod increases or as the aspect ratio increases. This figure also shows that as the aspect ratio increases, the rate of change in the rod's settling velocity decreases, and the settling velocity asymptotes. This is clearly demonstrated for diameters 0.5 mm and 1.0 mm. The physical interpretation for this fact is that as the rod increases in length, the effect of ends points of the rods become less important, therefore

the rod's settling velocity becomes independent of its length and consequently aspect ratio. Similarly, this concludes that for fibrous particles the settling velocity would also show an asymptotic behavior as aspect ratio increases. An obvious finding is that as the diameter of the particle increases the settling velocity increases. Looking at this from a force balance perspective the volume of the particle increase resulting in a larger mass and increase in gravitational force. Additionally, particles with larger diameters will fall faster as they have a low surface area to volume ratio.

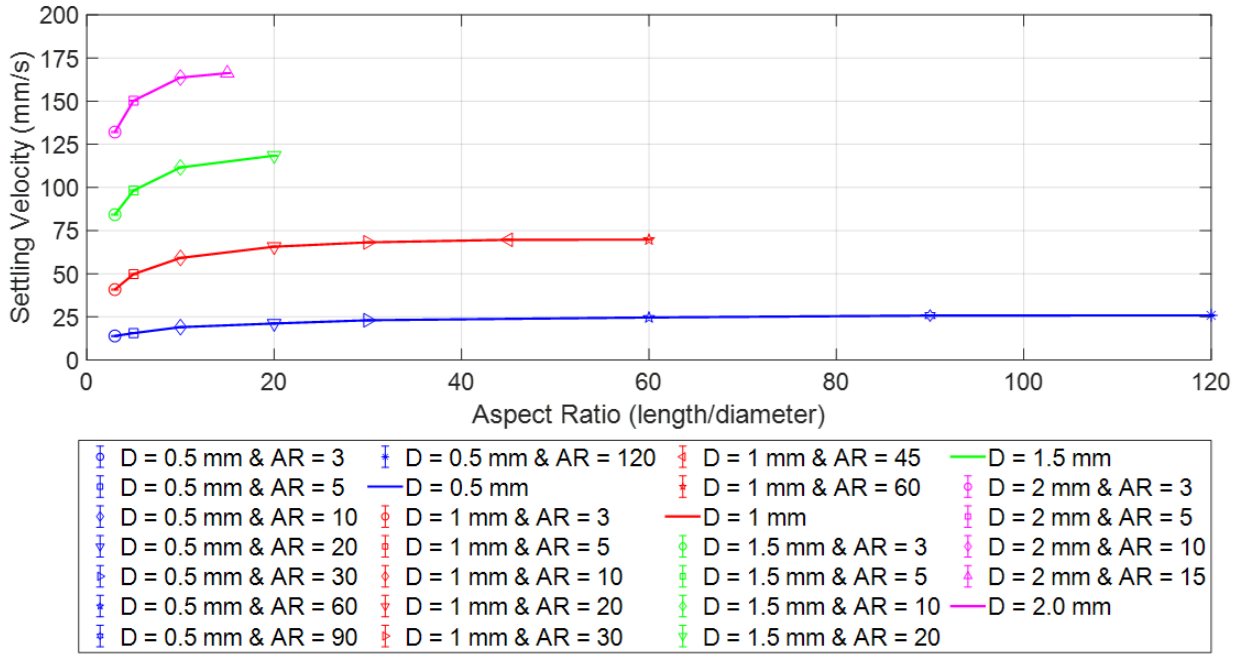

Figure 4.4: The settling velocity versus aspect ratio and diameter for straight rods falling in a glycerine water weight ratio of 90%.

4.2.3 C_D Variation with Reynolds Number

A graph showing the relationship between Reynolds number and drag coefficient for straight rods of various diameters and aspect ratios is shown in Figure 4.5. The Reynolds number and drag coefficient are calculated from 4.5 and 4.6, respectively.

$$Re = \frac{\rho u_s d}{\mu} \tag{4.5}$$

$$C_D = \frac{D}{\frac{1}{2}\rho u_s^2 A_p} \tag{4.6}$$

In Equations 4.5 and 4.6, ρ is the fluid density, u_s is the settling velocity, d is the diameter of the volume equivalent sphere, D is the drag force, A_P is the projected area. The drag force is calculated from the force balance governing the rod when it reaches the settling velocity. The projected area (A_P) for the drag coefficient is the surface area normal to the direction of the fall which is equal to the rod d, multiplied by the length L_P ($A_P = d \times L_P$). The characteristic length in the Reynolds number is modeled by the volume equivalent diameter (Equation 2.17). This figure shows that the drag coefficient decreases as the Reynolds number increases. This graph shows the deviation of the behavior of a cylindrical rod from a perfect sphere in the Stokes regime ($C_D = 24/Re$). From these results, the drag coefficient highly depends on other geometric factors such as sphericity or aspect ratio which distinguish them from a perfect sphere.

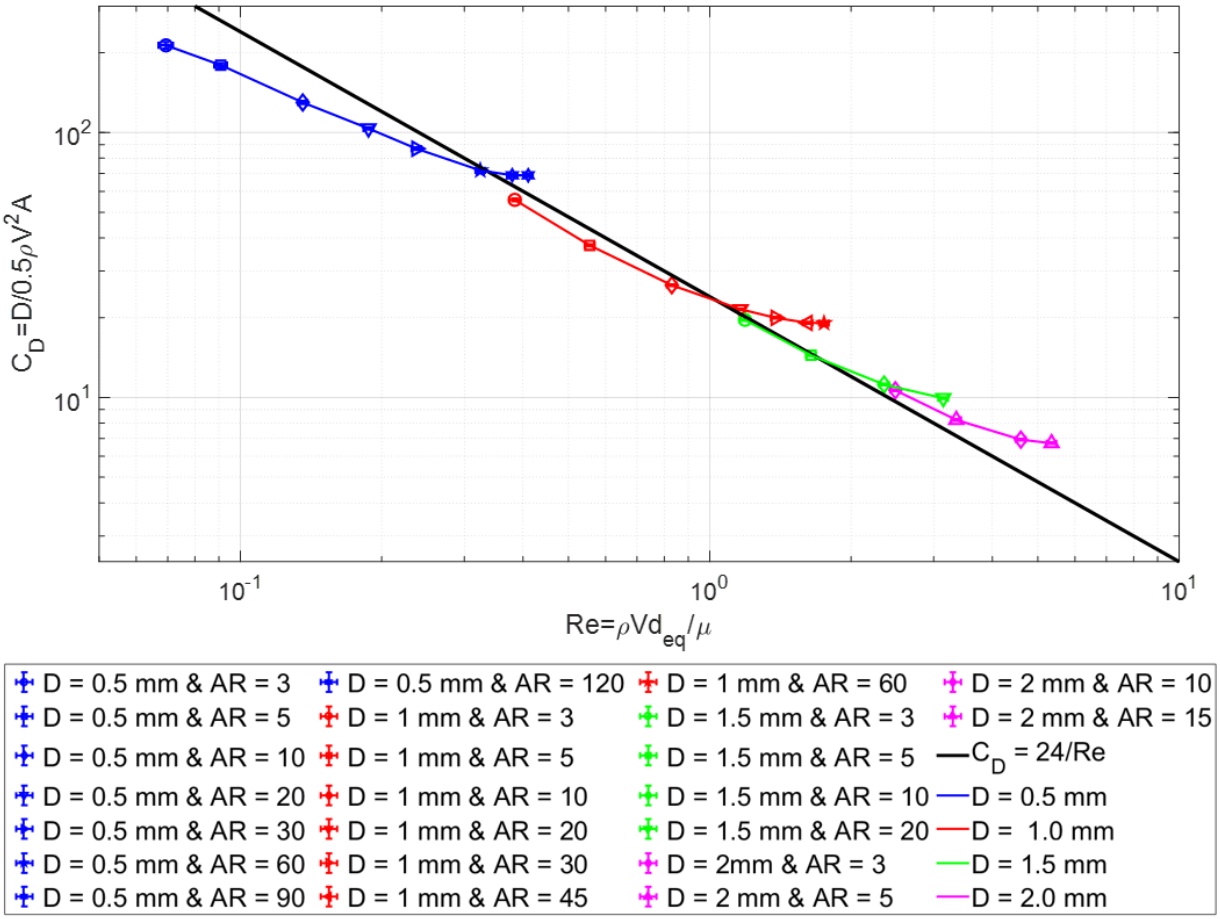

Figure 4.5: The drag coefficient versus Reynolds Number for straight rods of diameter 0.5, 1.0, 1.5 and 2.0 mm having aspect ratios from 3 to 120. A line of $C_D = 24/\mathrm{Re}$ is included for reference.

The experimental uncertainty has been detailed at the start of the chapter however the uncertainty hasn't been shown for the settling velocity, Reynolds number, and drag coefficient. Table 4.2 showcases the mean value, uncertainty, and error percentage for a straight rod of diameter 0.5 mm and aspect ratio 30. The mean value is found by taking the last ten velocity points of the trajectory and calculating the standard deviation to find the uncertainty.

Table 4.2: The mean value, uncertainty, and percentage error for a straight rod of diameter 0.5 mm and aspect ratio 30. The mean value is computed by taking the velocity from the last ten points of the 3D trajectory and calculating the standard deviation for the uncertainty.

D = 0.5 mm AR = 30	Mean Value	Uncertainty	Percentage Error (%)
Settling Velocity	23.03	0.32	1.39
Reynolds Number	0.24	0.01	2.33
Drag Coefficient	86.91	1.01	1.16

4.3 Curved Rods Analysis

4.3.1 Preferential Orientation of Curved Rods

Based on the observations as the curved rods fall they achieve a preferential orientation similar to the straight rods. Regardless of their initial orientation, the curved rods re-orient themselves such that the lowest point in their geometry points downwards. The three-dimensional trajectory is obtained using the profile of the curved rod and the coordinates of their centroids as shown in Figure 4.6.

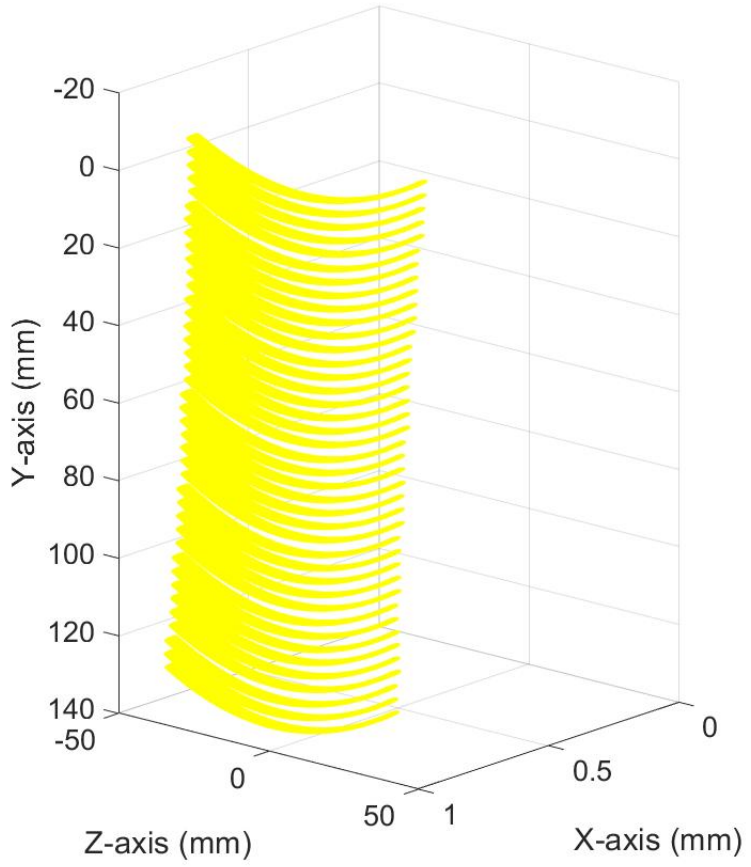

Figure 4.6: 3D Trajectory for a 0.5 mm diameter curved rod and aspect ratio 60.

4.3.2 Effect of Curvature of Rod on Settling Velocity

From microfibre samples collected through atmospheric deposition, often the fibres are not ideal straight geometries. One aspect noted is curvature. The settling behavior of the fibres can be affected by these irregularities in their shape. The purpose of this section is to study the effect of curvature in the geometry of a fibre on its settling velocity. While typical sampled fibres are more complex then just simple curves, the analysis provided is intended to improve the understanding of potential implications of changes in geometry relative to

straight rods on settling velocity. In this section, curved rods referenced in Table 3.4 were analyzed. Figure 4.7 shows the settling velocity of curved cylindrical rods in terms of the radius of curvature, aspect ratio, and diameter. It is shown that, the curved rods always reach higher velocities than the corresponding straight rods with the same diameter and aspect ratio. The settling velocity of the curved rods approach that of the straight rod with the same diameter and aspect ratio as the radius of curvature increases. The settling velocity of the straight rods is indicated with horizontal dashed lines. Moreover, as the radius of curvature increases, the settling velocity decreases. For curved rods, the settling velocity depends more on the diameter than the aspect ratio and radius of curvature within the ranges tested in this study.

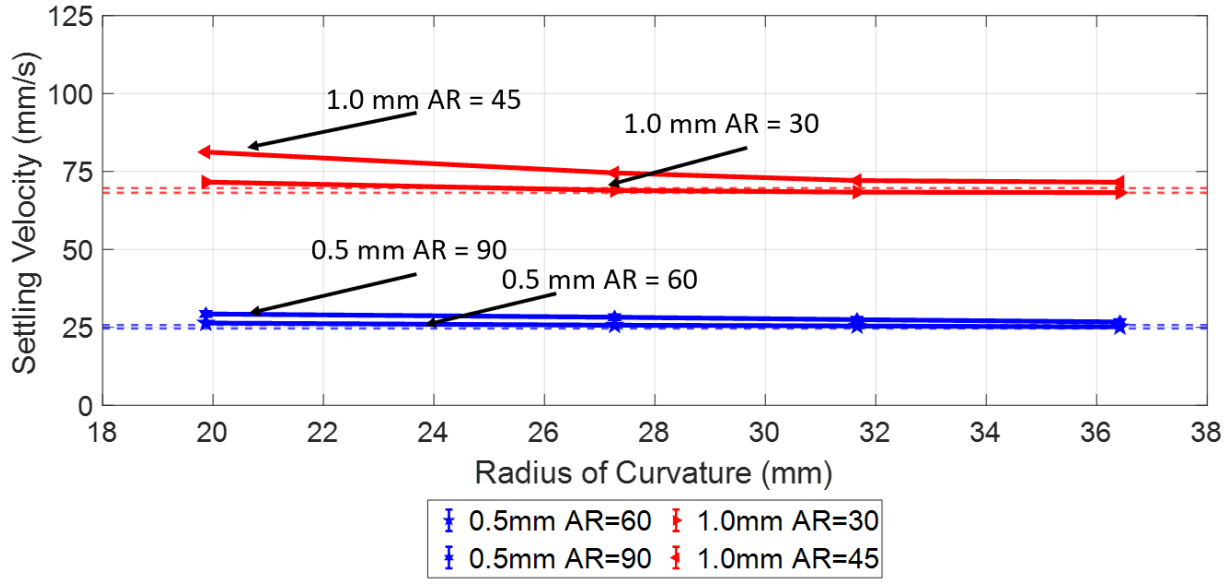

Figure 4.7: The settling velocity versus aspect ratio and diameter for curved rods falling in a glycerine water weight ratio of 90%, where the horizontal dashed line represents the settling velocity for a straight rod of the same diameter and aspect ratio.

Noteworthy is the fact that as the radius of curvature increases the difference between the settling velocities due to the aspect ratio decreases. This could be because as the radius of

curvature increases the shape of the rod becomes closer to the shape of a straight cylindrical rod which leads to a decrease in the effects of the rod's endpoints on the settling velocity. Additionally, our findings are consistent with Yang *et al.* [79] as a slender fibre increases in curvature the settling velocity increases. Therefore, it can be concluded that curved fibres have a higher settling velocity than perfectly straight fibres with the same diameter and aspect ratio, which is due to a smaller drag coefficient.

4.3.3 Effect of Reynolds Number on Drag Coefficient

In this section the variation of drag coefficient with Reynolds number and geometric properties including diameter, aspect ratio, and radius of curvature is plotted for the curved rods. Due to the existence of curvature in their geometry, curved rods' behavior is different from straight rods in terms of the aerodynamic forces applied to them. It can be concluded from this plot that the drag coefficient of the curved rod is smaller than that of the straight rod with the same diameter and aspect ratio which is consistent with the results of Yang *et al.* [79] research. Moreover, as the radius of curvature decrease, the projected area decreases while the velocity increases based on Figure 4.8. As the effect of change in velocity dominates the projected area, the drag coefficient decrease with a decrease in the radius of curvature based on Equation 4.6. Figure 4.8 shows a comparison of the straight and curved rod experimental data for Figures 4.5 and 4.8 and compares them to the models from Song *et al.* [17] and Bagheri *et al.* [56]. It is shown that the present experimental data lies below the predicted results from the existing models.

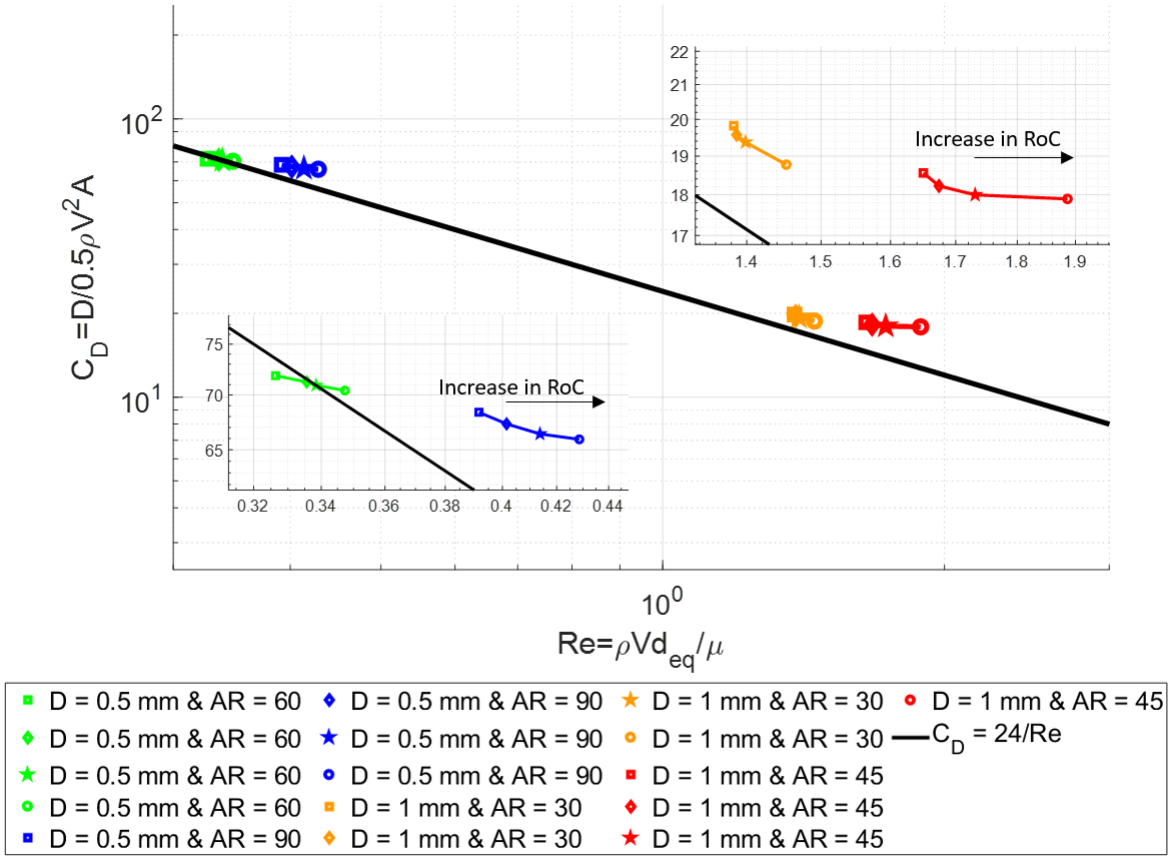

Figure 4.8: The drag coefficient versus Reynolds number for curved rods, where the symbols represent the curvature of the rods. The squares RoC is 37.5 mm, diamonds RoC is 31.7 mm, stars RoC is 27.3 mm, and circles RoC is 19.9 mm.

Figure 4.9 compares the experimental data for drag coefficient and Reynolds number for straight rods with the results of the research work from Huner *et al.* [64], Tritton *et al.* [63], and Khalili *et al.* [65]. The characteristic length used in the Reynolds number is the diameter of the cylinder. In order to determine the drag coefficient for a two-dimensional cylinder with high aspect ratios, the drag force (D) is calculated per unit length of the cylinder and is based on the projected area (A) per unit length of the cylinder, which is equivalent to the diameter. This comparison shows for large cylinders (higher aspect ratios) the experimental results are close in value to Huner *et al.* [64], Tritton *et al.* [63] and Khalili *et al.* [65] which are associated with 2D circular cylinders.

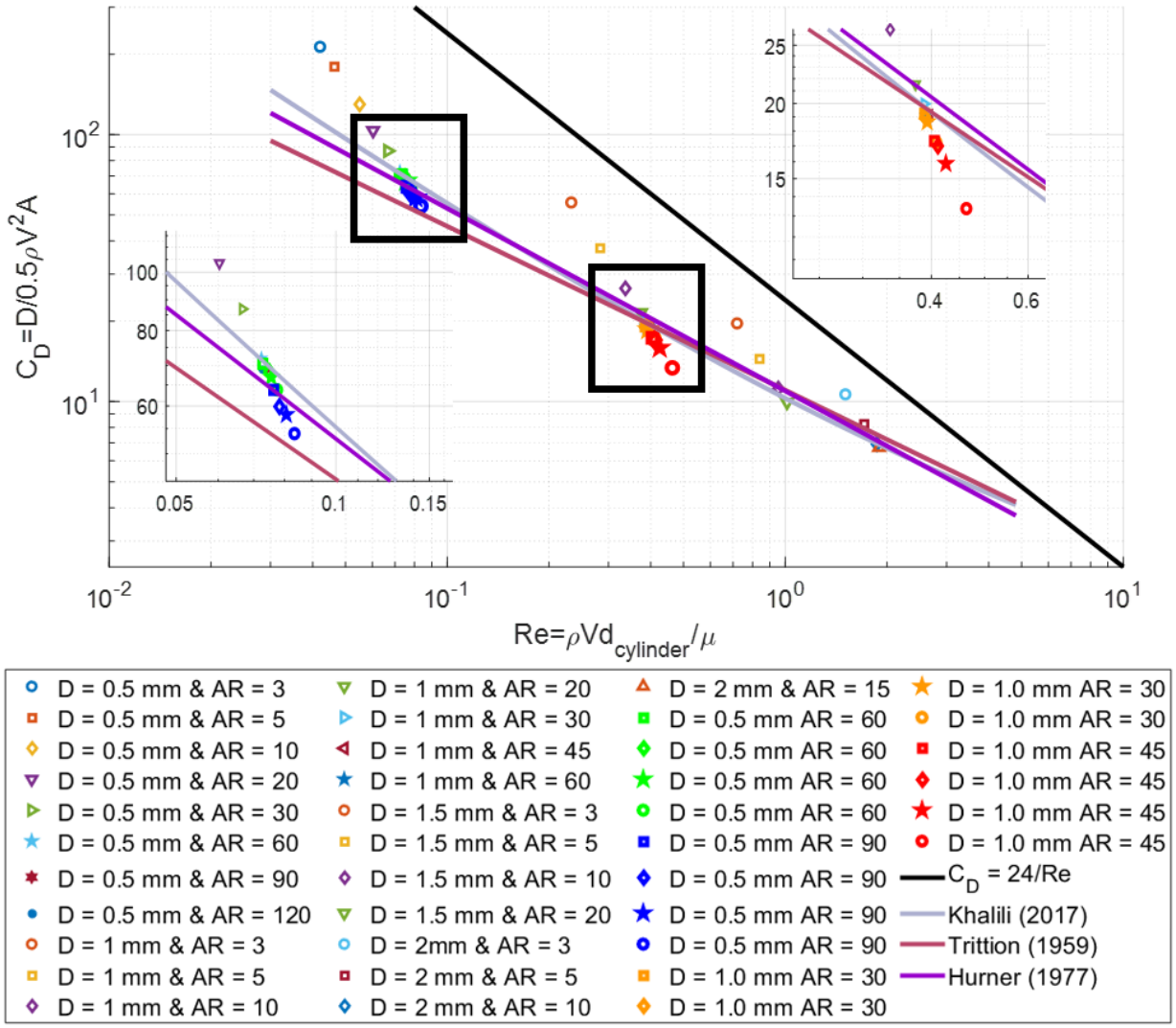

Figure 4.9: Comparison of the present experimental research work with existing models from Huner *et al.* [64], Tritton *et al.* [63], and Khalili *et al.* [65]. The squares RoC is 37.5 mm, diamonds RoC is 31.7 mm, stars RoC is 27.3 mm, and circles RoC is 19.9 mm for the lime green, navy blue, orange and red point.

However, the drag experienced by smaller cylinders was found to be greater than what existing models had predicted, similar to Huner *et al.* [64]. The Khalili *et al.* [65] is valid for relatively low Reynolds numbers (less than 1). The results obtained from the Khalili *et al.*

[65] study were found to be in close agreement with our own results for high aspect ratio cylinders. Tritton *et al.* [63] model is also applicable to high aspect ratio cylinders (above 600) as shown in Figure 4.9. Another point which is observed in Figure 4.9 is as the aspect ratio of the cylinder increases the drag coefficient becomes more consistent in all the models.

Figure 4.10 compares the straight and curved rod experimental data for Figures 4.3 and 4.7 and compares them to the models from Song *et al.* [17] and Bagheri *et al.* [56]. It is shown that the present experimental data lies below the predicted results from the existing models. Figures 4.9 and 4.10 cannot be compared on the same graph as Song *et al.* [17] and Bagheri *et al.* [56] uses equivalent diameter in the Reynolds Number.

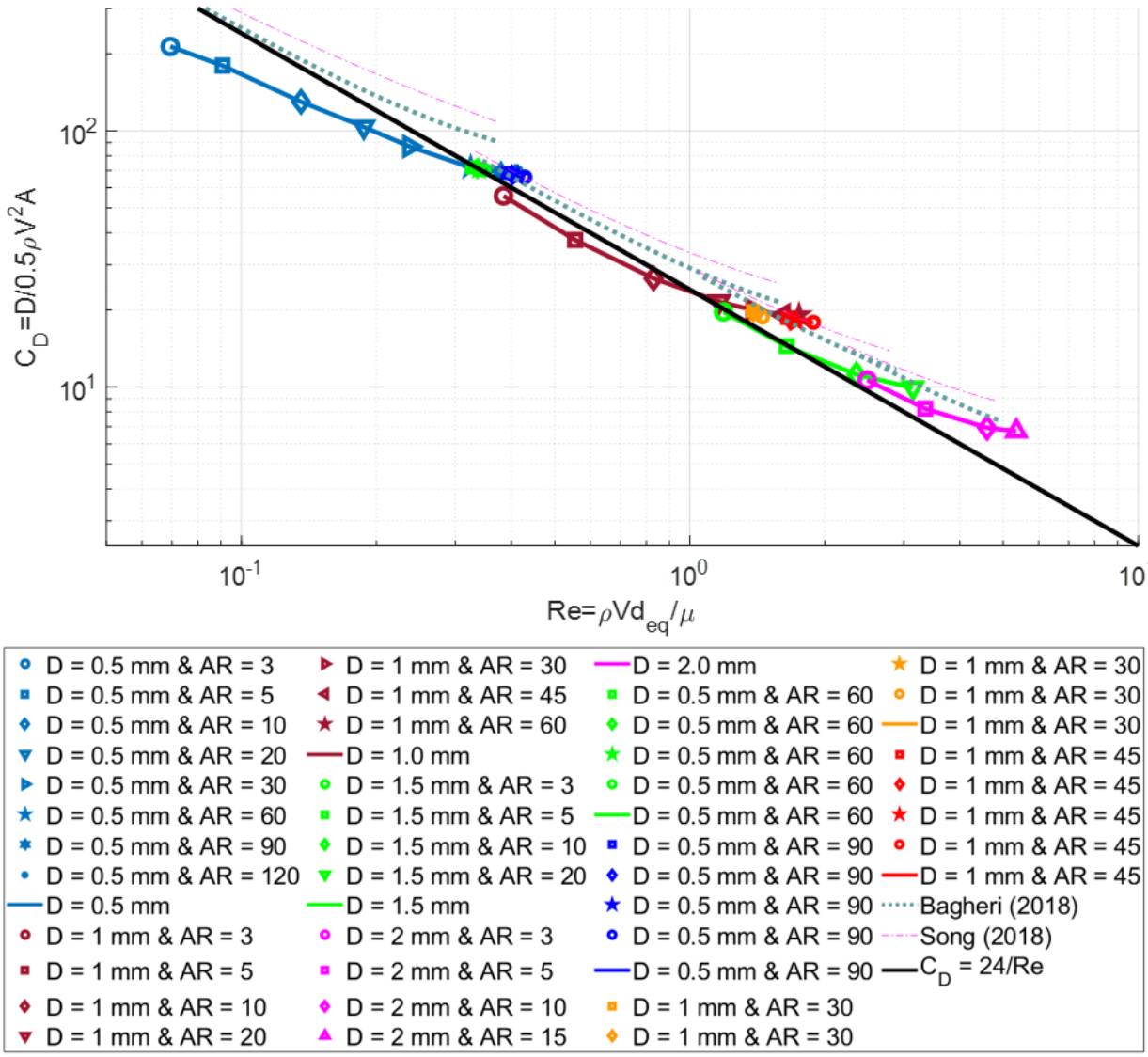

Figure 4.10: Comparison of the present experimental research work with existing models from Bagheri *et al.* [56] and Song *et al.* [17]. The squares RoC is 37.5 mm, diamonds RoC is 31.7 mm, stars RoC is 27.3 mm, and circles RoC is 19.9 mm for the lime green, navy blue, orange and red point.

4.4 Prediction of Microfibres Settling Velocity

Based on the experimental results a model has been developed to predict the settling velocity of microfibres found through atmospheric depositions. A generally relationship shown in Equation 4.7 shows a relationship between the drag coefficient and the particles Reynolds number developed by Song *et al.* [17]. The coefficients a, b, c and d represent coefficients used to fit the experimental data obtained from Song *et al.* [17] while ϕ is the particles sphericity and the effect of settling orientation is represented by S.

$$C_{dn} = \frac{24}{Re_n(\phi^c S^d)} \left(1 + aRe_n\right)^b \tag{4.7}$$

Similarly, a modified relationship is used to model the experimental data in the present work for both straight and curve rods in Equation 4.8.

$$C_D = \frac{24}{Re_n(AR^c \phi^d AR_n^e)} \left(1 + aRe_n\right)^b \tag{4.8}$$

The difference between Equation 4.7 and Equation 4.8 is the removal of the S term and introducing AR which is the aspect ratio of a particle and AR_n which is the projected length *(L_p)* of the particle divided by the length as shown in Equation 4.9. The Reynold number used the volume equivalent diameter noted in Equation 2.17.

$$AR_n = \frac{L_p}{L} \tag{4.9}$$

The calculated value for the AR_n for a straight rod will always be unity thus Equation 4.8 is valid for both curved and straight rods. The coefficients for values a, b, c, d and e in Equation 4.8 are shown in Table 4.3

Table 4.3: Calculated coefficients for Equation 4.8 to fit the experimental data.

a	b	c	d	e
0.37	0.71	1.58	5.82	-0.42

Table 4.4 utilizes Equation 4.8 to compare the results from the experiment with the theoretical equation. The average percentage error calculated for the total experimental results is 6.8%.

Table 4.4: Comparison of experimental results with Equation 4.8 for the cylindrical rods dropped in the experiment for diameters 0.5 mm to 1.5 mm.

Particle Size	Reynolds Number	Exp. C_D	Theo. C_D	% Error
D = 0.5 AR = 3	0.09	179.67	175.07	2.56
D = 0.5 AR = 10	0.14	129.88	116.10	10.61
D = 0.5 AR = 20	0.19	103.58	95.18	8.11
D = 0.5 AR = 30	0.24	86.91	84.10	3.24
D = 0.5 AR = 60	0.32	71.96	76.92	6.90
D = 0.5 AR = 90	0.38	68.98	75.93	10.07
D = 1.0 AR = 3	0.38	55.72	52.02	6.64
D = 1.0 AR = 5	0.56	37.50	31.97	14.76
D = 1.0 AR = 10	0.83	26.54	22.21	16.34
D = 1.0 AR = 20	1.16	21.53	18.88	12.92
D = 1.0 AR = 30	1.38	19.98	18.25	8.65
D = 1.0 AR = 45	1.62	19.12	18.21	4.78
D = 1.0 AR = 60	1.75	19.08	18.76	1.67
D = 1.5 AR = 3	1.19	19.64	19.83	1.01
D = 1.5 AR = 5	1.64	14.44	13.26	8.15
D = 1.5 AR = 10	2.35	11.19	10.12	9.61
D = 1.5 AR = 20	3.14	9.94	9.37	5.68

Table 4.5, 4.6 and 4.7 shows, as the aspect ratio of the fibre increases the settling velocity result obtained from the present experimental model becomes close to Khalili *et al.* [65] value. This makes sense because Khalili *et al.* [65] model considers a two-dimensional cylinder of infinite length. Additionally, as the aspect ratio of a fibre decreases the settling velocity is close to Song *et al.* [17] and Bagheri *et al.* [56] model as the equations developed in their models utilized a range of geometries. Figure 4.11 depicts the terminal velocity, Reynolds number, and drag coefficient of a straight polyacrylonitrile fibrous particle with a diameter of 20 μm and an AR of 20 (orange line) compared to a range of radius of curvature (blue line). The results were obtained using Equation 4.8 for both straight and curved rods. The way the calculations were made for straight rods is to set the term AR_n in Equation 4.8 to 1.

Table 4.5: Comparison of data for calculating the settling velocity, Reynolds Number and Drag Coefficient of a polyacrylonitrile fibrous particle of AR 20 and diameter 20 μm.

Model	Settling Velocity (mm/s)	Reynolds Number	Drag Coefficient
Khalili *et al.* [65]	73.28	0.05	56.61
Song *et al.* [17]	23.57	0.10	547.43
Bagheri *et al.* [56]	28.41	0.12	376.58
Henn *et al.* [14]	56.50	0.23	95.17
Present Model	69.04	0.28	63.77

Table 4.6: Comparison of data for calculating the settling velocity, Reynolds Number and Drag Coefficient of a polyacrylonitrile fibrous particle of AR 5 and diameter 20 μm.

Model	Settling Velocity (mm/s)	Reynolds Number	Drag Coefficient
Khalili *et al.* [65]	73.28	0.05	56.61
Song *et al.* [17]	22.13	0.06	621.95
Bagheri *et al.* [56]	27.30	0.07	407.9
Henn *et al.* [14]	36.16	0.94	232.37
Present Model	49.36	0.13	124.80

Table 4.7: Comparison of data for calculating the settling velocity, Reynolds Number, and Drag Coefficient of a polyacrylonitrile fibrous particle of AR 40 and diameter 20 μm.

Model	Settling Velocity (mm/s)	Reynolds Number	Drag Coefficient
Khalili *et al.* [65]	73.28	0.05	56.61
Song *et al.* [17]	22.93	0.12	530.74
Bagheri *et al.* [56]	27.42	0.14	404.3
Henn *et al.* [14]	66.54	0.34	68.59
Present Model	71.36	0.37	59.7

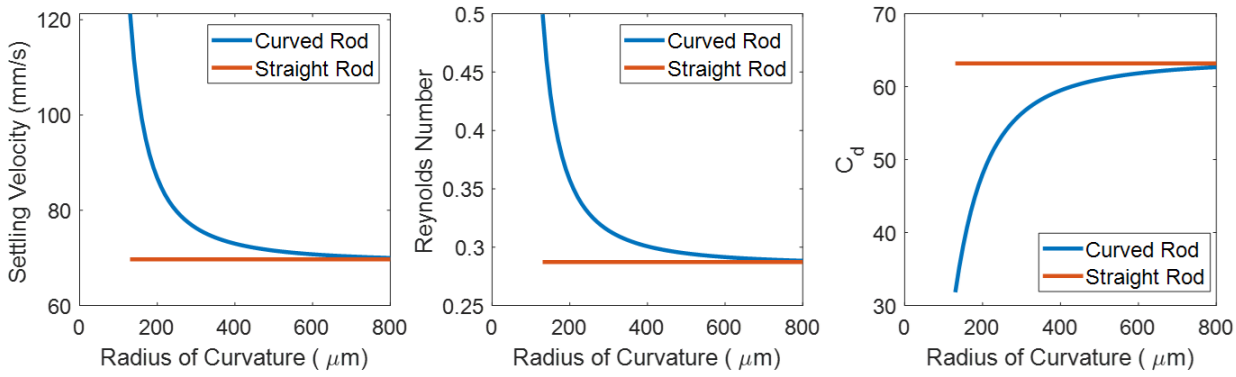

Figure 4.11: Calculation of the Settling velocity (mm/s), Reynolds number and Drag coefficient for a polyacrylonitrile fibrous particle of diameter 20 μm and AR 20 (i.e. straight length = 400 μm) using the present model for a range of Radius of Curvatures.

As mentioned, Wright *et al.* [9] found the settling velocity for a cylindrical fibrous particle (polyacrylonitrile) of aspect ratio (length/diameter) of (400 μm/20 μm). Wright *et al.* [9] assumed a horizontal wind speed of 5 m/s that the fibrous particle traveled along and started from a height 720 meters above the ground. Using various experimental models, the data from Table 4.8 summarizes the settling velocity and total distance and time traveled in the horizontal direction. Comparing the distances traveled from the model of Henn *et al.* [14] to the present model is 7.86 kilometers travel difference. The variation of the horizontal travel distance between Henn *et al.* [14] to Song *et al.* [17] and [56] are 66.71 and 92.74 kilometers, respectively while Khalili *et al.* [65] horizontal travel is 10.87 kilometers shorter. Assuming that the exact same fiber has a radius of curvature of 400 mm, the presented model incorporates this parameter to calculate the settling velocity. With a settling velocity of 73.00 mm/s, the fiber would travel a horizontal distance of 49.3 km in 9863 seconds. Therefore, considering the curvature of the fibre, the horizontal travel distance compared to Henn *et al.* [14] model is 10.7 kilometers with the present model. This shows that the a curved fibre traveled 2.84 km less than a straight fibre with the same aspect ratio.

Table 4.8: Comparison of data total time and horizontal distance traveled for polyacrylonitrile fibrous particle of AR 20 and diameter 20 μm from an initial height of 720 m above the ground with a horizontal wind speed of 5 m/s. Wright *et al.* [9] used the Henn *et al.* [14] model, where he reported the settling velocity of this particle to be 60 mm/s.

Model	Settling Velocity (mm/s)	Total Time (s)	Horizontal Travel (km)
Khalili *et al.* [65]	73.28	9825	49.13
Song *et al.* [17]	23.57	30547	152.74
Bagheri *et al.* [56]	28.41	25343	126.71
Henn *et al.* [14]	60	12000	60
Present Model	69.04	10428	52.14

Chapter 5

Summary and Conclusions

5.1 Conclusions

Microplastic fibres are a subset of plastic pollution that has been found across the globe from urban to remote regions. Samples of microfibres collected around the world demonstrate that these fibres have a geometry more complex than a simple straight length of the fibre. However, current attempts to simulate the atmospheric transport of fibres tend to rely on simple aerodynamic models based on straight fibre lengths. Therefore, while current simulations provide valuable insight into the potential long-range transport of these pollutants by the wind, they may not accurately predict their range of atmospheric transport. One common shape characteristic of microfibres is the curvature of their geometry. While typically sampled fibres are more complex than just simple curves, the focus of this thesis is intended to improve the understanding of changes in geometry relative to idealized straight fibres on settling velocity and hence atmospheric transport predictions.

An important first step was the design, manufacture and validation of a drop tank and system using a particle tracking velocimetry technique to measure the trajectory and velocity of straight and curved rods in free fall. The experiment performed uses a particle tracking velocimetry (PTV) technique to record the motion of straight cylindrical rods falling through

glycerin and water mixtures $GW_{90\%}$. The sizing of these rods have diameters between 0.5 to 2 mm with aspect ratios of 3 to 120 to replicate the Reynolds number regime (0.1 to 10). These non-dimensional relations are the basis for models of the spectrum of complex fibre geometries typical of the atmospheric deposition samples that we aim to simulate the transport of.

The results show that as a rod's diameter and aspect ratio increases the settling velocity increases. Moreover for straight rods as the aspect ratio of a rod increases the settling velocity asymptotes to a constant value, implying the negligible effects of the endpoints on velocity for long rods. The variation of the drag coefficient with the Reynolds number demonstrates that the behaviour of straight rods differs from that of a perfect sphere because shape factors have a large influence on the drag coefficient. The straight rods are observed to take a horizontal orientation when they reach their settling velocity. The shorter the rods, the faster they will achieve their settling velocity and orientation.

Our observations show that the settling velocity of the curved rods is always larger than that of the straight rods with the same diameter and aspect ratio. The smaller the radius of curvature, the faster the settling velocity. In very large aspect ratios, the settling velocity does not change significantly with an increase in aspect ratio, similar to the straight rods. As the radius of curvature decreases, the velocity increases and the projected area decreases. Due to the dominance of velocity over the projected area, the drag coefficient decreases with a decrease in the radius of curvature for a rod with a specific diameter and length. The experimental results for high aspect ratio rods in the present research align with existing models for high aspect ratio or two-dimensional cylinders.

A new experimental model has been developed that considers the curvature of rods. This model employs a single equation to estimate the settling velocity, drag coefficient, and terminal velocity for both straight and curved rods. Based on a situation from Wright *et al.* [9] it was compared with existing models in the literature for a cylindrical particle (polyacrylonitrile) of aspect ratio (length/diameter) of (400 μm/20 μm).

5.2 Future Work

The present study has contributed important insights into the settling behaviour of straight and curved rods at low Reynolds numbers in a quiescent fluid. However, there are several limitations to the study that need to be acknowledged. Firstly, the absence of turbulence as an experimental parameter means that the results may not be applicable to fluid systems that are subject to turbulent flows. It is therefore important to conduct further research to investigate the effect of turbulence on the settling behaviour of rods and other microfibers.

Furthermore, the data collected in this study is limited to the settling velocity of only straight and curved rods, and does not consider other geometrical shapes such as bends or other abnormal shapes. This is a significant limitation, as microfibers collected from atmospheric deposition are often found in a variety of complex geometries such as loops, kinks, and tangles. It is important to understand how the settling behaviour of these different geometries may differ from straight and curved rods, as this can have important implications for the transport and fate of microfibers in the environment.

Another important consideration is that very high aspect ratio fibers, such as those found in some types of microfibers, may not be rigid and their geometry can be altered by fluid forces. This can have important implications for their settling behaviour, as the flexibility and deformability of these fibers can influence their transport and deposition in the environment.

In conclusion, while the present study has provided valuable insights into the settling behaviour of straight and curved rods at low Reynolds numbers in a quiescent fluid, there is still much to be learned about the settling behaviour of microfibers in more complex fluid systems and with a wider range of geometries. Further research is needed to address these limitations and to develop a more comprehensive understanding of the transport and fate of microfibers in the environment.

References

[1] Steve Allen, Deonie Allen, Samaneh Karbalaei, Vittorio Maselli, and Tony R Walker. Micro (nano) plastics sources, fate, and effects: What we know after ten years of research. *Journal of Hazardous Materials Advances*, 6:100057, 2022.

[2] S Allen, D Allen, F Baladima, VR Phoenix, JL Thomas, G Le Roux, and JE Sonke. Evidence of free tropospheric and long-range transport of microplastic at pic du midi observatory. *Nature communications*, 12(1):7242, 2021.

[3] Janice Brahney, Natalie Mahowald, Marje Prank, Gavin Cornwell, Zbigniew Klimont, Hitoshi Matsui, and Kimberly Ann Prather. Constraining the atmospheric limb of the plastic cycle. *Proceedings of the National Academy of Sciences*, 118(16):e2020719118, 2021.

[4] Alice A Horton, Alexander Walton, David J Spurgeon, Elma Lahive, and Claus Svendsen. Microplastics in freshwater and terrestrial environments: evaluating the current understanding to identify the knowledge gaps and future research priorities. *Science of the total environment*, 586:127–141, 2017.

[5] Rachid Dris, Johnny Gasperi, Mohamed Saad, Cécile Mirande, and Bruno Tassin. Synthetic fibers in atmospheric fallout: a source of microplastics in the environment? *Marine pollution bulletin*, 104(1-2):290–293, 2016.

[6] Steve Allen, Deonie Allen, Vernon R Phoenix, Gaël Le Roux, Pilar Durántez Jiménez, Anaëlle Simonneau, Stéphane Binet, and Didier Galop. Atmospheric transport and deposition of microplastics in a remote mountain catchment. *Nature Geoscience*, 12(5): 339–344, 2019.

[7] Melanie Bergmann, Sophia Mützel, Sebastian Primpke, Mine B Tekman, Jürg Trachsel, and Gunnar Gerdts. White and wonderful? Microplastics prevail in snow from the alps to the arctic. *Science advances*, 5(8):eaax1157, 2019.

[8] Sajjad Abbasi, Behnam Keshavarzi, Farid Moore, Andrew Turner, Frank J Kelly, Ana Oliete Dominguez, and Neemat Jaafarzadeh. Distribution and potential health impacts of microplastics and microrubbers in air and street dusts from asaluyeh county, iran. *Environmental pollution*, 244:153–164, 2019.

[9] Stephanie Louise Wright, Jannis Ulke, A Font, Ka Lung Andrew Chan, and Frank James Kelly. Atmospheric microplastic deposition in an urban environment and an evaluation of transport. *Environment international*, 136:105411, 2020.

[10] Janice Brahney, Margaret Hallerud, Eric Heim, Maura Hahnenberger, and Suja Sukumaran. Plastic rain in protected areas of the united states. *Science*, 368(6496):1257–1260, 2020.

[11] Nikolaos Evangeliou, Henrik Grythe, Zbigniew Klimont, Chris Heyes, Sabine Eckhardt, Susana Lopez-Aparicio, and Andreas Stohl. Atmospheric transport is a major pathway of microplastics to remote regions. *Nature communications*, 11(1):1–11, 2020.

[12] Minghu Liu, Zhiming Xin, Zhi Su, Yingming Zhao, Xinle Li, Zhimin Liu, Mariano A Cony, Wei Liang, Xuanping Qin, Jianqiang Qian, et al. A video camera recording method for measuring terminal velocity of seed dispersal by wind. *Journal of Forestry Research*, 32(1):81–90, 2021.

[13] Kai Liu, Tianning Wu, Xiaohui Wang, Zhangyu Song, Changxing Zong, Nian Wei, and Daoji Li. Consistent transport of terrestrial microplastics to the ocean through atmosphere. *Environmental science & technology*, 53(18):10612–10619, 2019.

[14] Arthur R Henn. Calculation of the stokes and aerodynamic equivalent diameters of a short reinforcing fiber. *Particle & particle systems characterization*, 13(4):249–253, 1996.

[15] Yulan Zhang, Shichang Kang, Steve Allen, Deonie Allen, Tanguang Gao, and Mika Sillanpää. Atmospheric microplastics: A review on current status and perspectives. *Earth-Science Reviews*, 203:103118, 2020.

[16] Joanna E Bullard, Annie Ockelford, Patrick O'Brien, and Cheryl McKenna Neuman. Preferential transport of microplastics by wind. *Atmospheric Environment*, 245:118038, 2021.

[17] Xianzhi Song, Zhengming Xu, Gensheng Li, Zhaoyu Pang, and Zhaopeng Zhu. A new model for predicting drag coefficient and settling velocity of spherical and non-spherical particle in newtonian fluid. *Powder Technology*, 321:242–250, 2017.

[18] Reza Barati, Seyed Ali Akbar Salehi Neyshabouri, and Goodarz Ahmadi. Development of empirical models with high accuracy for estimation of drag coefficient of flow around a smooth sphere: An evolutionary approach. *Powder Technology*, 257:11–19, 2014.

[19] R Clift and WH Gauvin. Motion of entrained particles in gas streams. *The Canadian Journal of Chemical Engineering*, 49(4):439–448, 1971.

[20] Jinping Peng, Jundong Wang, and Liqi Cai. Current understanding of microplastics in the environment: occurrence, fate, risks, and what we should do. *Integrated environmental assessment and management*, 13(3):476–482, 2017.

[21] Nanna B Hartmann, Thorsten Huffer, Richard C Thompson, Martin Hassellov, Anja Verschoor, Anders E Daugaard, Sinja Rist, Therese Karlsson, Nicole Brennholt, Matthew Cole, et al. Are we speaking the same language? Recommendations for a definition and categorization framework for plastic debris. 2019.

[22] Courtney Arthur, Joel E Baker, and Holly A Bamford. Proceedings of the international research workshop on the occurrence, effects, and fate of microplastic marine debris, september 9-11, 2008, university of washington tacoma, tacoma, wa, usa. 2009.

[23] Marcel Paredes, Rafaela Viteri, Tito Castillo, Cristian Caminos, and Christian Ebere Enyoh. Microplastics from degradation of tires in sewer networks of the city of riobamba, ecuador. *Environmental Engineering Research*, 26(5), 2020.

[24] Matthew Cole, Pennie Lindeque, Claudia Halsband, and Tamara S Galloway. Microplastics as contaminants in the marine environment: a review. *Marine pollution bulletin*, 62 (12):2588–2597, 2011.

[25] Mark Anthony Browne, Phillip Crump, Stewart J Niven, Emma Teuten, Andrew Tonkin, Tamara Galloway, and Richard Thompson. Accumulation of microplastic on shorelines woldwide: sources and sinks. *Environmental science & technology*, 45(21):9175–9179, 2011.

[26] François Remy, France Collard, Bernard Gilbert, Philippe Compère, Gauthier Eppe, and Gilles Lepoint. When microplastic is not plastic: the ingestion of artificial cellulose fibers by macrofauna living in seagrass macrophytodetritus. *Environmental science & technology*, 49(18):11158–11166, 2015.

[27] Aikaterini Anastasopoulou, Chryssi Mytilineou, Christopher J Smith, and Konstantia N Papadopoulou. Plastic debris ingested by deep-water fish of the ionian sea (eastern

mediterranean). *Deep Sea Research Part I: Oceanographic Research Papers*, 74:11–13, 2013.

[28] Erik R Zettler, Tracy J Mincer, and Linda A Amaral-Zettler. Life in the "plastisphere": microbial communities on plastic marine debris. *Environmental science & technology*, 47 (13):7137–7146, 2013.

[29] Alzona, BL Cohen, Hea Rudolph, HN Jow, and JO Frohliger. Indoor-outdoor relationships for airborne particulate matter of outdoor origin. *Atmospheric Environment (1967)*, 13(1):55–60, 1979.

[30] John L Pauly, Sharon J Stegmeier, Heather A Allaart, Richard T Cheney, Paul J Zhang, Andrew G Mayer, and Richard J Streck. Inhaled cellulosic and plastic fibers found in human lung tissue. *Cancer Epidemiology and Prevention Biomarkers*, 7(5):419–428, 1998.

[31] Qiqing Chen, Yue Li, and Bowen Li. Is color a matter of concern during microplastic exposure to scenedesmus obliquus and daphnia magna? *Journal of hazardous materials*, 383:121224, 2020.

[32] Rachid Dris, Johnny Gasperi, Vincent Rocher, Mohamed Saad, Nicolas Renault, and Bruno Tassin. Microplastic contamination in an urban area: a case study in greater paris. *Environmental Chemistry*, 12(5):592–599, 2015.

[33] Peter S Liss. Microplastics: All up in the air? In *EGU General Assembly Conference Abstracts*, page 9684, 2020.

[34] Lei Su, Xiong Xiong, Yulan Zhang, Chenxi Wu, Xiangrong Xu, Chengjun Sun, and Huahong Shi. Global transportation of plastics and microplastics: A critical review of pathways and influences. *Science of The Total Environment*, page 154884, 2022.

[35] Michèlle Van Der Does, Peter Knippertz, Philipp Zschenderlein, R Giles Harrison, and Jan-Berend W Stuut. The mysterious long-range transport of giant mineral dust particles. *Science advances*, 4(12):eaau2768, 2018.

[36] Denis-Didier Rousseau, Danielle Duzer, Jean-Louis Etienne, Geneviève Cambon, Dominique Jolly, Jackie Ferrier, and Patrick Schevin. Pollen record of rapidly changing air trajectories to the north pole. *Journal of Geophysical Research: Atmospheres*, 109(D6), 2004.

[37] Liqi Cai, Jundong Wang, Jinping Peng, Zhi Tan, Zhiwei Zhan, Xiangling Tan, and Qiuqiang Chen. Characteristic of microplastics in the atmospheric fallout from dongguan city, china: preliminary research and first evidence. *Environmental Science and Pollution Research*, 24(32):24928–24935, 2017.

[38] Qian Zhou, Haibo Zhang, Chuancheng Fu, Yang Zhou, Zhenfei Dai, Yuan Li, Chen Tu, and Yongming Luo. The distribution and morphology of microplastics in coastal soils adjacent to the bohai sea and the yellow sea. *Geoderma*, 322:201–208, 2018.

[39] Malin Klein and Elke K Fischer. Microplastic abundance in atmospheric deposition within the metropolitan area of hamburg, germany. *Science of the Total Environment*, 685:96–103, 2019.

[40] Rachid Dris, Johnny Gasperi, Cécile Mirande, Corinne Mandin, Mohamed Guerrouache, Valérie Langlois, and Bruno Tassin. A first overview of textile fibers, including microplastics, in indoor and outdoor environments. *Environmental pollution*, 221:453–458, 2017.

[41] Sharareh Dehghani, Farid Moore, and Razegheh Akhbarizadeh. Microplastic pollution in deposited urban dust, tehran metropolis, iran. *Environmental Science and Pollution Research*, 24(25):20360–20371, 2017.

[42] Zhou Qian, Tian ChongGuo, and Luo YongMing. Various forms and deposition fluxes of microplastics identified in the coastal urban atmosphere. *Chinese Science Bulletin*, 62 (33):3902–3909, 2017.

[43] Satoru Yukioka, Shuhei Tanaka, Yoshiki Nabetani, Yuji Suzuki, Taishi Ushijima, Shigeo Fujii, Hideshige Takada, Quang Van Tran, and Sangeeta Singh. Occurrence and characteristics of microplastics in surface road dust in kusatsu (japan), da nang (vietnam), and kathmandu (nepal). *Environmental Pollution*, 256:113447, 2020.

[44] Brett Roblin, Margaret Ryan, Andrew Vreugdenhil, and Julian Aherne. Ambient atmospheric deposition of anthropogenic microfibers and microplastics on the western periphery of europe (ireland). *Environmental science & technology*, 54(18):11100–11108, 2020.

[45] Karolina Szewc, Bożena Graca, and Anna Dołęga. Atmospheric deposition of microplastics in the coastal zone: Characteristics and relationship with meteorological factors. *Science of the Total Environment*, 761:143272, 2021.

[46] Emilie Strady, Thuy-Chung Kieu-Le, Quoc-Viet Tran, Quoc-Thinh Thuong, et al. Microplastic in atmospheric fallouts of a developing southeast asian megacity under tropical climate. *Chemosphere*, 272:129874, 2021.

[47] Yumei Huang, Tao He, Muting Yan, Lian Yang, Han Gong, Wenjing Wang, Xian Qing, and Jun Wang. Atmospheric transport and deposition of microplastics in a subtropical urban environment. *Journal of Hazardous Materials*, 416:126168, 2021.

[48] Ella Knobloch, Helena Ruffell, Alex Aves, Olga Pantos, Sally Gaw, and Laura E Revell. Comparison of deposition sampling methods to collect airborne microplastics in christchurch, new zealand. *Water, Air, & Soil Pollution*, 232(4):1–10, 2021.

[49] Neda Sharifi Soltani, Mark Patrick Taylor, and Scott Paton Wilson. Quantification and exposure assessment of microplastics in australian indoor house dust. *Environmental Pollution*, 283:117064, 2021.

[50] Marco Parolini, Diego Antonioli, Franco Borgogno, Maria Cristina Gibellino, Jacopo Fresta, Carlo Albonico, Beatrice De Felice, Susanna Canuto, Donatella Concedi, Alessandra Romani, et al. Microplastic contamination in snow from western italian alps. *International Journal of Environmental Research and Public Health*, 18(2):768, 2021.

[51] Subhasish Dey, Sk Zeeshan Ali, and Ellora Padhi. Terminal fall velocity: the legacy of stokes from the perspective of fluvial hydraulics. *Proceedings of the Royal Society A*, 475 (2228):20190277, 2019.

[52] H Seinfeld John, N Spyros, et al. Atmospheric chemistry and physics: from air pollution to climate change, 1997.

[53] Walter RA Goossens. Review of the empirical correlations for the drag coefficient of rigid spheres. *Powder Technology*, 352:350–359, 2019.

[54] Walter RA Goossens. A new explicit equation for the terminal velocity of a settling sphere. *Powder Technology*, 362:54–56, 2020.

[55] E Loth. Drag of non-spherical solid particles of regular and irregular shape. *Powder Technology*, 182(3):342–353, 2008.

[56] Gholamhossein Bagheri and Costanza Bonadonna. On the drag of freely falling non-spherical particles. *Powder Technology*, 301:526–544, 2016.

[57] Sabine Tran-Cong, Michael Gay, and Efstathios E Michaelides. Drag coefficients of irregularly shaped particles. *Powder Technology*, 139(1):21–32, 2004.

[58] EK Marchildon, A Clamen, and WH Gauvin. Drag and oscillatory motion of freely falling cylindrical particles. *The Canadian Journal of Chemical Engineering*, 42(4): 178–182, 1964.

[59] Prabhata K Swamee and Chandra Shakhar P Ojha. Drag coefficient and fall velocity of nonspherical particles. *Journal of Hydraulic Engineering*, 117(5):660–667, 1991.

[60] Bing Ren, Wenqi Zhong, Baosheng Jin, Yong Lu, Xi Chen, and Rui Xiao. Study on the drag of a cylinder-shaped particle in steady upward gas flow. *Industrial & engineering chemistry research*, 50(12):7593–7600, 2011.

[61] Arthur Thomas Corey et al. *Influence of shape on the fall velocity of sand grains*. PhD thesis, Colorado A & M College, 1949.

[62] Carl Wilhelm Oseen. Uber die stokes' sche formel und uber eine verwandte aufgabe in der hydrodynamik. *Arkiv Mat., Astron. och Fysik*, 6:1, 1910.

[63] David J Tritton. Experiments on the flow past a circular cylinder at low reynolds numbers. *Journal of Fluid Mechanics*, 6(4):547–567, 1959.

[64] Burke Huner and RG Hussey. Cylinder drag at low reynolds number. *The Physics of Fluids*, 20(8):1211–1218, 1977.

[65] Arzhang Khalili and Bo Liu. Stokes' paradox: creeping flow past a two-dimensional cylinder in an infinite domain. *Journal of Fluid Mechanics*, 817:374–387, 2017.

[66] RK Finn. Determination of the drag on a cylinder at low reynolds numbers. *Journal of Applied Physics*, 24(6):771–773, 1953.

[67] Kolf Jayaweera and BJ Mason. The behaviour of freely falling cylinders and cones in a viscous fluid. *Journal of Fluid Mechanics*, 22(4):709–720, 1965.

[68] Felipe Gómez-Noguez, Luis Manuel León-Rossano, Klaus Mehltreter, Alma Orozco-Segovia, Irma Rosas-Pérez, and Blanca Pérez-García. Experimental measurements of terminal velocity of fern spores. *American Fern Journal*, 107(2):59–71, 2017.

[69] FJ Carranza Chavez and Y Zhang. Single particle motion studies using stereo-vision and digital image processing. 2016.

[70] Luis Blay Esteban, John Shrimpton, and Bharathram Ganapathisubramani. Edge effects on the fluttering characteristics of freely falling planar particles. *Physical Review Fluids*, 3(6):1–14, 2018. ISSN 2469990X. doi: 10.1103/PhysRevFluids.3.064302.

[71] Timothy J Garrett, Sandra E Yuter, Cale Fallgatter, Konstantin Shkurko, Spencer R Rhodes, and Jason L Endries. Orientations and aspect ratios of falling snow. *Geophysical Research Letters*, 42(11):4617–4622, 2015.

[72] Brendan C Cole, Guy G Marcus, Shima Parsa, Stefan Kramel, Rui Ni, and Greg A Voth. Methods for measuring the orientation and rotation rate of 3d-printed particles in turbulence. *JoVE (Journal of Visualized Experiments)*, (112):e53599, 2016.

[73] Stefan Kramel, Greg A Voth, Saskia Tympel, and Federico Toschi. Preferential rotation of chiral dipoles in isotropic turbulence. *Physical review letters*, 117(15):154501, 2016.

[74] Guo Q Qi, Graham J Nathan, and Richard M Kelso. Ptv measurement of drag coefficient of fibrous particles with large aspect ratio. *Powder technology*, 229:261–269, 2012.

[75] Guo Q Qi, Graham J Nathan, and Richard M Kelso. Aerodynamics of long fibres settling in air at 10$<$ re$<$ 100. *Powder technology*, 235:550–555, 2013.

[76] Guoqiang Qi, Graham J Nathan, and Richard M Kelso. The influence of aspect ratio on distributions of settling velocities and orientations of long fibres. *Powder technology*, 257:192–197, 2014.

[77] Xiaoni Yang, Yi Wang, Honggang Yang, and Yang Yang. Experimental research on free settling properties of different types of single fiber particle in air. *Building and Environment*, 185:107300, 2020.

[78] Thu Ha Nguyen, Thuy-Chung Kieu-Le, Fiona HM Tang, and Federico Maggi. Controlling factors of microplastic fibre settling through a water column. *Science of The Total Environment*, page 156011, 2022.

[79] Xiaoni Yang, Yi Wang, Yunbo Li, Yingxue Cao, Yu Zhou, and Yanqiu Huang. Experimental research on the settling property of slender fiber particles under the influence of multiple factors. *Powder Technology*, 405:117543, 2022.

[80] John R. Taylor. *An Introduction to Error Analysis: The Study of Uncertainties in Physical Measurements*. University Science Books, 2 sub edition, 1996. ISBN 093570275X.

[81] Keith E Paskins, Adrian Bowyer, William M Megill, and John S Scheibe. Take-off and landing forces and the evolution of controlled gliding in northern flying squirrels glaucomys sabrinus. *Journal of Experimental Biology*, 210(8):1413–1423, 2007.

[82] S M Soloff, R J Adrian, and Z-C Liu. Distortion compensation for generalized stereoscopic particle image velocimetry. *Measurement Science and Technology*, 8(12):1441–1454, dec 1997. doi: 10.1088/0957-0233/8/12/008. URL `https://doi.org/10.1088/0957-0233/8/12/008`.

[83] Ajay K Prasad. Stereoscopic particle image velocimetry. *Experiments in fluids*, 29(2): 103–116, 2000.

[84] B Wieneke. Volume self-calibration for 3d particle image velocimetry. *Experiments in fluids*, 45(4):549–556, 2008.

[85] Bernhard Wieneke. Improvements for volume self-calibration. *Measurement Science and Technology*, 29(8):084002, 2018.

[86] F Cabrera, MZ Sheikh, B Mehlig, Nicolas Plihon, M Bourgoin, Alain Pumir, and Aurore Naso. Experimental validation of fluid inertia models for a cylinder settling in a quiescent flow. *Physical Review Fluids*, 7(2):024301, 2022.

[87] Nian-Sheng Cheng. Formula for the viscosity of a glycerol- water mixture. *Industrial & engineering chemistry research*, 47(9):3285–3288, 2008.